EXPERIMENTAL INVESTIGATION OF FLOW BOILING CHARACTERISTICS OF AN IMMERSION COOLED SERVER MODEL

by

Sriram Chandrasekaran

A thesis submitted to the Graduate Faculty of
Auburn University
in partial fulfillment of the
requirements for the Degree of
Master of Science

Auburn, Alabama
August 5, 2017

Keywords: Immersion cooling, Flow boiling, Microporous, Microfinned, Impingement flow system, Nucleation suppression

Approved by

Sushil H. Bhavnani, Chair, Professor of Mechanical Engineering
Roy W. Knight, Assistant Professor of Mechanical Engineering
Jay M. Khodadadi, Professor of Mechanical Engineering

Abstract

The meteoric growth of global communication and networking infrastructure has resulted in demand for high-performance data centers. With the increase in power capacity of server electronics, thermal management of data centers has become a significant challenge, as the traditional air cooling technique is approaching its heat dissipation limit. Liquid immersion cooling is a liquid cooling technique that offers orders of magnitude higher heat transfer rates than air cooling, and also has the potential to reduce the energy needed for cooling data centers. While the liquid immersion solutions that are currently used in commercial applications provide some of these benefits, most of these solutions employ a large fluid inventory of expensive dielectric fluid to cool the server packages. A modular cooling solution that isolates each server blade will result in a smaller fluid inventory, which in turn would reduce the fluid costs and also improve the ease of maintenance.

This study explores the thermal performance of a line replaceable, small form factor server cooling module with fluid inventory less than 2L. Flow boiling tests were performed on test boards with four high-performance dies in a square array. Three different test boards – boards with bare silicon, and silicon surfaces enhanced with microporous and microfinned heat sinks were tested. Novec 649 was used as the primary coolant in this study. Heat flux improvement of up to 50% was achieved by increasing the flow rate and decreasing the facility water temperature of the system. The use of enhanced surfaces provided significantly lower operating temperatures than the bare silicon surface.

In addition to the flow distribution system that delivers a parallel flow over to the heated surfaces, a flow distribution system that delivers impinging flow to the bottom row of heaters was also tested. For the microfinned surface, the highest heat flux recorded was 28.6 W/cm^2 which is roughly 185 W per die. The nucleation suppression phenomena in flow boiling was also investigated for this server model, and it was observed that the microfinned surface with impinging flow distribution system suppressed boiling activity for heat flux values of up to 18 W/cm^2. High-speed imaging was performed to assess the boiling activity, and to understand the change in nucleation characteristics brought about by the change in parameters of this system.

Acknowledgments

To Dr. Sushil H. Bhavnani, Dr. Roy W. Knight and Dr. Jay M. Khodadadi, thank you for your guidance and support throughout my graduate coursework and research. To all my friends at Auburn, especially Christopher Duron, Le Gao, Michael Henry and Kayla Reid, thanks for helping me through this journey. To Dr. Sushil H. Bhavnani, thank you for the support and motivation you have provided me all through this research. To my parents, sister and other family members, thank you for your confidence in me through every step of this journey.

Table of Contents

Abstract ii

Acknowledgments iv

List of Figures vii

List of Tables xi

Nomenclature xiii

Chapter 1: Introduction 1

- 1.1 Data Center Power Consumption 1
- 1.2 Heat Dissipation Requirements 7

Chapter 2: Literature Review 10

- 2.1 Liquid Cooling in Data Centers 10
- 2.2 Fundamentals of Boiling Heat Transfer 17
- 2.3 Tailored Surfaces for Improving Boiling Heat Transfer 20
- 2.4 Boiling Performance Enhancement Studies in Electronics Cooling 24
    - 2.4.1 Pool Boiling 24
    - 2.4.2 Flow Boiling 27
- 2.5 Impingement Boiling 28
- 2.6 Nucleation Suppression in Flow Boiling 33
- 2.7 Flow Visualization Techniques 34
- 2.8 Objectives of this Study 38

Chapter 3: Experimental Setup 40
    3.1 Enclosure Assembly 40
    3.2 Fluid Supply and Control System 47
    3.3 Surface Enhancements 50
    3.4 High-Speed Imaging System 51
Chapter 4: Results and Discussion 53
    4.1 Parallel Flow Distribution System Results 54
        4.1.1 Facility Water Temperature and Dielectric Flow Rate Effects 55
        4.1.2 Surface Enhancement Effects 69
    4.2 Impinging Flow Distribution System Results 75
        4.1.1 Dielectric Flow Rate and Facility Water Temperature Effects 71
        4.1.2 Impact of Surface Enhancement 82
    4.3 Flow Distributor Effects 86
    4.4 Nucleation Suppression 93
Chapter 5: Conclusions 102
    5.1 Suggestions for Future Study 103
References 105
Appendix A: Flow Distributor Component Drawings 118
Appendix B: Data Acquisition System 121
Appendix C: Sample Calculations 125
Appendix D: Microporous Surface Enhancement Fabrication Procedure 127

List of Figures

Figure 1 – Historical data center power consumption in the United States [1] 2

Figure 2 – Self-reported average PUE values from 2011-2014 [2] 3

Figure 3 – Immersion cooling system from Green Revolution Cooling [10] 5

Figure 4 – Iceotope liquid cooling system [11] [12] 6

Figure 5 – Heat transfer coefficients for various fluids and heat transfer mechanisms. Adapted from [20] 9

Figure 6 – Heat flux demands of bipolar and CMOS transistors over time [21] 11

Figure 7 – Cooling system in IBM System/360 [23] 12

Figure 8 – Thermal conduction module from IBM [22] [23] 13

Figure 9 – Schematic of IBM z Enterprise EC 12 processor cooling system [25] 14

Figure 10 – Schematic of ChilledDoor® rear door heat exchangers from Motivair™ [28] ... 15

Figure 11 – PCB module of the Cray-2 supercomputer [30] 16

Figure 12 – Liquid cooling system in Cray-2 supercomputer [29] 16

Figure 13 – Pool boiling curve [32] 19

Figure 14 – (Left to right) free, submerged and confined jet configurations [57] 29

Figure 15 – Different regions in a submerged jet configuration [57] 30

Figure 16 – Fin profiles used in the study by Ndao et al. [62] 32

Figure 17 – Nucleation suppression in flow boiling [67] 35

Figure 18 – Single-phase PIV images with (left) and without (right) flow guides [47] 37

Figure 19 – Flow map generated from two-phase PIV showing coolant entry points [47] 37

Figure 20 – Enclosure assembly 41

Figure 21 – Coolant channel (left) and pin-fin condenser (right) on top of the enclosure 41

Figure 22 – Circuit diagram of the thermal test cell 43

Figure 23 – Test cell arrangement and PCB layout 44

Figure 24 – Flow in parallel flow distributor (left) and impinging flow distributor (right) 47

Figure 25 – Fluid supply and control system 49

Figure 26 – Microporous (top) and microfinned (bottom) enhancement surfaces 52

Figure 27 – Effect of subcooling and flow rate on flow boiling curves [71] 56

Figure 28 – Effect of increasing flow rates on thermal performance of bare silicon surface with parallel flow distributor 57

Figure 29 – Boiling activity at heat-addition termination point for the bare silicon surface 58

Figure 30 – Effect of decreasing facility water temperatures on the boiling curves of bare silicon surface with parallel flow distributor 59

Figure 31 – Nucleation characteristics of bare silicon surfaces at the lowest flow rate and highest facility water temperature (a) and vice-versa (b) 62

Figure 32 – Effect of increasing flow rate on flow boiling curves of the microporous surface with parallel flow distributor 63

Figure 33 – Effect of decreasing facility water temperature on the flow boiling performance of microporous surfaces with parallel flow distributor 64

Figure 34 –Screen –captured high-speed images shows the vigorous boiling activity at the heat-addition termination point for the microporous surface 65

Figure 35 – Effect of increasing flow rate on thermal performance of the microfinned surface with parallel flow distribution system.. 66

Figure 36 – Effect of decrease in facility water temperature on the thermal performance of the microfinned surface with parallel flow distributor 68

Figure 37 – Comparison of thermal performance of three surfaces at a fixed facility water temperature and flow rate 73

Figure 38 – Screen-captured high-speed images of microfinned surface showing the movement of vapor slug through the inter-fin spacing.. 74

Figure 39 – Effect of increasing the flow rate on thermal performance of bare silicon surfaces with impinging flow distributor 76

Figure 40 – Effect of decreasing the facility water temperature on the thermal performance of bare silicon surface with impinging flow distributor.. 77

Figure 41 – Effect of flow rate on thermal performance of microfinned surface with impinging flow distributor.. 79

Figure 42 – Effect of decrease in facility water temperature on thermal performance of microfinned surface with impinging flow distributor... 81

Figure 43 – Thermal performance comparison for bare silicon and microfinned surfaces for impingement flow distribution system.. 83

Figure 44 – Screen-captured high-speed image showing vigorous boiling activity only at the right corner of the microfinned surface 85

Figure 45 – Comparison of thermal performance of parallel and impinging flow distributors for the bare silicon surface for 360 mL/min flow rate 87

Figure 46 – Comparison of thermal performance of parallel and impinging flow distributors for the bare silicon surface for 1260 mL/min flow rate 89

Figure 47 – Comparison of thermal performance of parallel and impinging flow distributors for the microfinned surface for 1260 mL/min flow rate 90

Figure 48 – Comparison of thermal performance of parallel and impinging flow distributors only for the bottom microfinned surfaces at 1260 mL/min flow rate 92

Figure 49 – Nucleation suppression in bare silicon surfaces 94

Figure 50 – Temperature profiles for pool boiling system (left) and flow boiling system (right) . 97

Figure 51 – Nucleation suppression in microfinned surfaces 99

List of Tables

Table 1 – Diode Temperature Measurement Locations 44

Table 2 – Saturated fluid properties of Novec 649 54

Table 3 – Parameters used in parallel flow distribution system studies 54

Table 4 – Thermal performance summary of bare silicon surfaces with parallel flow distributor 61

Table 5 – Thermal performance summary of microporous surface with parallel flow distribution system 65

Table 6 – Thermal performance summary for the microfinned surface with parallel flow distribution system 69

Table 7 – Highest heat flux recorded in this study for different surfaces with parallel flow distribution system 71

Table 8 – Parameters used in impinging flow distribution system studies 75

Table 9 – Thermal performance summary of the bare silicon surface with impinging flow distribution system 78

Table 10 – Thermal performance summary of the microfinned surface with impingement flow distribution system 82

Table 11 – Highest recorded heat flux for bare silicon and microfinned surfaces with impinging flow distributor at 1260 mL/min flow rate and 7°C facility water temperature 82

Table 12 – Highest thermal performance recorded for the bare silicon and microfinned surfaces with impinging flow distributor with power only to bottom heated surfaces 85

Table 13 – Highest heat flux comparison of parallel and impinging flow distributors 86

Table 14 – Summary of heat flux values with nucleation suppression for bare silicon surface 98

Table 15 – Summary of heat flux values with nucleation suppression for microfinned surface 101

Nomenclature

h	heat transfer coefficient, ($W/m^2 \cdot K$)
A	heat transfer area (m^2)
T_s	temperature of the surface (°C)
T_∞	temperature of the fluid (°C)
q''	surface heat flux (W/m^2) or (W/cm^2)
ΔT	temperature difference (°C)
μ	dynamic viscosity (kg.m/sec)
ρ	density (kg/m^3)
Pr	Prandtl number
T_w	wall temperature (°C)
T_{sat}	saturation temperature of the liquid (°C)
C_p	specific heat ($kJ/kg \cdot K$)
h_{lv}	latent heat of vaporization (kJ/kg)
g	acceleration due to gravity (m/s^2)
C_{sf}	Rohsenow correlation surface constant factor
σ	surface tension (N/m)
P	pressure (kPa)

δ	momentum boundary layer thickness (m)
δ_t	thermal boundary layer thickness (m)
Re	Reynolds number

Subscripts

l	liquid phase property
v	vapor phase property
e	effective

Chapter 1: Introduction

With the rapid progress of today's society into the prime of the information age, the need for increase in networking and communication infrastructure is more than ever before. The developments in data transfer capability have a resulted in a highly interconnected world, in which online social networking has become an important part of life, where many businesses now cannot function without e-commerce, and media storage in computers and personal devices is being phased out by online audio/video streaming services. These demands have led to a dramatic increase in number and size of data center facilities. The other significant achievement in the development of electronic devices is the increase in computational power of the microprocessor, while simultaneously decreasing the footprint. Over recent years, computers, cell phones and other electronic devices have registered orders of magnitude improvement in performance and capability, while managing to become slim and compact. These developments in data center infrastructure and microprocessor power density pose new challenges, which require timely solutions necessary to sustain future development.

1.1 Data Center Power Consumption

In 2014, the total power consumed by the data center facilities across the United States was roughly 70 billion kWh, which is around 1.8% of the country's annual electricity production [1]. From Figure 1, it can be observed that the growth in data center power consumption over recent years has been relatively flat. One of the reasons responsible for this flat trend is the economic recession that has resulted in the decline in annual server shipment growth to 5% during 2005-2010, and further down to 3% after 2010.

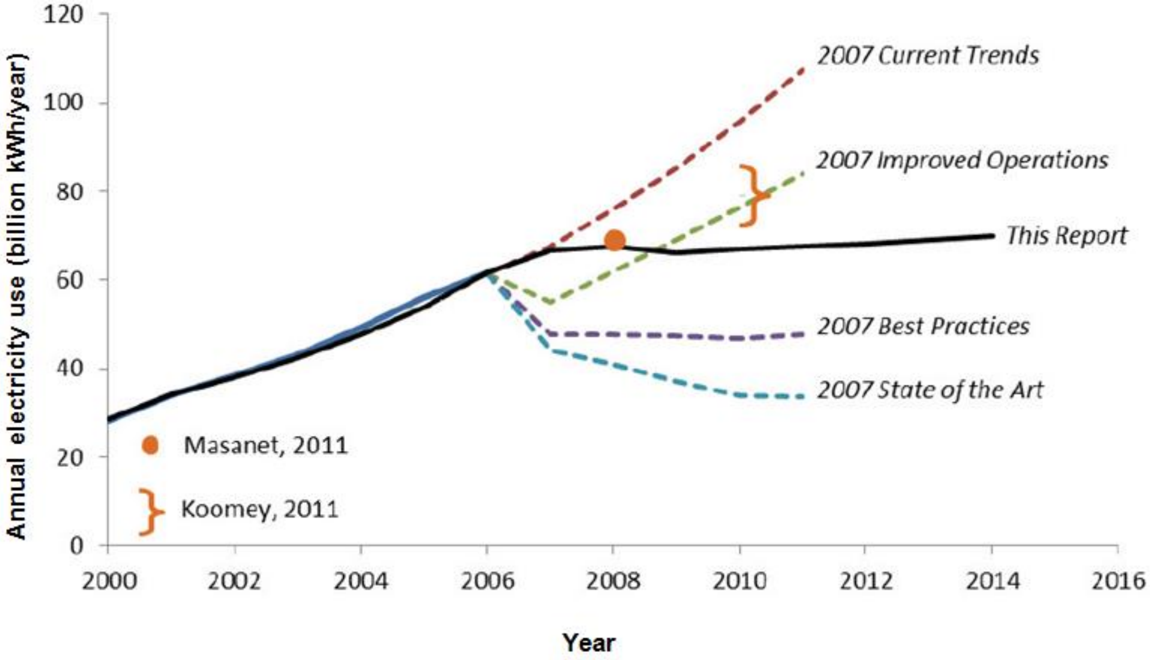

Figure 1: Historical data center power consumption in the United States [1]

Another reason for this trend that is associated with actual improvement in energy utilization is the increase in the number of hyperscale data center facilities. To provide same services, these data centers require fewer severs than traditional data centers, as the servers in hyperscale facilities are configured for higher utilization rates. While other factors such as efficiency improvements in network, storage and infrastructure are cited as reasons for decrease in growth, the infrastructure improvements such as increase in data center cooling efficiency are observed only in large cloud data centers. A common metric that is used to quantify the energy utilization in data centers power usage effectiveness (PUE), which is the ratio of the total energy delivered to the data center to the energy delivered to the computing or IT equipment. A PUE value of one is ideal, in which all the energy supplied to the data center is utilized for processing. According to the surveys by the Uptime Institute®, in which the institute's network members self-reported the PUE values, the average PUE values have not significantly changed over the recent years [2]. Figure 2 shows these reported PUE values for 2011-2014.

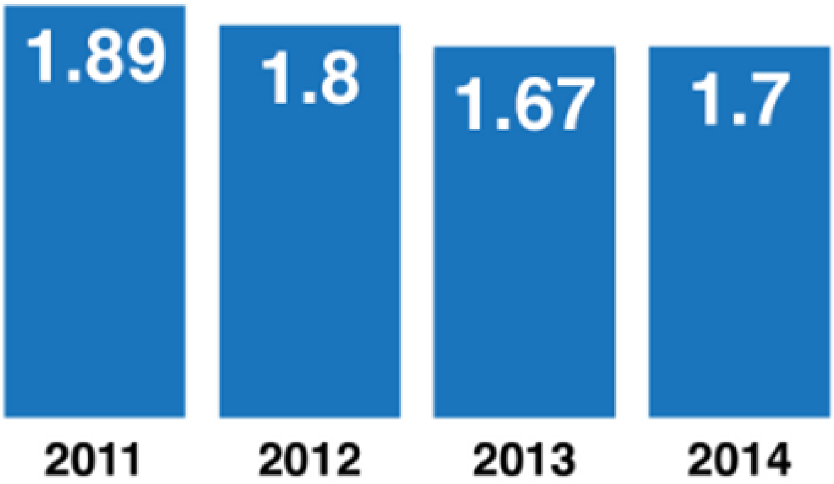

Figure 2: Self-reported average PUE values from 2011-2014 [2]

The trend supports the assertion that the sluggish growth in data center power consumption is not primarily due to improved energy-efficiency. With energy costs on the rise and natural resources diminishing, measures to reduce the already substantial power consumption must be taken. One avenue for improvement is reducing the energy spent on data center cooling, which represents around 33% of the energy utilized by data centers [3].

Improvements in energy efficiency of the air cooling techniques are being carried out across various levels, from reducing contact resistance at the chip level to optimizing air flow at the room and plenum levels. Strategies such as hot/cold aisle separation and server rack exhaust chimneys have been implemented to prevent mixing of hot and cold air streams, with reported energy savings of up to 59% over traditional open type data centers [4]. The environmental responsibility and economic incentive associated with cooling energy savings have motivated data center giants such as Google™ and Facebook™ to adopt a number of measures to reduce cooling power. These measures include the use free cooling energy by employing sea water for heat rejection and planning facilities at locations with cold climates, and other techniques such as use of evaporative cooling to bring chilled water into the room and air-side economizers to bring external air into the room. These steps have resulted in Google maintaining an average Twelve Month Trailing (TTM) PUE value of 1.12 for all its large-scale data centers [5], and TTM PUE value of 1.09 at Facebook's Prineville datacenter facility [6].

Parallel to the studies that focus on air cooling efficiency improvement, studies have been conducted to quantify the energy-efficiency of liquid cooling techniques for cooling server packages. Liquid immersion cooling has been used by a number of commercial entities and has been proven to substantially reduce cooling power. 3M™ claims that the use of two-phase liquid immersion cooling techniques can reduce cooling energy by more than 95%, while resulting in a smaller facility footprint, as the immersion cooled facilities require ten times less floor space than the air cooled facilities [7]. These claims are supported by the DataTank™ cooling modules offered by Allied Control, which use the 3M Novec™ family of dielectric fluids to achieve PUE values of 1.01 or less [8]. The cooling modules use the open bath immersion (OBI) cooling technique, in which the server packages are immersed in large tanks containing the dielectric fluid. Green Revolution Cooling (GRC) uses a single-phase OBI approach for its CarnotJet™ system, where a dielectric mineral oil blend removes the heat from the server packages. The cooling system, when tested at Intel® New Mexico facility provided PUE of 1.02-1.03 [9]. Figure 3 shows a CarnotJet system.

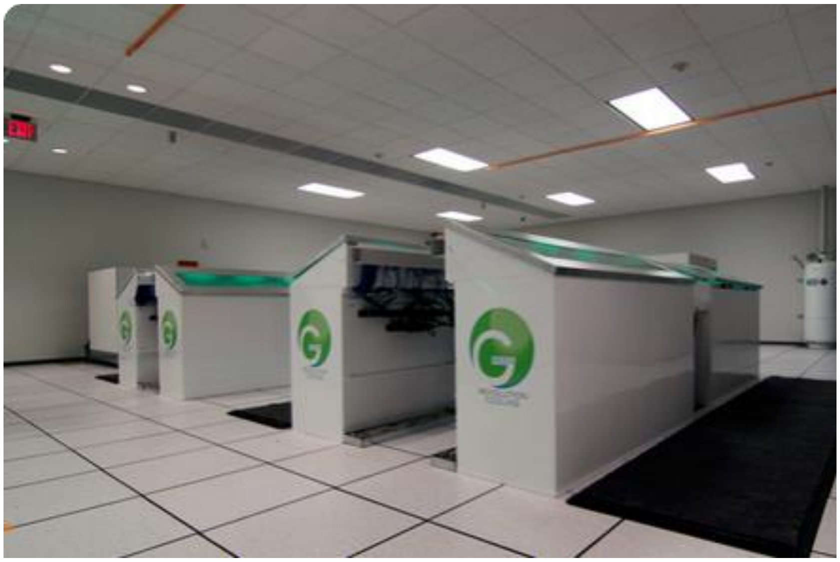

Figure 3: Immersion cooling system from Green Revolution Cooling [10]

In contrast to the OBI approaches, the liquid cooling solution from Iceotope™ uses a modular approach in each server blade is encapsulated in a sealed system with individual fluid and electrical connections. Single-phase natural convection drives the primary fluid movement inside the enclosure. The primary fluid, which is from the Novec family of fluids, then rejects the heat into water that is circulated through a jacket. Figure 4 shows the cooling system from Iceotope. Using this approach, more than 80% of cooling energy reduction was recorded during the tests at University of Leeds [11].

Figure 4: Iceotope liquid cooling system [11] [12]

The current study focuses on a small form factor cooling model which follows the same modularity principle as the Iceotope cooling system, but with the capability to operate using convective two-phase heat transfer. This type of design offers reduced fluid inventory over the OBI approach, as the large tanks are replaced by small form factor server blades placed in racks. Another advantage of this design is the line replaceability and ease of access, as all the fluid and electrical connections are simple to connect/disconnect.

1.2 Heat Dissipation Requirements

The advancements in manufacturing technologies used to fabricate microelectronics have resulted in progressive decrease in transistor spacing on an Integrated Circuit (IC), leading to smaller interconnect lengths and higher processing speeds. Dr. Gordon E. Moore's prediction that the number of transistors on a chip would double every 2 years [13] has been proven to be accurate until recent years. The decrease in transistor density due to the current limitations in micro fabrication processes has led a slight deviation from Moore's law [14]. The feature length that defines the transistor spacing is now at 14 nm [15], and Samsung™ has already released Qualcomm® Snapdragon™ 835 processor, which has a feature length of 10 nm [16]. The increasing transistor density results in a higher power density, which means more heat is now generated that must be dissipated to maintain the junction at operating temperature. This leads to an increase in heat flux value, as increasing the footprint of the processor to accommodate the increase in heat dissipation is counter to the consumer expectations of compact electronics. Relaxing the heat dissipation requirements would result in an increase in the junction temperature, which in turn would result in increased failure rates and decrease the reliability of electronic systems [17]. The International Technology Roadmap for Semiconductors (ITRS) specifies that the heat flux requirement for the 14 nm generation is greater than 100 W/cm^2 [18], and heat flux requirements are expected to reach up to 1000 W/cm^2 in the next decade [19]. These high heat flux values will render the traditional air-cooling solutions impractical for thermal management.

$$q = h * A * (T_s - T_\infty) \tag{1}$$

$$q" = h * \Delta T \tag{2}$$

An analysis of Newton’s law of cooling indicates the potential avenues to increase heat dissipation. Equation 1 shows that the heat dissipated from a surface depends on the heat transfer coefficient, area of the surface, the surface temperature and the ambient temperature. At this point, it is clear that the surface area and the surface temperature cannot be modified. While reducing ambient temperature would result in increased heat dissipation, there are limitations to the lowest air temperature that can be achieved. Also, decreasing ambient air temperature is not economical as it increases air-conditioning costs. With these restrictions in heat flux and temperature values, the only possible way to achieve high heat flux values is to increase the heat transfer coefficient, which is clearly depicted in Equation 2.

Figure 5 shows the heat transfer coefficients of various fluids under different heat transfer mechanisms. From the figure it can be observed that for a given heat transfer mechanism -- say natural convection, the liquid cooling techniques offer higher heat transfer coefficients than air cooling techniques. While the use of liquid cooling methods such as forced convection of water through cold plates mitigates some of the heat flux requirements, the heat transfer path from the junction to the fluid has multiple resistances such as contact and spreading resistances which

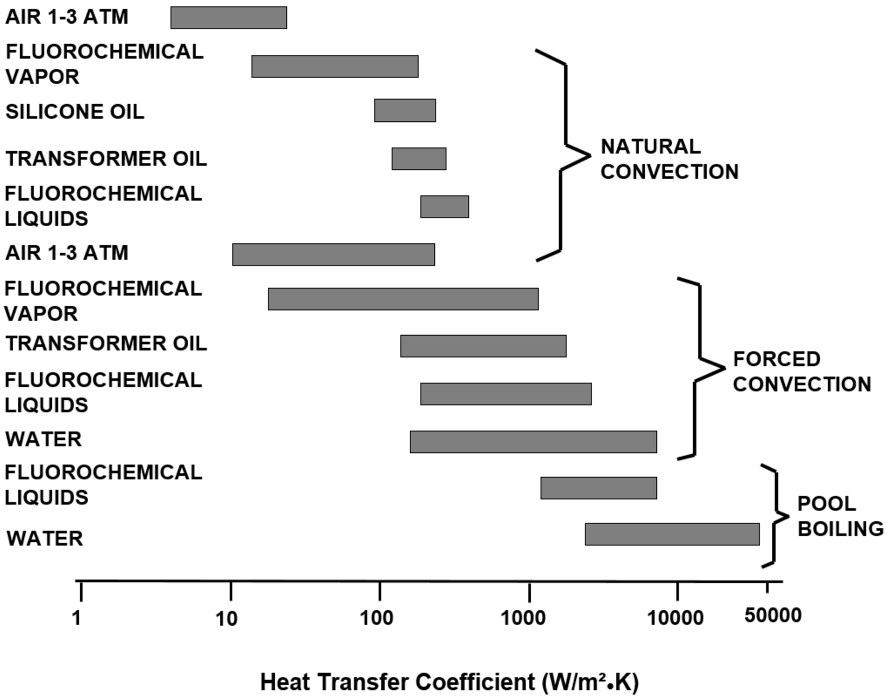

Figure 5: Heat transfer coefficients for various fluids and heat transfer mechanisms. Adapted from [20]

decrease the overall heat transfer coefficient of the system. On the other hand, liquid immersion cooling techniques have highly simplified heat transfer paths with fewer resistances, which result in high heat transfer coefficients. The two-phase liquid immersion systems offer orders of magnitude higher heat transfer rates than their single-phase counter parts, and prove to hold high potential in satisfying the growing heat flux demands. The current study investigates the highest achievable heat flux values in a small form factor server model that uses two-phase liquid immersion cooling, while maintaining die temperatures well below the current industry requirements.

Chapter 2: Literature Review

This chapter aims to provide an overview of key research activities in the field of electronics cooling, to understand the motivation behind the current study and the factors that influenced its development. An outline of liquid cooling techniques in data centers is presented first, followed by an introduction to two-phase heat transfer. The rest of this chapter focuses on studies that pertain to tailored surfaces to improve boiling performance, different boiling processes employed in cooling electronics, nucleation suppression phenomenon in flow boiling and flow visualization techniques.

2.1 Liquid Cooling in Data Centers

While liquid cooling solutions for data centers are developing at a rapid pace now more than ever, liquid cooling for electronics in general, is not a new technology. Prior to the introduction of complementary metal oxide semiconductor (CMOS) transistors as switching elements in ICs, bipolar transistors were used. Being less efficient than CMOS, the bipolar transistors generated significantly higher heat flux values to provide similar performance. The heat flux increase for bipolar and CMOS transistors, along with the computer system models that featured them, are shown in Figure 6. From this figure, it can be observed that the transition from bipolar to CMOS in the ‘90s resulted in significant reduction in heat flux values. To dissipate high heat flux values in electronic systems with bipolar transistor switching, computers in past have adapted liquid cooling solutions.

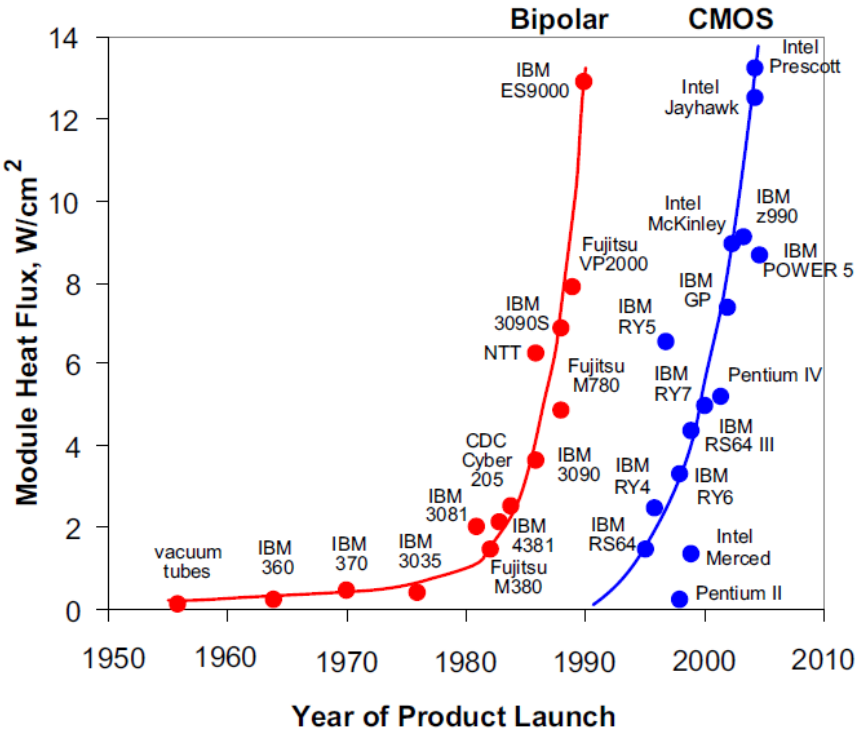

Figure 6: Heat flux demands of bipolar and CMOS transistors over time [21]

One of the earliest applications of liquid cooling can be traced back to IBM®, with the water cooling system for the System/360 Model 91 Processor in 1964 [21]. This system used a hybrid air-to-water cooling technique, in which the heat exchangers placed between rows of circuit boards cooled the hot air that was leaving one board assembly before entering the next assembly. This improved the heat transfer from the boards, as much of the heat gained by the air from the boards was rejected to the chilled water in the heat exchanger before it entered the next board assembly. The schematic of this system is shown in Figure 7. Another significant application that incorporated liquid cooling in data centers is the thermal conduction module (TCM) from IBM, for the IBM 3081 computing system [22]. This design features several components and systems, with a central objective of decreasing the resistances in the heat transfer path. The convection resistance is significantly reduced by replacing air cooling with a cold plate system that uses water as cooling fluid. Heat transfer from the chip to the cold plate is achieved through spring loaded piston arrangement inside cylinder housing filled with helium gas. The TCM module and the piston spring arrangement are shown in Figure 8. The piston and spring arrangement ensures proper contact between the chip and cold plate by compensating for chip alignment mismatch and stresses induced by the mismatch in coefficient of thermal expansion (CTE). Highly conductive metals were used in making springs and pistons used in this module. The inert helium gas, which is a good thermal conductor, enhances the conduction heat transfer by filling the gaps between the chip and the piston head, and also the gaps between the

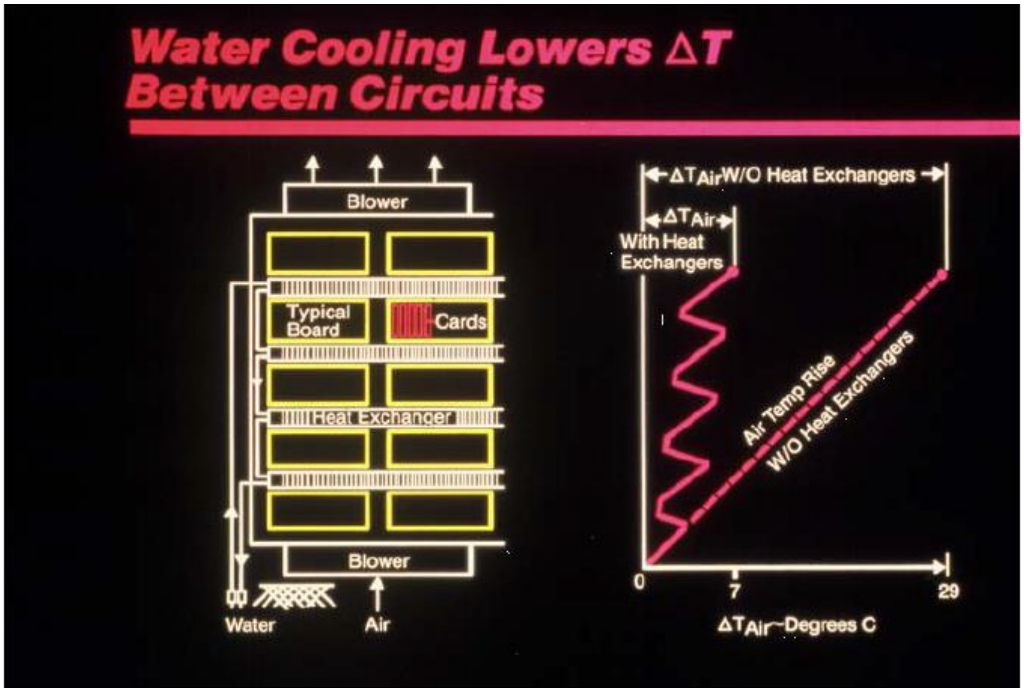

Figure 7: Cooling system in IBM System/360 [23]

spring and the cold plate. The TCM is approximately 150 mm x 150 mm x 60 mm in size, and can dissipate up to 300 W from an array of chip placed in 90 mm x 90 mm envelope [24].

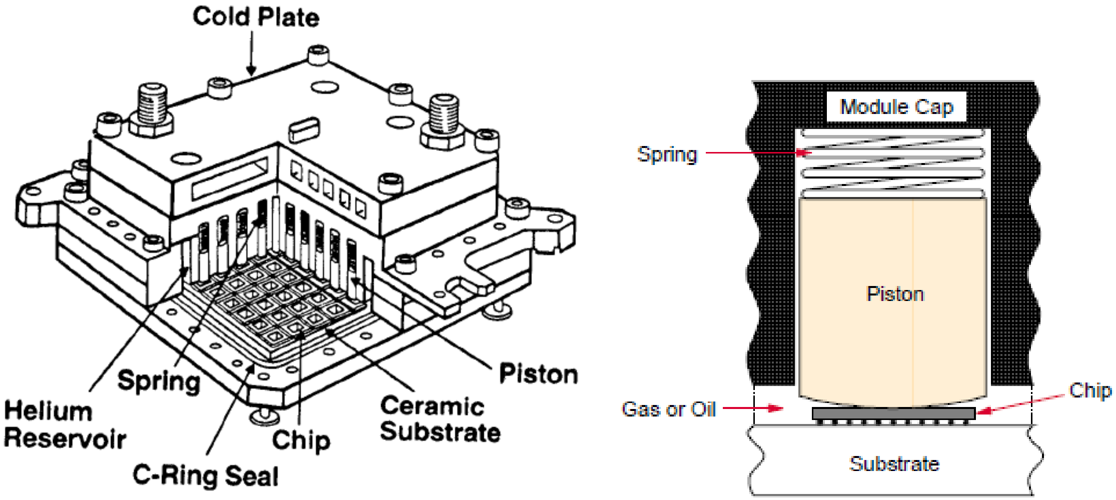

Figure 8: Thermal conduction module from IBM [22] [23]

Recent liquid cooling techniques include the IBM zEC 12 systems that have eliminated refrigeration systems and instead use a radiator system in which the water circulating in cold plates is cooled by air flow [25]. This system also features a backup heat sink attached to the electronic packages to allow for low clock speed operation, in the event of failure in the water cooling system. The schematic of this system is shown in Figure 9.

Efforts to bring the cooling systems closer to the server packages have resulted in the growth of hybrid air-water cooling systems. The operating principle of these systems is similar to that of the inter-board heat exchangers in the IBM System/360 computers. Heat exchangers are placed on the server racks, either at the side, top or rear location. The rear configuration has the heat exchanger placed on door and is called a rear door heat exchanger (RDHx). In this system, cold air enters the server rack from the front, and gets heated through the heat transfer from the electronic packages in the rack. This hot air then passes through a heat exchanger setup mounted on the rear side of the rack, and rejects the heat into the liquid passed through the heat exchanger coils. In some designs, up to 100% of the heat is rejected by the hot air into the cooling liquid [26]. This system can provide supplemental cooling for few high density racks or provide total cooling to the racks, eliminating the need for hot/cold aisle separation in traditional data centers. The heat exchanger in this system uses water or refrigerants as cooling fluid. A schematic of this system is shown in Figure 10. The other heat exchangers such as the side and top mounted systems work on a similar principle.

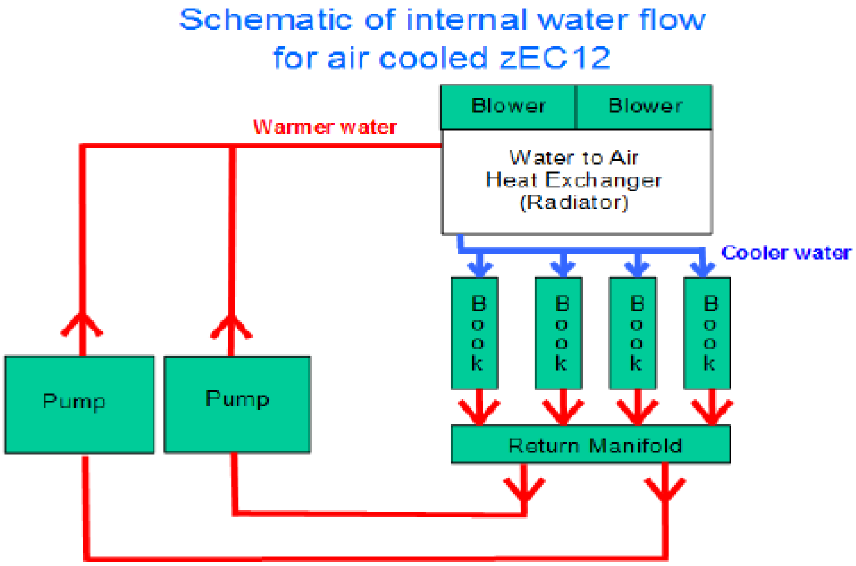

Figure 9: Schematic of IBM z Enterprise EC 12 processor cooling system [25]

A notable early application of liquid immersion cooling was the cooling system in Cray-2 supercomputer. Figure 11 shows eight printed circuit boards (PCB), stacked and packaged one above the other to form a three dimensional module. This multichip module has a heat flux value of about 0.2 W/cm² per chip [27], a value that could be addressed by air cooling techniques.

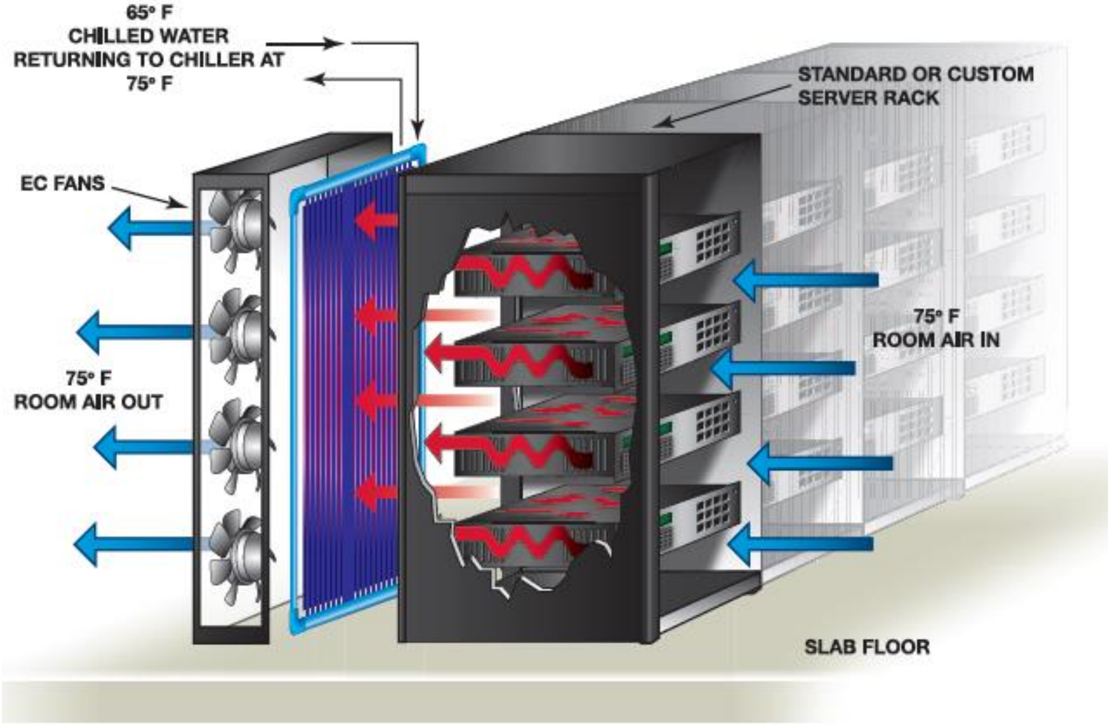

Figure 10: Schematic of ChilledDoor® rear door heat exchangers from Motivair™ [28]

However, the high density of chips on the PCB required a volumetric flow rate of air that was not practical. To address this problem, single-phase liquid immersion cooling with FC-77 fluid was used as the cooling solution. Figure 12 shows the schematic from the patent filed for this system. Horizontal flow of coolant over the radially arranged chip modules is achieved through stand pipes with provisions to ensure uniform flow over each board in the stacks. The flow rate is approximately 0.0254 m/s (1 in./s) across the boards [29]. The pumping systems transport this fluid into and out of the reservoirs for heat rejection. Each module in this system measures 0.1016 m x 0.2032 m x 0.0254 m (4 in x 8 in x 1 in) and could dissipate up to 700 W. The volumetric heat dissipation of this system exceeds far beyond the capabilities of today's air cooled servers.

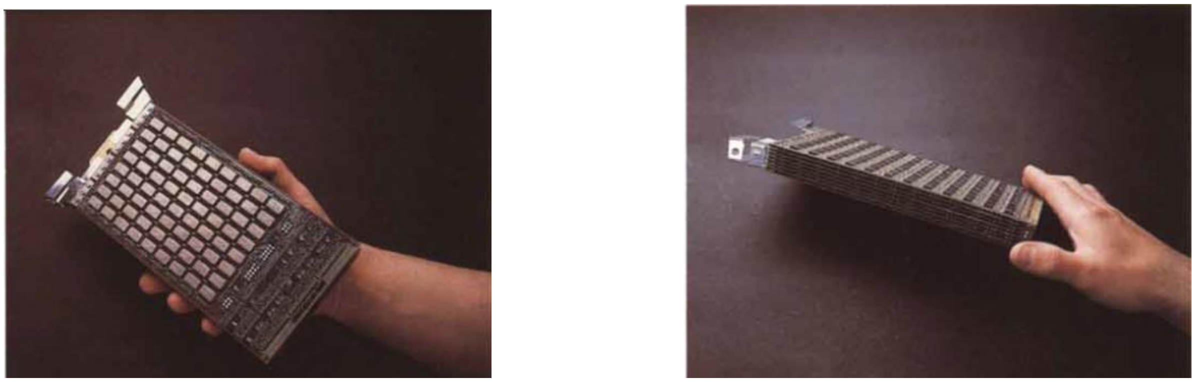

Figure 11: PCB module of the Cray-2 supercomputer [30]

FIG. 14

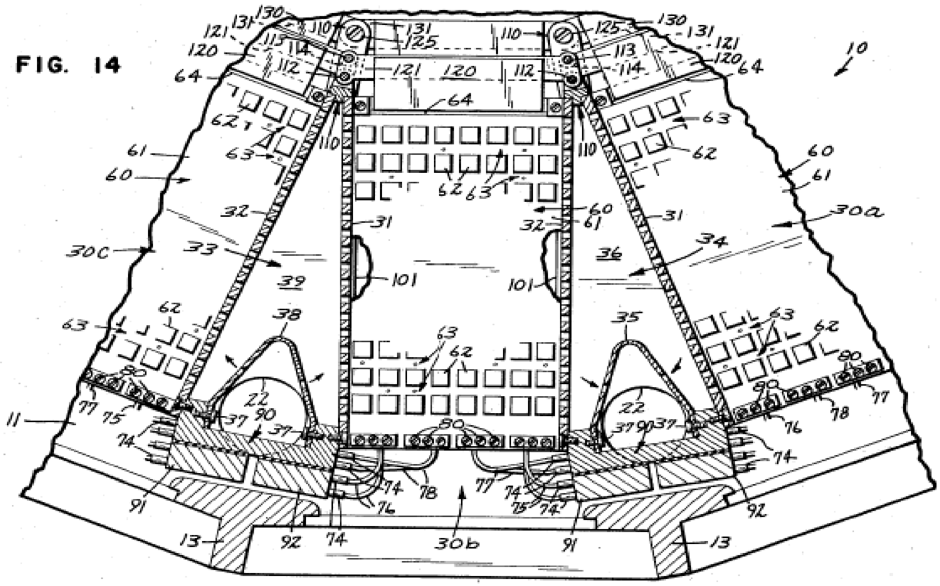

Figure 12: Liquid cooling system in Cray-2 supercomputer [29]

Figure 12 shows a top section view of the computing system. FC-77 dielectric fluid flows over the heated surfaces from left inlet standpipe to the right outlet standpipe. Both standpipes have holes along the length (into and out of the paper) to provide equal flow to the PCB modules.

With the CMOS transistors approaching the same heat flux trends as that of the bipolar transistors, single-phase and two-phase liquid immersion solutions have re-emerged, as witnessed by the growth in commercial OBI solutions such as CarnotJet™, DataTank™ and IceoTope™ systems. The cooling module of the current study uses a two-phase immersion cooling system, and offers volumetric heat dissipation several times higher than the air cooled server.

2.2 Fundamentals of Boiling Heat Transfer

The importance of boiling in numerous engineering applications has motivated extensive studies on investigating the thermal performance and associated heat transfer mechanisms. A fundamental study by Nukiyama [31] provides information on the various regimes or stages in pool boiling. The experiments in this study were performed by heating platinum, nickel, nichrome, iron and fuse wires of known resistances through a supply of constant current. This power supply creates a constant heat flux input for which the surface temperature is measured through a Wheatstone bridge arrangement. Figure 13 provides the pool boiling curve that was pieced together from the experiments. The first regime up to point A is the natural convection regime, in which the surface temperature is less than the saturation temperature of the liquid in the pool. The density difference between the hot fluid close to the surface and the cold fluid far away from the surface creates fluid motion in the pool. The curve is approximately linear in this regime and the slope of this curve provides the heat transfer coefficient. As the heat flux is increased, the nucleation activity is initiated, and this point is called onset of nucleate boiling (ONB). The heat flux required to initiate the boiling activity is called incipience heat flux. The transition in the heat transfer mechanism from single-phase natural convection to partial boiling is marked by decrease in surface temperature, since for the same heat flux value, boiling has more heat transfer rate than single-phase natural convection. This overshoot in temperature is observed only in increasing heat flux experiments, since the energy required to initiate nucleation is more than energy required to deactivate the nucleation activity. Between points A and B is the partial boiling regime in which heat transfer is due to both natural convection and boiling. The slope of the curve is now steeper, which means that compared to the convection regime a relatively large change in heat flux is required to increase the difference in surface temperature by an equivalent value. This increase in heat transfer rate is mainly due to the numerous nucleating bubbles removing the heat from the boiling surface and transferring it to the pool liquid. Between the points B and C is the fully developed boiling regime in which the boiling effects are highly dominant over the convective effects and the entire surface is nucleating.

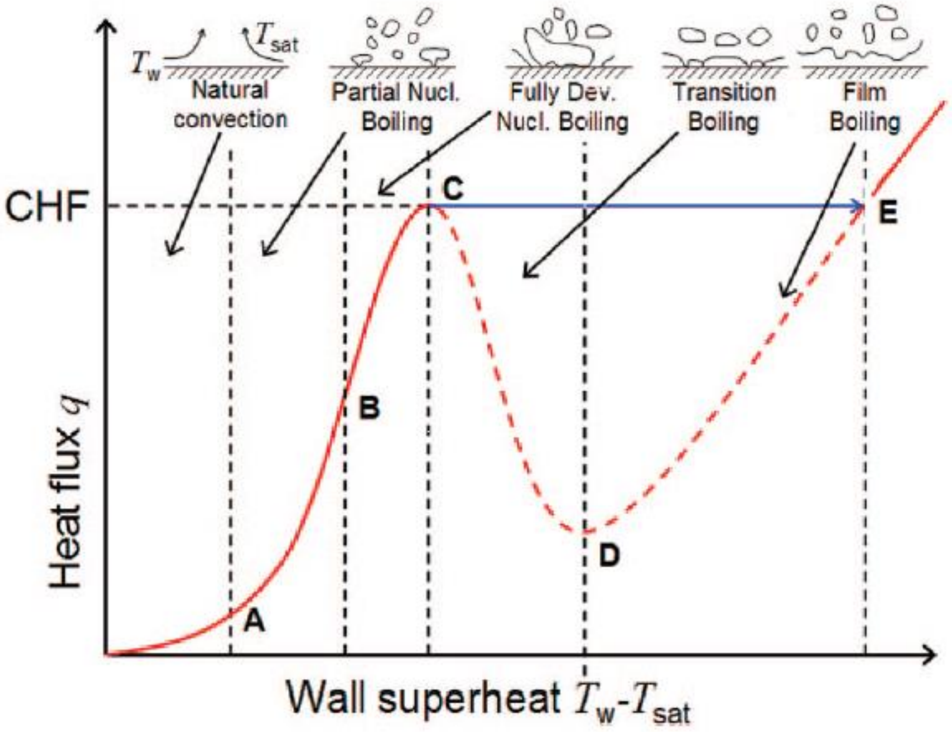

Figure 13: Pool boiling curve [32]

This regime has very high heat transfer rates and is the most important regime from the electronics cooling perspective. Increase in surface temperature is caused by increase in heat flux up to point C. Beyond this point, surface temperature increases by orders of magnitude without increase in heat flux and causes the wire to melt and burn out. This occurs due to the vapor bubbles agglomerating over the surface and forming a vapor blanket that impedes heat transfer to the pool liquid. Therefore the heat flux at point C is called burn out heat flux or critical heat flux (CHF). The heat transfer mechanisms beyond point C are of little importance to electronics cooling applications, as the surface temperatures beyond this point are higher than the melting point of solder metals used in the electronic packages, and therefore cause electronics to fail. Therefore to further improve the heat dissipation capability of two-phase immersion cooling systems, the CHF value must be increased. To reduce the surface temperature for a given heat dissipation, the slope of the fully developed boiling regime, the regime in which the immersion cooling solutions would be operating, must be increased.

2.3 Tailored Surfaces for Improving Boiling Heat Transfer

Several studies have recorded the improvements in CHF and heat transfer coefficient brought about by tailored surface enhancements. One of the earliest studies was performed by Berenson [33], who investigated the effect of surface material, roughness and cleanliness on pool boiling characteristics of n-pentane. In this study in which nickel, copper and inconel were used as surface materials, it was found that the nucleate boiling heat transfer coefficients changed by up to 600% with change in surface characteristics. The burnout heat flux or CHF, however, was independent of surface material, roughness or cleanliness. The role of surface enhancements on two-phase liquid cooling of electronics was investigated as early as 1974 by Oktay and Schmeckenbecher [34]. In this study, thermal performance of a dendritic heat sink made from nickel powder was compared to a solid heat sink and with the plain chip surface. The use of dendrite structures reduced the temperature overshoot at nucleation, as the dendrite structures started to nucleate at heat input of 0.5 W compared to the plain surface that nucleated at 3 W and had a surface temperature of 70°C. Following this study, surface enhancements with micro- and nano-scale features have been studied for performance improvement of electronics cooling applications.

The presence of micro-scale porosities offers higher heat transfer rates, as the area to volume ratio in comparison to the plain surface is higher, along with increased nucleation density. In addition, CHF improvement also happens due to reason that these porosities facilitate boiling and two-phase flow within the surfaces. A traditional method of creating porous surfaces is by bonding of metal particles to form a thin surface on a base metal. Chien and Chang [35] investigated the effect of particle size and coating thickness on the evaporation resistance of test surface with water as working fluid under sub atmospheric conditions. Based on the results, they concluded that the best boiling performance and low evaporation resistance is achieved when the coating thickness to particle diameter ratio is 3.85. Campbell and Tuma [36] investigated the effect Boiling Enhancement Coating (BEC) on immersion cooling system by performing numerical simulations of the dual core POWER6 processor from IBM p575 supercomputer. By applying experimentally determined boiling heat transfer coefficient as convection boundary condition, they concluded that the immersion system with BEC would provide lower system resistance and in certain cases a lower junction temperature than the cold plate system that was used as the cooling solution in production IBM p575s. Using surfaces with the same BEC, Moreno [37] conducted experiments on 1 cm^2 horizontal surfaces with HFC-245fa as working fluid. The results from these experiments show that the use of BEC can provide up to 430% increase in heat transfer coefficients and 50% increase in CHF compared to the plain copper surface. By using the Boiling Enhancement Paint patented by You and O’Connor [38], the patent authors achieved a 109% increase in CHF and up to four times increase in heat transfer coefficients for a surface coating with silver flakes in comparison to a plain aluminum foil surface [39]. O’Connor et al. also developed a dielectric paint with diamond particles and painted it on to a silicon surfaces. This painted silicon surface showed a 224% improvement in CHF over non-painted surface, when operating at 45 K subcooling condition [40]. Using the Aluminum Particles/ Devcon Brushable Ceramic epoxy/Methyl-Ethyl-Keytone (ABM) coating developed using the same patented coating technique, Rainey and You [41] performed pool boiling experiments on copper surfaces with FC-72 as working fluid. The tested surfaces include plain, plain with microporous coating, surface with square pin-fin array and pin-fin surfaces with microporous coating. The fin length was also a variable for both the pin-fin surfaces. The results indicate that the pin-fin surface with microporous coating and a fin length of 8 mm has the highest CHF recorded in the study with a value of 129.4 W/cm². Under similar conditions, the plain, uncoated surface has a CHF of 18.8 W/cm². The fin surface with microporous coating also has about a 41% higher CHF than the uncoated pin fin surface. Pool boiling experiments on silicon surfaces with diamond-base microporous coating was performed by Arik et al. [42] using FC-72 as working fluid for 1-3 atm system pressures and 0-72 K subcooling. The test system used the ATC 2.6 chip package with square die surface measuring 6.4 mm on side. The results indicate CHF values of up to 47 W/cm² for the coated surface under 3 atm pressure and 71.5 K subcooling, compared to the CHF of 34.6 W/cm² for uncoated surface operating under similar conditions. Under other conditions, CHF enhancement of up to a factor of 2 was observed for the coated surface. Parker and El-Genk [43] compared the pool boiling performance between smooth copper and porous graphite surfaces with FC-72 as working fluid. For subcooling values of 10 K, 20 K and 30 K, the porous graphite surface has 63-94% higher CHF values than the smooth copper surface. In addition, the porous graphite surface does not have temperature overshoot during nucleation incipience compared to the 9-14 K overshoot in copper surfaces, and has higher heat transfer coefficients than the smooth copper surface.

In addition to microporous coatings, many studies have also investigated the boiling performance improvement achieved with the introduction of finned surfaces. These surfaces offer higher heat transfer area in single-phase regime that improves the heat transfer coefficients compared to the plain surface. In two-phase regime, these surfaces have higher surface area for nucleation, and therefore improve the nucleation density and two-phase heat transfer coefficient. These surfaces also offers nucleation at the fin surface at higher heat flux values, even when the base surface has vapor agglomeration. Honda et al. [44] conducted pool boiling investigations with FC-72 liquid on silicon chips with four different surface characteristics – plain smooth, plain rough, smooth micro-pin-fin and rough micro-pin-fin surfaces. The results show that the smooth micro-pin-fin surface has up to 2 times higher CHF than the plain smooth silicon surface. The micro-pin-fin surface with submicron roughness has the highest CHF of all the surface characteristics, with up to 2.3 times higher CHF than the plain smooth surface. Yuan et al. [45] performed similar investigations for a flow boiling configuration with FC-72, using a plain and two different micro-pin-fin surfaces with 60 and 120 μm fin heights. The results show that the fin surfaces with 120 μm have the highest CHF, with 60% higher than the plain surface. The fin surfaces with largest fin height also showed a higher response to CHF increase with increase in flow rate.

With developments in nano scale manufacturing, two-phase thermal performance enhancement brought about by the inclusion of nano level surface features has been the focus of several investigations. Ujereh et al. [46] compared the pool boiling performance of plain silicon surface and Carbon Nano-Tube (CNT) coated surfaces. The results show that more than 35% improvement in CHF and 65% reduction of wall superheat can be achieved with a light array of fully CNT coated silicon surfaces. FC-72 was used as the working fluid in this study. Chen et al. [32] used arrays of copper and silicon nano wires as surface enhancement in a pool boiling study with deionized water as working fluid. Compared to the plain silicon surface with a CHF of about 80 W/cm², the surfaces with nano wires achieved a CHF around 200W/cm². The heat transfer coefficient of the nano wire surfaces was twice that of the plain silicon surface.

In summary, a review of studies that employed tailored surfaces in two-phase systems reveals that the use of surface enhancements improves boiling heat transfer in both pool boiling as well as flow boiling configurations. Most of the studies reviewed used dielectric fluids, fluids that have properties comparable to the dielectric fluid used in the current study. Also apparent is the effect of parameters such as subcooling and flow rate, which have the effect of further improving the thermal performance of these enhanced surfaces.

2.4 Boiling Performance Enhancement Studies in Electronics Cooling

The wide range of cooling requirements in electronic systems spanning different sizes and designs, and the highly local nature of two-phase heat transfer makes the two-phase electronics cooling less amenable to being numerically modeled and systematically generalized. Consequently, a significant portion of the literature has been gathered from experimental investigations. This section presents some of the studies that have been done in the domain of two-phase immersion cooling. Other techniques in two-phase cooling such as microchannels and spray cooling that are also actively being investigated, but a detailed discussion on these studies would be lengthy and out of the scope of this section.

2.4.1 Pool Boiling

The system in which the electronic packages are immersed in a pool of dielectric fluid maintained at a specified temperature is generally referred to a pool boiling system. The temperature of the fluid can be maintained at its saturation temperature or at a subcooled temperature. Using the same experimental setup discussed in this study Gess et al. [47] performed pool boiling investigations for three different surfaces – bare silicon, microporous and microfinned. The thermal performance between FC-72 and Novec 649 fluids were compared and the different subcooling values for these dielectric fluids were also tested. Heat flux values of up to approximately 14 W/cm² were achieved for the microfinned surface at the highest subcooling used in the study. Using similar surface enhancements but in a more conventional pool boiling setting, Sridhar [48] achieved heat flux values of up to 47 W/cm² with the microfinned heat sinks. The change in thermal performance of a chip due to the presence of neighboring dies in a multi chip module was also investigated in this study. The pool boiling studies by Ramakrishnan [49] using Novec 649 and HFE-7100 fluids also investigated the thermal performance of microporous and microfinned heat sinks, and reported highest heat fluxes in the neighborhood of 20 W/cm² for the microporous surfaces. This study also investigated the effect of fluid contamination by intentionally contaminating the working fluid with dioctyl phthalate. The results show that the microporous surface had the highest loss of performance with increase in superheats of up to 10°C. The microfinned heat sink was recommended to be used in operations prone to fluid contamination, as the large feature size has higher resistance to contamination and also offers better performance than the bare silicon surface. Other recent studies on pool boiling include the investigations by Jaikumar and Kandlikar [50], in which the surfaces with open microchannels along with porous fin tops were employed to achieve 270% enhancement in CHF compared to the plain surface. Copper surfaces (20 mm x 20 mm), in a horizontal orientation, with centrally machined 10 mm x 10 mm microchannels were used in this pool boiling study.

FC-87 was used as the working fluid. Five different test sections, each with a unique combination of channel width and depth were tested to determine the effect of channel geometry on boiling performance. The ratio of channel width to depth was identified to be an important parameter, and the highest performance recorded in this study was for a ratio of one. CHF values in the neighborhood of 65 W/cm² were reported by El-Genk [51], for upward facing microporous copper surfaces (10 mm x 10 mm) at 30K subcooling of the PF-5060 dielectric liquid. The other parameters tested in this pool boiling configuration include surface characteristics, working fluid, subcooling and surface orientation. Thiagarajan et al. [52] conducted pool boiling experiments with plain and microporous surfaces in a horizontal orientation, using HFE-7100 as working fluid. Two plain surfaces with different surface roughness values and three microporous surfaces with different coating thickness values were tested in this study. The results show up to 60% increase in CHF value for the microporous surface with smallest coating thickness, in comparison to the plain surfaces.

It must be noted that while the studies reviewed above show the effect of different parameters on the thermal performance of the pool boiling system, a direct comparison between these studies cannot be made due to the large differences in the volume of the pool. While the studies by Sridhar [48] use a large pool that is similar to OBI approach, the studies by Gess [47] use a relatively smaller pool. Therefore, the highest heat flux values alone cannot be used to quantify the performance of the system. Nevertheless, it can be observed that for any pool boiling system, employing tailored surfaces and increasing the degree of subcooling will result in higher heat dissipation compared to a system with a plain surface and a saturated pool.

2.4.2 Flow Boiling

In a flow boiling system, a fluid delivery system directs the dielectric fluid over the heated surfaces, which can be either in a fluid pool or a narrow channel. The fluid flow rate is an important parameter in this configuration. Flow boiling investigations for a vertical configuration similar to that of the current study were performed by Mudawar and Maddox [53], in which FC-72 was used as the working fluid. The copper test surfaces measuring 12.7 mm x 12.7 mm were mounted in a narrow rectangular channel. The results showed that the fluid velocity and subcooling of the fluid had a significant impact on the CHF of the system. Two different CHF regimes – low velocity and high velocity regimes were identified and a correlation for low velocity CHF was proposed. Using the same system, but with different surface characteristics CHF values of up to 361 W/cm² was achieved in this system [54]. Willingham and Mudawar [55] further extended the flow boiling analysis to an array of nine 10 mm x 10 mm copper heat sources simulating microelectronic chips. The chip far away from the fluid inlet was the first to achieve nucleation incipience, generally monotonously followed by the lower upstream chips. Subcooling and flow rate were found to increase the onset of CHF and nucleation incipience for all the surfaces. In order to improve the uniformity of the boiling activity of the multiple chip surfaces, other heat sources were recommended to be placed beneath the multichip arrays. Rainey et al. [56] performed flow boiling experiments on plain and microporous copper surfaces with FC-72 as working fluid. The test surfaces, measuring 10 mm x 10 mm were placed horizontal in a square channel measuring 12.7 mm in side. In this study, the effects of subcooling and flow rate were also investigated. CHF values of around 85 W/cm² were recorded for the microporous surface, for the highest subcooling and flow rate used in this study. For the plain surface, the CHF increased from around 15 W/cm² for the lowest subcooling and flow rate, to around 70 W/cm² for the highest values. Yuan et al. [45] performed experiments with 10 mm x 10 mm silicon chip using FC-72 fluid. In this study in which the chip is horizontally placed in a rectangular channel, the effect of subcooling and flow rate were investigated. One plain surface and two different types of micro-pin-finned surfaces were used as test surfaces. CHF values of up to 145 W/cm² were achieved with the micro-pin-finned surface, for the highest subcooling and flow rate values used in this study. With the same experimental setup discussed in the current study, but with a different flow distribution system, Gess et al. [47] performed flow boiling experiments on two different surfaces using Novec 649 as working fluid. In this system with vertically oriented surfaces, the effect increasing flow rates was also investigated. The results show roughly 22% increase in heat dissipation for the microfinned surface and 19% increase for the microporous surface, in response to the increase in flow rate.

Collectively, the aforementioned studies show that the flow rate has a substantial impact on the thermal performance of systems that employ dielectric fluids and have small heater surfaces similar to the heat dissipating elements in electronic systems. Once again, as with the case of pool boiling, comparison between these flow boiling studies cannot be performed, as most of these studies employ a narrow channel configuration, while the studies by Gess [47] and the current study use a cartridge configuration.

2.5 Impingement Boiling

The two-phase technique in which the fluid flow is directed toward the surface is called impingement boiling. The free jet system is one in which the liquid jet impinges on a surface that is surrounded by a gaseous environment. If the surface is submerged in the same cooling fluid as that of the jet, the configuration is referred to as submerged jet system. If the surface is submerged, but the liquid surrounding the nozzle is constrained by an upper wall, this configuration is referred to as confined jet system. These systems are shown in Figure 14. The fluid field in the impingement system has different regions as shown in Figure 15. The flow region that is not affected by the presence of the impingement surface is called the free jet region. The flow out of the jet is marked by a presence of an inviscid region called the potential core. As the flow moves away from the jet orifice, the momentum exchange between the fluid from the jet and the surrounding fluid increases the free jet boundary, and the potential core contracts. As the jet flow approaches the impingement surface, the fluid decelerates in the z-direction and accelerates in the r-direction. This region called the stagnation region and the stagnation point has the highest local pressure in this region. As the flow moves point in the transverse (r) direction, it continues to exchange momentum with the surrounding fluid. For the submerged jet configuration, the velocity profile of this transverse wall jet region has no slip boundary condition at both free jet and impingement surfaces.

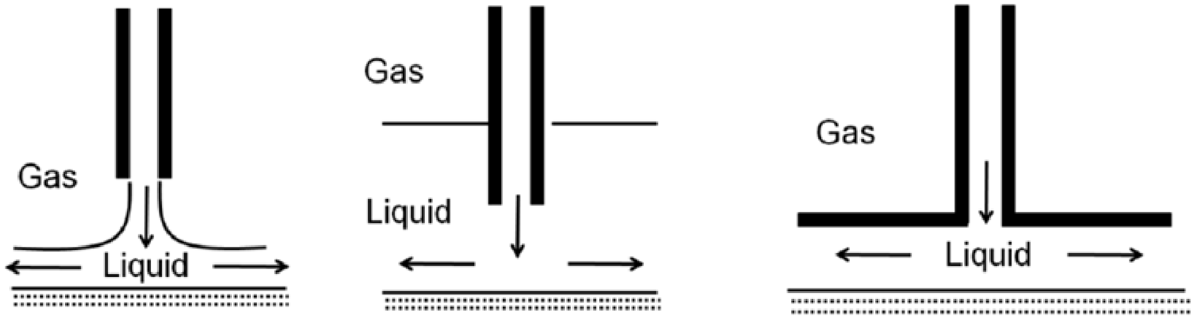

Figure 14: (Left to right) free, submerged and confined jet configurations [57]

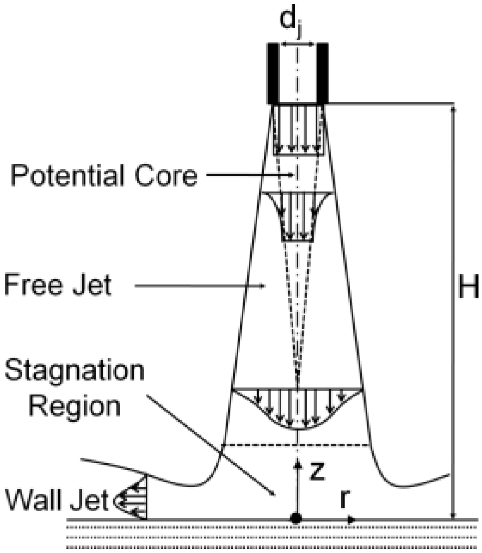

Figure 15: Different regions in a submerged jet configuration [57]

Some of the earliest studies on jet impingement boiling for electronics cooling applications were performed by Ma and Bergles [58], with the experiments on 5 mm x 5mm and 3 mm x 3mm test surfaces using R-113 as working fluid. Two different jet orifice diameters were used and the effects of flow rate, subcooling and surface aging were also studied. The results indicated that the overshoot at nucleation incipience was reduced by increase in both flow velocity and subcooling. The boiling curves for different flow rates merged into a single curve in the fully developed boiling regime, but the curve for subcooled boiling was shifted leftwards to the saturated boiling curve. It was also found that surface aging had a positive impact on the boiling performance. Chrysler et al. [59] performed free and submerged jet studies on 6.5 mm square chip surface with FC-72 as working fluid. Two different flow rates and four different types of jets were tested in this study. All the jets had an orifice diameter of 0.5 mm. The jet orifice to chip distance was also a variable that was studied, and two different approaches – jet pin and jet piston arrangements were implemented in adjusting this distance. The results showed up to 120 W/cm² CHF values for a flow volumetric rate of 2.2 cm³/s. For this flow rate, the average surface temperature of the chip relatively remained unchanged for orifice to chip distance greater than 1.75 mm. For values below this gap distance, the average temperature increased with decreasing gap distance. It was also observed that the performance of jet piston approach was comparable to that of the jet pin approach. Cardenas and Narayanan [60] conducted jet impingement boiling experiments for an unconfined submerged jet configuration, in which the FC-72 working fluid was maintained at its saturation temperature. The effects of jet nozzle diameter and the jet Reynolds number were also studied in this experiment. A horizontally oriented circular copper heater measuring 27.64 mm in diameter was used as the test surface. The results show that the impingement configuration has boiling enhancement of up to 1.44 times compared to the pool boiling configuration. The highest CHF values reported in this study are in the neighborhood for 20 W/cm², for the smallest jet nozzle diameter working at highest jet Reynolds number. The effect of surface enhancements in two-phase impingement was investigated by Copeland [61], in a study on submerged jet impingement boiling on plain and pin-fin copper surfaces with a 1cm x 1cm base. In this study that used FC-72 as working fluid, the test parameters include pin-fin geometry, flow rate, nozzle diameter, and number of nozzles. CHF values from 45 W/cm² to 395 W/cm² for the combination of parameters tested. Correlations for single-phase heat transfer coefficients and CHF based on the aforementioned parameters were also provided in this study. Ndao et al. [62] performed impingement experiments on a 64 pin-fin array etched to a silicon substrate with R134a as working fluid. Three different pin-fin geometry profiles – circular, square and hydrofoil were tested in this study. These profiles are shown in Figure 16. The effects of flow rate, saturation pressure and surface aging were also investigated in this study and were found to have significant impact on boiling performance. The results indicate heat transfer coefficients of 150,000 W/m²K for the circular pin fins, and heat fluxes values of up to 275 W/cm² for the hydrofoil fins. The effects of surface characteristics on impingement boiling performance were also investigated by Rau and Garimella [63], for a confined submerged jet configuration. In this study that uses a single 3.75 mm jet, HFE-7100 is used as working fluid. Four different surface characteristics for the copper surfaces -- smooth, microporous coated, macrofinned and macrofinned with microporous coated pin fins were tested in this study. The base area of the copper surface was 25.4 mm x 25.4 mm. The effect of three different flow rates was also studied in these tests. The results indicate that the finned surface provide the highest CHF improvement, with the plain pin-fins providing up to 2.13 times enhancement and the coated pin-fins providing up to 2.42 times enhancement compared to the plain surface. The highest enhancement provided by the plain microporous coated surface in comparison to plain surface is 1.51. The highest CHF reported in this study is 88.3 W/cm² for the

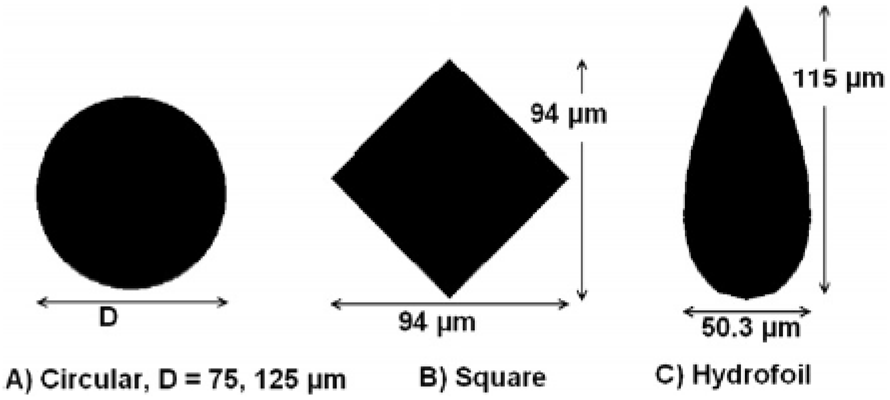

Figure 16: Fin profiles used in the study by Ndao et al. [62]

macrofinned surface with microporous coating at the highest flow rate used in the study. Jet impingement performance of a multichip arrangement was investigated by Mudawar and Wadsworth [64], for a 3 x 3 array of simulated copper chips cooled in a channel by FC-72 fluid. The effects of jet width, the height of the channel and impingement velocity were also investigated in this study. The results showed that the jet impingement system could maintain uniform heat fluxes and surface temperatures across 9 chip surfaces, and provide heat flux values of up to 250 W/cm^2 [65].

In summary, the submerged two-phase jet impingement system can provide large heat dissipation values for applications in electronic thermal management. In addition to parameters such as surface characteristics, subcooling and flow rate at the nozzle exit, careful understanding of additional parameters such as jet configuration, size of the jet, number of jets and the effect of fluid interaction between multiple jets is highly essential in designing these systems.

2.6 Nucleation Suppression in Flow Boiling

In two-phase heat transfer, depending on the surface characteristics and other parameters such as subcooling, system pressure and other fluid properties, a certain thermal boundary layer thickness is required to initiate and sustain the nucleation activity. If the boundary layer thickness is not sufficiently large, the embryonic bubble will not be allowed to develop. This phenomenon of having a boundary layer thin enough that it cannot support nucleation is called nucleation suppression. For flow boiling in tubes and channels, nucleation suppression happens in saturated flow boiling. The increasing void fraction and acceleration transitions the flow from slug flow to churn flow and finally to annular flow regime. These regimes are shown in Figure 17. This transition changes the heat transfer mechanism from vigorous nucleate boiling to liquid film evaporation as the flow moves downstream. At some point, the liquid film is thin enough that the nucleation activity is suppressed. Increasing the mass flux or flow rate of the fluid flowing on a surface also decreases the thermal boundary layer thickness, and this can be used to suppress the nucleation activity. This phenomenon was studied by Thorncroft et al. for flow boiling on a vertical flat surface [66]. FC-87 was used as working fluid and a rectangular nichrome strip was used as the test surface in this study. The suppression point was determined from the flow boiling curves, by finding the intersection point between the convection regime that has a constant slope and the boiling regime that has a varying slope. The effects of different inlet vapor quality and flow direction on nucleation suppression were also investigated in this study. The results were used in calculating a dimensionless ratio of maximum to minimum cavity size, which would indicate if nucleate suppression is possible. The correlation between this dimensionless variable and nucleation site density and the transition from convection to boiling regime were also discussed in this study.

2.7 Flow Visualization Techniques

To improve the performance of the two-phase cooling systems, knowledge of mechanisms that drive and limit the boiling heat transfer is highly essential. This is often achieved by performing high-speed imaging studies to capture the bubble characteristics such as the departure diameter, frequency and nucleation site density. Knowledge on flow field is also highly important, as the boiling performance is directly linked to the ability of the cold fluid to quench the surface. The design of two-phase systems must be done with care, with a special focus on the layout of the components. A design with components obstructing proper fluid circulation will diminish the thermal capability of the system. Particle image velocimetry (PIV) can be used to understand the flow field of a fluid system. PIV is a technique that creates flow field by tracking the motion of laser illuminated particles that move with the fluid. Early studies on the concept and application of this technique in fluid mechanics were performed by Meynart [68], who showed that the technique could be applied to two-dimensional fluid domain, and then extended it to more complex flows. Arghode et al. [69] applied this technique for flow

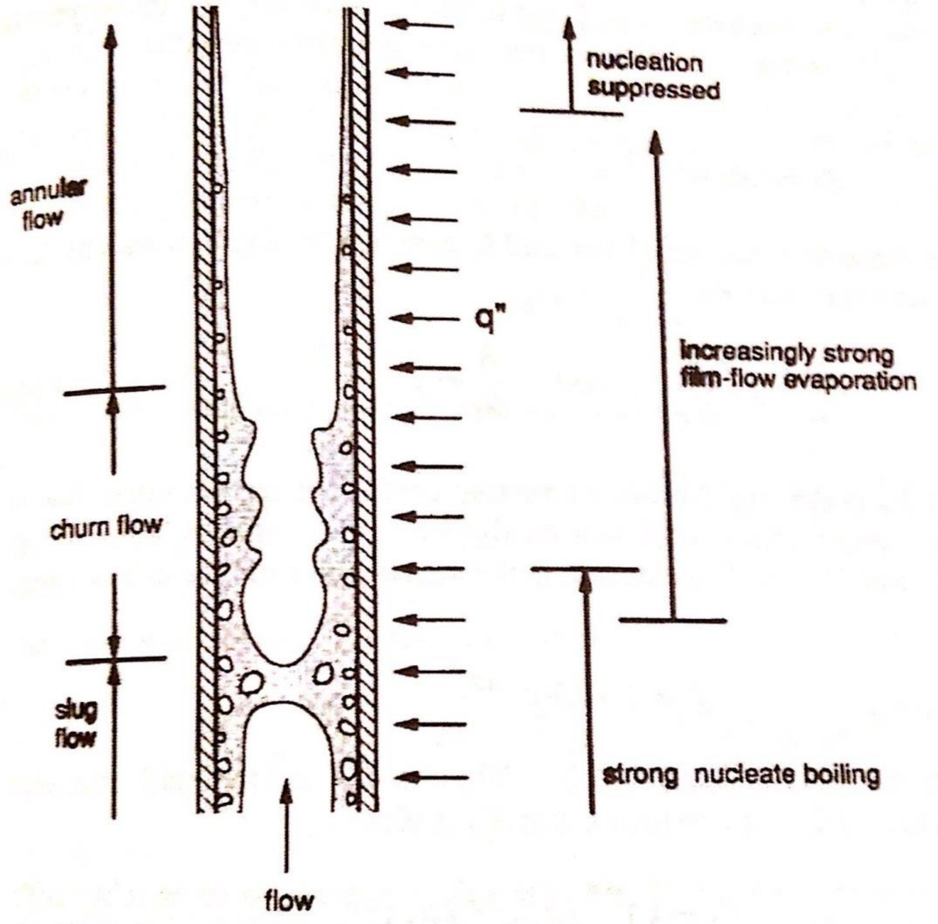

Figure 17: Nucleation suppression in flow boiling [67]

visualization of the air through a perforated tile. The PIV results were compared with computational fluid dynamics (CFD) results, and the findings were used in developing new CFD strategies to improve the accuracy of the models. Pavlova and Amitay [70] used PIV in synthetic jet impingement system to generate the velocity fields, and used these velocity fields to create mean vorticity fields. The vorticity fields of jet impingement at two frequencies -- 420 Hz and 1200 Hz were used to study the characteristics of the vortices in the flow field for each frequency. The PIV technique for smaller length scales called micro-PIV or µ-PIV, was used in the study of wavy microchannels by Gong et al. [71], and the PIV measurements were found to have good agreement with the CFD results. For the Re number range of the experiment, both µ-PIV and CFD results also showed no secondary or re circulating flow within the channel. Using the same experimental setup discussed in this study, Gess et al. [47] performed single-phase PIV experiments for the flow boiling configuration for two different types of flow distributors. Measurements taken at three slices 5 mm apart were used in determining the mass flow rate over the heated surfaces for each flow distributor design. Comparison of these results aided in determining the optimal flow distributor. Further improvement was achieved through the implementation of flow guides, which improved the thermal performance by increasing the fluid flow to the heated surfaces. The PIV images before and after the flow guide implementation are shown in Figure 18. Gess also performed two-phase PIV experiments, but for the pool boiling configuration. As the bubbles in two-phase system can also reflect the incident laser light as the particles, a filter was used in the image capture system to remove the light reflected from these bubbles. The results from the two-phase PIV experiments were used in determining the map that shows the quenching coolant entry points in this pool boiling system. This map is shown in Figure 19.

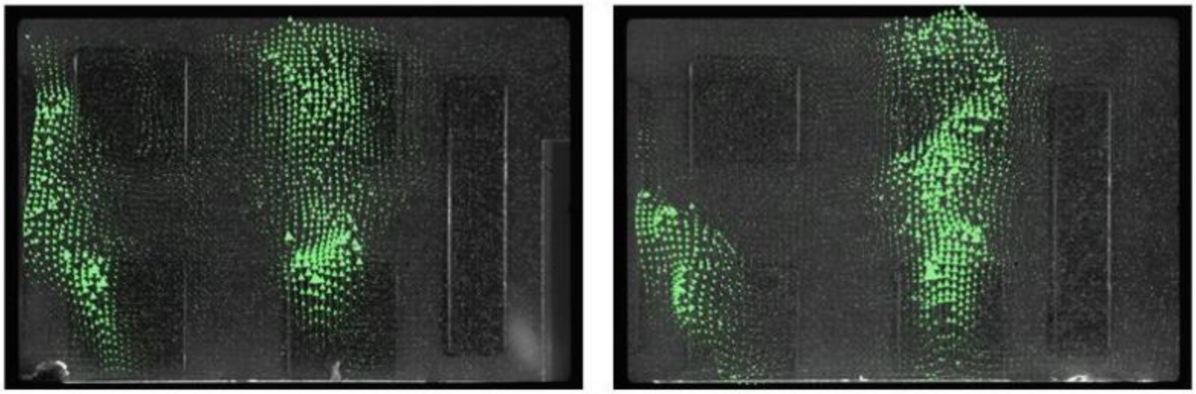

Figure 18: Single-phase PIV images with (left) and without (right) flow guides [47]

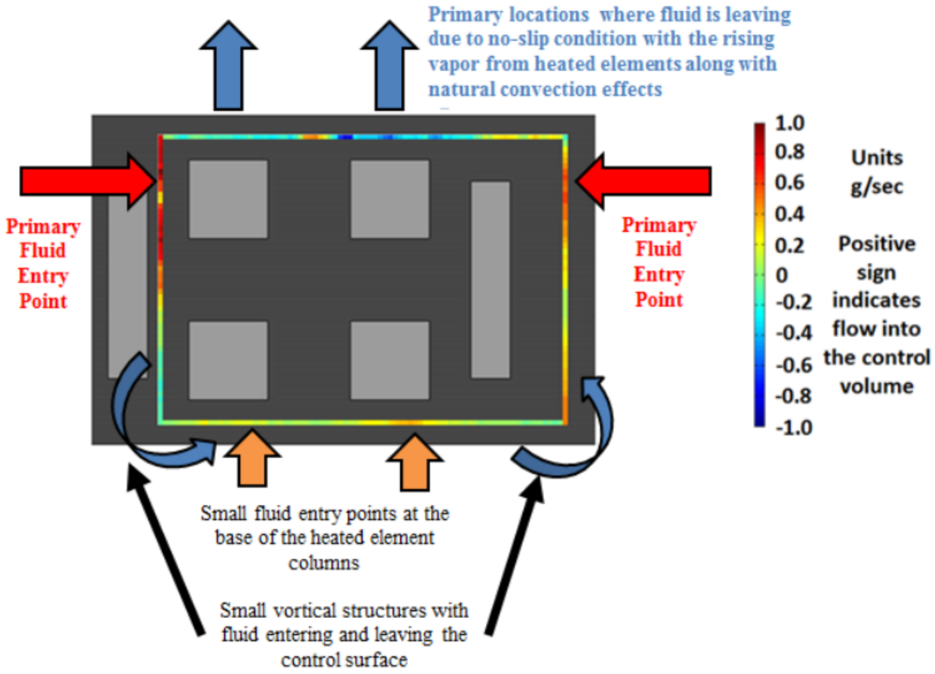

Figure 19: Flow map generated from two-phase PIV showing coolant entry points [47]

2.8 Objectives of this Study

With the air cooling technique approaching its limit in cooling high-power electronics, the industry is increasingly adopting liquid cooling solutions such as cold plates and rear door heat exchangers. While these techniques mitigate some of the problems associated with traditional air cooling methods and offer improvements in heat dissipation and energy-efficiency, the heat transfer paths of these systems have multiple resistances from the junction to the cooling fluid that limit their cooling potential. The liquid immersion systems have lower system level resistances, as the cooling fluid is in direct contact with the heat dissipating surface. This feature and other advantages of two-phase cooling have resulted in increased commercial interest in OBI cooling solutions. While these OBI solutions dramatically reduce the footprint of the data center facility compared to air cooled facilities, they often use a large fluid inventory of expensive dielectric fluid in their cooling systems. Leakage or contamination of cooling fluid, or other issues with the large tank containing the fluid will render multiple server blades inoperable, which may significantly reduce the productivity of the datacenter facility. In contrast, a modular cooling paradigm with an individual cooling system for each blade will result in a substantial reduction of the fluid inventory. The use of quick disconnect couplings for fluid and electrical connections will enable easy line replacement, which will make it possible to perform a quick swapping of server blades when one particular blade needs maintenance or repair. The system discussed in this study is a small form factor, line-replaceable cooling module that was developed based on the aforementioned idea. This system has a fluid inventory of less than 2L, and has the capability to operate in flow boiling configuration.

The objective of the current study is to investigate the flow boiling characteristics of this server cooling module. From the review of boiling studies in electronics cooling, it can be concluded that the flow boiling performance can be improved by employing tailored surfaces, and increasing the subcooling and flow rate of the dielectric fluid. This study will quantify the thermal performance improvement brought about by varying the aforementioned parameters. In a preliminary effort understand the impact of impinging flow on the thermal performance of this system; this study will provide the heat transfer characteristics of the configuration that delivers an impinging flow to some of the surfaces. These studies will employ high-speed imaging to understand the qualitative changes in the nucleation characteristics brought about by varying the parameters. The nucleation suppression phenomenon in flow boiling will be investigated, and the implications of different surface characteristics and flow distributors will also be studied.

Chapter 3: Experimental Setup

The section describes the construction and operation of the experimental setup used in conducting this study. Details of the testing elements used to simulate the processing and memory modules, the cartridge enclosing these elements and the fluid systems used in removing the heat dissipated from these surfaces are provided. The key aspects of the surface enhancements used in improving the two-phase heat transfer performance are discussed. Details on hardware and essential parameters used in high-speed imaging are also provided.

3.1 Enclosure Assembly

The cartridge that encloses the electronics assembly is the main component of this experimental setup. The primary component within this enclosure assembly is an aluminum housing with the dimensions of 150 mm x 300 mm x 38 mm (H x L x W). Figure 20 shows the enclosure assembly. The housing is milled out of a solid aluminum block rather than being a welded assembly, in order to avoid cracks that might lead to the leakage of the highly wetting dielectric fluid contained in the assembly. Also, the single piece design avoids contaminants entering the cartridge, especially water, as Novec 649 dielectric fluid used in this study forms an acid when it mixes with water. Another reason for this single piece design is to improve the heat transfer between the condenser pin fins inside the cartridge and the coolant channels on top of the cartridge, by improving the contact between the surfaces. Figure 21 shows the coolant channels and the pin fin condenser milled out of the cartridge. If constructed separately,

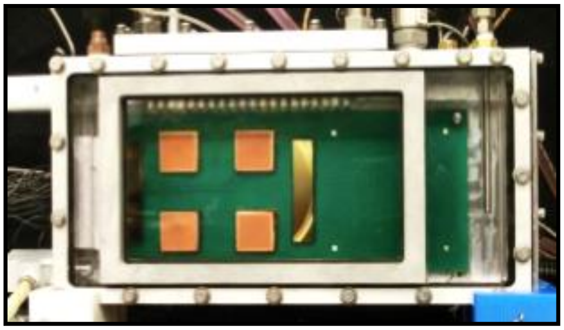

Figure 20: Enclosure assembly

this channel - condenser assembly would have higher contact resistance, and the introduction of a Thermal Interface Material (TIM) to reduce this resistance may bring compatibility issues with dielectric fluid. A mixture of deionized water and Dowtherm SR-1™ fluid is the system level coolant used in this setup. This coolant will be referred here on to as Chilled Water (CW). Ethylene-Propylene-Diene-Monomer (EPDM) gaskets provide sealing for the components

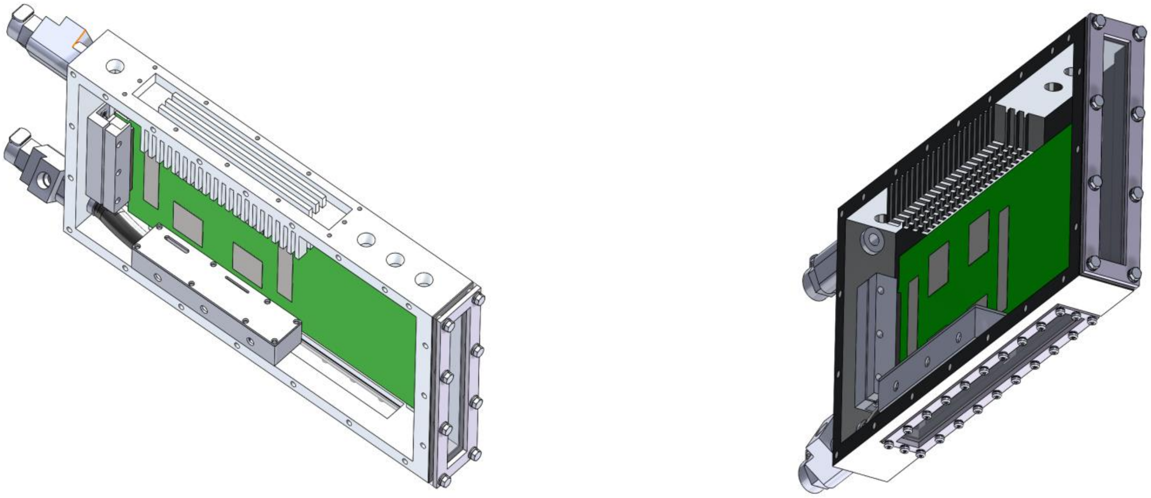

Figure 21: Coolant channel (left) and pin fin condenser (right) on top of the enclosure

attached to the housing. For visualization of flow field and the boiling activity, transparent polycarbonate viewing windows are placed on the front, bottom and right faces of the enclosure assembly.

A Graham condenser is mounted on top of the enclosure assembly to maintain the internal pressure of the enclosure to be as close to ambient pressure as possible, as the increase in system pressure would increase the saturation temperature of the dielectric fluid, which in turn would increase the surface temperature necessary to start the boiling process which offers high heat transfer rates. Considering the small temperature budget of the electronic devices and the adverse effect the increased chip junction temperature has on reliability of electronics, increasing the surface temperature required to the reach boiling regime is not preferable. The Graham condenser also has chilled water connections to condense any vapor leaving the system. However, from sensible heat gain analyses, it was concluded that the cooling loop to the Graham condenser does not provide significant heat removal from the system [47].

The Printed Circuit Board (PCB) housed within the cartridge and immersed in dielectric fluid, contains the heating elements that simulate the power dissipating devices in computing devices. These PST4 series test cells from Kokomo Semiconductors© each measuring 0.25" x 0.25" (6.32 mm x 6.34 mm), are mapped into four square test sections to simulate the high power dissipating processing elements, and two rectangular test sections that simulate low power density Dual Inline Memory Module (DIMM). Each of these test cells have resistance heaters for controlled heat dissipation, and a five-diode array which is connected to the Data Acquisition (DAQ) system for temperature measurement. Figure 22 shows the circuit diagram for a test cell with heating and temperature measurement provisions. Power is supplied to the resistance heaters in the test cells through a constant current source from an AMREL ™ SPS series power supply. Temperature measurements are conducted by exciting the five-diode array with a 2.2 mA current from a Keithley© Model 2401 source meter, and then measuring the voltage drop across the diodes. The voltage drop is proportional to the temperatures of the test cells with a sensitivity of 10 mV/°C. The arrangement of these test cells into heaters on to a PCB, along with the spacing between heater surfaces is shown in Figure 23. Leak proof electrical connections for power and signal into the cartridge is achieved through the MIL-STD-83513 100-pin connector from the Glenair© 177-705H series. This connector press fits with the Glenair GMR 7590 series connector mounted on the PCB inside the cartridge. The power and signal then travel through the traces in the three layer PCB to reach the test cells through solder bump node vias penetrating through the PCB. Although there are 100 connections out of the PCB, this is still not sufficient to connect all the test cells to the source meter and DAQ system for temperature measurement. Therefore, temperature measurement is performed only at fourteen points, as shown by the

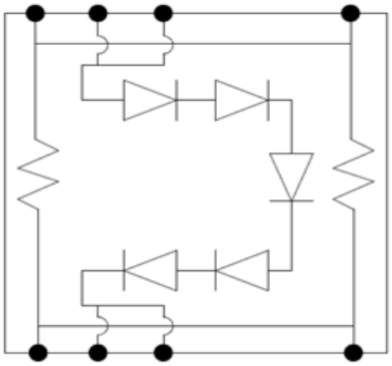

Figure 22: Circuit diagram of the thermal test cell

numbered cells in Figure 23. Furthermore, the inevitable failures in some of these temperature measurement points due to manufacturing problems and also the DAQ system limitations meant only certain diodes were functional for temperature measurement. Table 1 shows the list of these functional diodes for three different test vehicles used in this study.

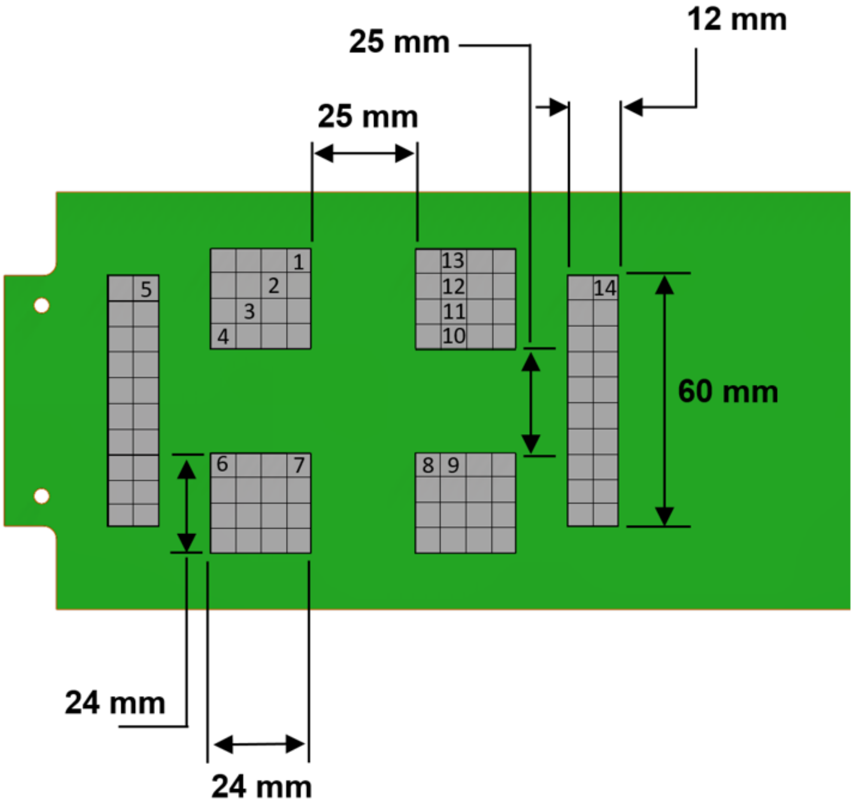

Figure 23: Test cell arrangement and PCB layout

Table 1: Diode Temperature Measurement Locations

Surface	Active Diode locations from Figure 23
Bare Silicon	2,3,4,6,7,8,9,11
Microporous	2,3,6,7,8,9,10,12,13
Microfinned	2,4,6,7,8,9,10,11,12

Experiments in measuring thermal performance of the system were performed by varying the power input into the system, and measuring the corresponding surface temperatures from the temperature measurement points. The temperature measurement was carried out after the system was assessed to be in steady-state. For a constant current supplied, from Ohm's law, the stabilization of voltage drop across the surfaces indicate that the resistance of the heaters have stabilized. This stable resistance in turn implies that the surface temperatures have stabilized. This voltage stabilization criterion is implemented through a feedback loop written in the DAQ programming language. The voltage drop values are recorded for 2 minutes at a sampling rate of 1 kHz, and these values are then averaged. The DAQ program repeats this measurement and averaging step, and compares it with the previous value. When the difference is less than the set difference value, the program performs temperature measurements. The value of this voltage difference was set at 1.5 mV, based on the measurements to determine this criterion [47]. While the system satisfied this difference typically within 1-3 iterations in the boiling regime, the steady-state in the convection regime is usually based on the execution of this voltage drop check for a specified maximum number of iterations. Details of the DAQ system, such as wiring layout and LabVIEW virtual instrument (VI) are presented in Appendix-B. The temperature measurement diodes were calibrated using a NIST–traceable thermistor with an accuracy of ±0.01°C. Each of the three test surface vehicles has individual calibration curves. Details on calibration can be found in the study by Gess [47]. The enhanced surfaces were calibrated after adding enhancement heat sinks. The overall uncertainty for the thermal test cell's temperature measurement was determined to be ±0.09°C. The uncertainty in heat flux measurement was calculated to be ±0.23 W/cm². Details of the uncertainty calculations can be found in the previous study performed on this setup [47].

Located in the bottom of the cartridge is a flow distribution system that directs dielectric fluid to the surfaces that simulate processing elements. Cold fluid enters from bottom connection located on the left side of the cartridge and then to the flow distribution system. This fluid gets heated as it flows through the heated elements and leaves through the top connection. The plate with slots that directs flow over the surfaces will be referred to as flow distributor. This system uses two different flow distributors – parallel and impinging flow distributors. The parallel flow distributor delivers a flow parallel to the heated surfaces. The impinging flow distributor delivers an impinging flow to the bottom heated surfaces, and hits the center of the bottom surface. The angle of impingement is 36° to the die surface. Figure 24 shows the depictions of the parallel and impinging flow distributors. The dimensions of these flow distributors are shown in drawings presented in Appendix-A. All fluid connections into the cartridge are provided by the quick-disconnect couplings from Colder© Products LC series.

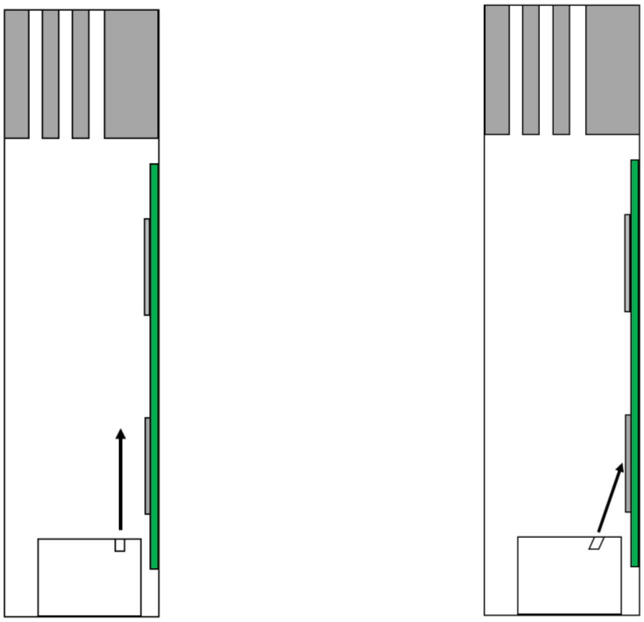

Figure 24: Flow in parallel flow distributor (left) and impinging flow distributor (right)

3.2 Fluid Supply and Control System

The fluid flow system in this setup has two isolated coolant loops -- chilled water and dielectric fluid loops. These flow loops along with measurement devices are shown in Figure 25, identified by the Reference Numbers (RN). The dielectric flow loop has the pumping, metering and heat removal components for the dielectric fluid. Subcooled dielectric fluid is pumped into the enclosure through a Ismatec® MCP-Z standard series pump (RN 2) integrated with a GJ series external gear pump head from Micropump®. The flow rate of the dielectric fluid is controlled through the pump. However, the dielectric flow rate values are measured through a Sponsler Lo-Flo series flow meter (RN 6) (P/N: MF90-MB-PH-A-4X-V) with a Sponsler 3 wire analog transmitter (P/N : SP711-3) which converts the frequency signals from the flow meter into a 0-5 V signal that is compatible with the Data Acquisition system. The dielectric fluid is heated up after flowing through the heated elements leaves the cartridge through the top, and rejects this sensible heat into the chilled water loop through a liquid-liquid heat exchanger (RN 3) from FlatPlate® P/N: FP3X8-14. The pool temperature is monitored through a 44007 thermistor from Omega Engineering (RN 21) placed in a relatively quiescent part of the pool. All the thermocouples used in this system K-type probes of the M12 series from Omega Engineering. These thermocouples are used in measuring the dielectric fluid temperature (RNs 13 &14), and chilled water temperature (RNs 15 through 20).

The chilled water loop provides system level heat removal and has the chilled water supply from a Fisher-Scientific™ Isotemp™ 1013D series chiller (RN 4). The flow rate from this chiller is back pressure driven and is controlled through threaded rod at the rear of the chiller. The chilled water loop is divided into three sub loops – Heat exchanger loop, chilled water header loop and Graham condenser loop. Flow meters from the FLR 1000 series from Omega Engineering are placed on each sub loop to monitor the flow rate (RNs 7, 8 and 9). The needle valves placed on each loop are used to independently control the chilled water flow rate (RNs 10, 11 and 12). In the pool boiling configuration of the system, the heat exchanger loop is disconnected from system and the chilled water header loop provides primary heat removal from the system. In flow boiling configuration, the heat exchanger loop provides primary cooling to the system and the chilled water header loop provides secondary cooling. The chiller output temperature can be controlled in 0.1°C increments, and this temperature will be referred to as

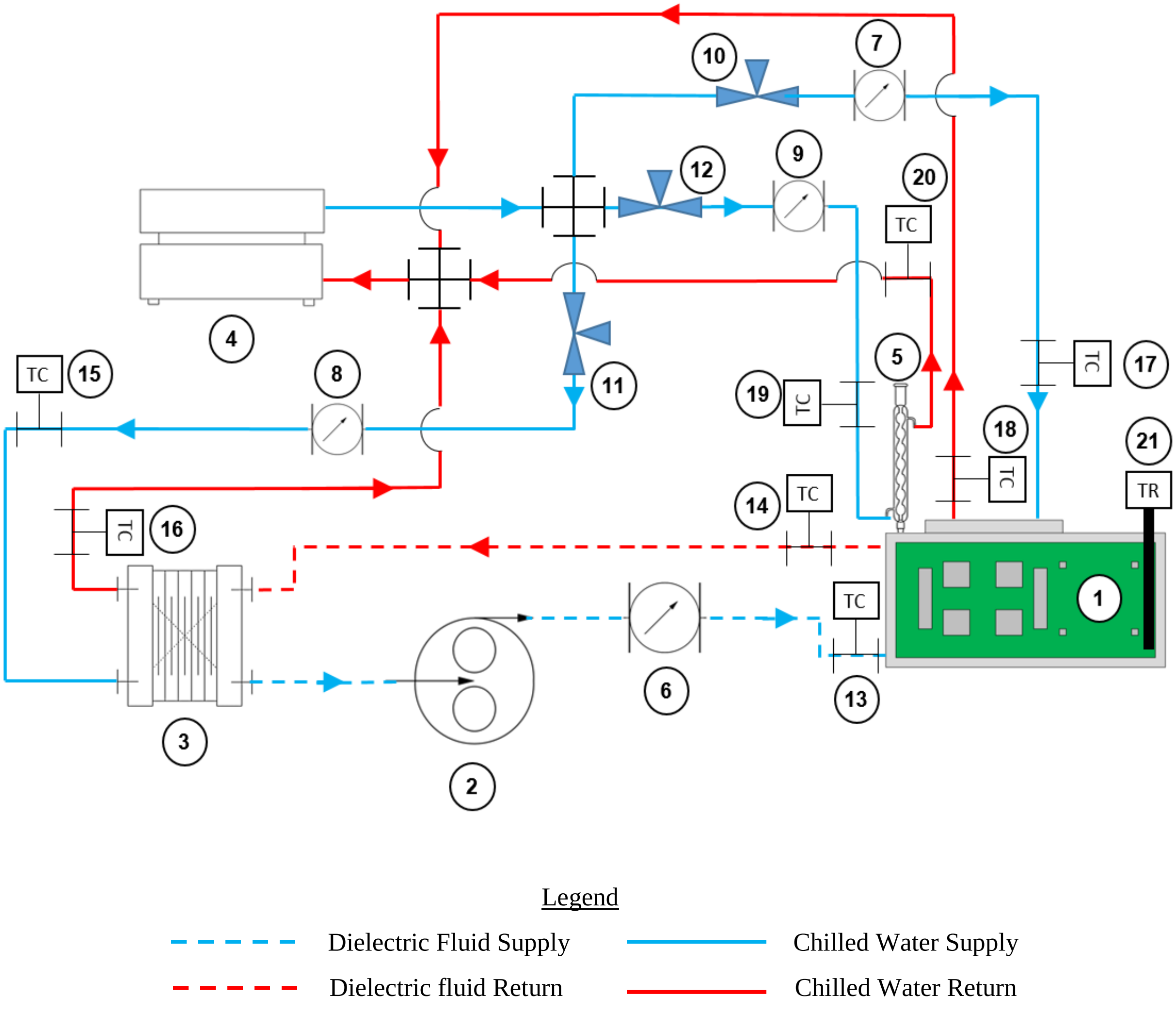

Reference Numbers

1 Enclosure Assembly
2 Dielectric Fluid Pump
3 Liquid-Liquid HX
4 Chiller
5 Graham Condenser
6 Dielectric Flow Meter
7 CW Flow Meter (CW Header)

8 CW Flow Meter (HX)
9 CW Flow Meter (GC)
10 CW Needle Valve (Header)
11 CW Needle Valve (HX)
12 CW Needle Valve (GC)
13 Thermocouple (DF Inlet)
14 Thermocouple (DF Outlet)

15 Thermocouple (HX Inlet)
16 Thermocouple (HX Outlet)
17 Thermocouple (CW Header Inlet)
18 Thermocouple (CW Header Outlet)
19 Thermocouple (GC Inlet)
20 Thermocouple (GC Outlet)
21 Thermistor (Pool)

Figure 25: Fluid supply and control system

facility water temperature throughout this study. The facility water temperatures used in this study are 7°C, 11°C and 15°C, which are typical for data center facilities that use chillers for heat rejection. For all the experiments in this study, the facility water flow rate was set at a constant value.

3.3 Surface Enhancements

The improvement in boiling heat transfer brought about by the addition of surface enhancements is an essential aspect to be investigated, as these enhancements provide higher heat transfer coefficients and reduced surface temperatures without the need for significant design changes to the cooling system. In addition to the bare silicon surface, thermal performance of the system with two surface enhancements – microporous (MP) and microfinned (MF) surfaces were also investigated in this study. Figure 26 shows these two surfaces along with the Scanning Electron Microscope (SEM) image of each surface. Both the surface enhancements are created by adding a layer of gold film to the exposed top surface of the bare silicon test cell and the back face of the microporous and microfinned heat sinks. The gold layers help in adhesion of the two surfaces with a metal foil from Indium Corporation©. The microfinned heat sink has a 1mm thick copper base and an array of 30 x 30 square fins that measure 400 μm on each side, 2 mm in height and spaced 400 μm apart. This heat sink was machined out of a solid copper block using Electrical Discharge Machining (EDM) process. The microporous heat sink also has a copper base and a top surface that is created by bonding silver coated copper spheres that are 10-50 μm in diameter. Further fabrication details of this structure are provided in Appendix-D.

For low heat flux values, both microporous and microfinned surfaces offer better thermal performance, as their heat transfer areas are higher compared to the bare silicon surface. The mechanisms that drive thermal performance improvement are different for the high heat fluxes in the fully developed boiling regime, which is important to electronics cooling applications. The interwoven structure of the microporous surface increases the number of cavities, which in turn increases the nucleation density and leads to higher two-phase heat transfer. Also, the surface tension of liquid travelling through these pores provides an added wicking force, which counteracts the shear force from the vapor travelling away from the surface. This increases the heat flux value required to cause vapor production that is needed to prevent effective rewetting of the surface, and therefore increases the highest heat dissipated by the cooling system. In the fully developed boiling regime, the microfinned surface has nucleation activity not only on the base of the heat sink, but also on the fin surfaces, including fin tips. This increase in nucleation density leads to higher heat transfer performance. At heat flux values near CHF, while the base of the microfinned heat sink has vapor agglomeration that blankets the surface and impedes heat transfer to the fluid, the fin regions that protrude beyond this vapor blanket can still support nucleation activity. This nucleation activity in the region beyond the vapor blanket enables heat from the surface to be rerouted to the fin regions, and this in turn increases the heat flux required to cause catastrophic failure.

3.4 High-Speed Imaging System

In order to understand the change in bubble characteristics of the different parameters used in this system, high-speed imaging was performed on the heated surfaces. A Phantom®

v310 high-speed camera from Vision Research was used in capturing the nucleation activity on the surfaces. The camera can operate between the frame rates of 200 frames per second (fps) to 120000 fps. Frame rate values of 1000 fps or 2000 fps were typically used in this study. Higher magnification imaging was needed due to the small length-scale of the bubbles, which was performed using the K2/Sc microscopic lens from the Infinity Photo-Optical Company. Depending on whether imaging was needed for an entire surface or for features within the surface, two different objectives were used.

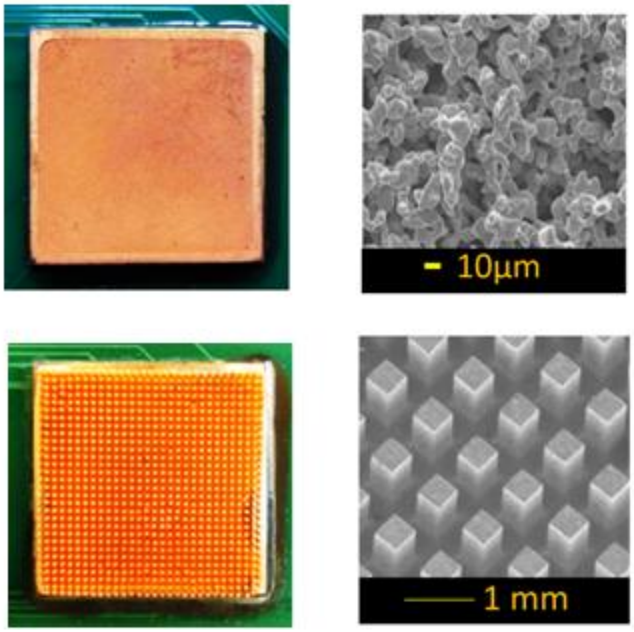

Figure 26: Microporous (top) and microfinned (bottom) enhancement surfaces

Chapter 4: Results and Discussion

The results obtained for the flow boiling configuration of this cooling module are discussed in this chapter. In flow boiling, the primary heat removal is through the dielectric fluid flow and the chilled water header provides secondary cooling. Before starting the experimental runs to measure the flow boiling performance, the fluid system was thoroughly degassed to reduce the concentration of the dissolved gases in the fluid that are detrimental to the condenser performance. Degassing also removes the gases entrapped in the surface cavities, the presence of which might initiate nucleation at a lower heat flux than the actual incipience heat flux. The system is degassed for the corresponding facility water temperature by bringing the system to vigorous boiling and venting the dissolved gases through the Graham condenser. This process might result in reduction of the fluid level in the cartridge, and a small amount of fluid is added periodically to keep the fluid line above the dielectric exit port of the cartridge. After degassing, the flow boiling investigations are performed by increasing the power dissipated by the surfaces and measuring the corresponding surfaces temperatures after the system has reached the set steady-state criterion. This heat addition is continued until a visually determined termination point is reached, after which power supply to the surfaces is reduced. This power reduction is continued and the corresponding surface temperatures are measured again. The data from these runs are used in constructing the increasing and decreasing flow boiling curves. This experiment set is performed for a second time, to assess and ensure the repeatability of the experiments. The following sections present the results and observations for the different parameters used in this study. The relevant fluid properties of Novec 649 dielectric fluid are provided in Table 2.

Table 2: Saturated fluid properties of Novec 649

Property	**Value**
Saturation Temperature (T_{sat})	49°C
Liquid Density (ρ_l)	1517 kg/m³
Vapor Density (ρ_v)	12.6 kg/m³
Surface Tension (σ)	9.24 mN/m
Latent heat of Vaporization (h_{lv})	87956 J/kg
Liquid Specific Heat (C_{pl})	1118 J/(kg·K)
Liquid Thermal Conductivity (k_l)	0.054 W/(m·K)
Dynamic Viscosity (μ_l)	4.4 x 10^{-4} Pa·sec

4.1 Parallel Flow Distribution System Results

The thermal performance results of the system with parallel flow distributor are discussed in this section. The following subsections present the effect of facility water temperature, dielectric flow rate and surface characteristics. The values of parameters used in this study are provided in Table 3.

Table 3: Parameters used in parallel flow distribution system studies

Parameter	**Value/ description**
Facility Water Temperature (°C)	7, 11 and 15
Novec 649 Flow Rate (mL/min)	360, 660, 960 and 1260
Surface Characteristics	Bare silicon, Microporous and Microfinned

4.1.1 Facility Water Temperature and Dielectric Flow Rate Effects

For the fluid system in this study, decreasing the facility water temperature increases the subcooling of the Novec 649 fluid. For a given heat flux value, increase in the level of subcooling, or the temperature difference between the system fluid temperature and its saturation temperature, results in smaller bubble departure diameters from the heater surface. Therefore, as subcooling is increased, higher heat fluxes will be required to increase the bubble diameter, and cause vapor agglomeration that leads to CHF. Increasing the dielectric fluid flow rate in a subcooled system like the current study improves the convective transport, and provides better quenching for the heated surfaces. This improved vapor removal leads to the requirement of higher heat flux values to cause dryout patches on the surface. Therefore, both increasing the flow rate and decreasing the facility water temperature must increase the CHF limit of the system. While the aforementioned parameters have the effect of lifting the fully boiling curve upward, observations have shown that the surface temperatures in the fully developed boiling regime is less sensitive to the changes in flow rate and subcooling, and all the curves merge into a single curve in this regime. This is shown in Figure 27.

For the bare silicon surface at a facility water temperature of 11°C, Figure 28 shows the effect of increasing the dielectric fluid flow rate. The heat flux values presented are calculated based on the foot print of all four surfaces, and each individual surface measures 25.4 mm x 25.4 mm (1” x 1”). The curves presented here are for decreasing runs, as the temperature overshoot during nucleation incipience creates difficulties in comparing increasing heat flux runs. From Figure 28, it can be observed that the increasing flow rate values improve the highest heat dissipated by the system, which is in line with the previous discussion. The increasing flow rates, however, have no significant effect on the surface temperatures throughout the flow boiling curve. Similar trends were also observed for the bare silicon surface at 7°C and 15°C facility water temperatures. The highest heat dissipation values presented in Figure 28 are not necessarily the CHF values, but the heat flux value at which heat addition was stopped in the experiment to prevent any permanent damage to the test surfaces. This point of heat addition termination was decided based on visual observation of the boiling activity using the Phantom v310 high-speed camera. Figure 29 presents the screen-captured high-speed image of the bare silicon surface at this termination point. From the figure, it can be seen that boiling activity is

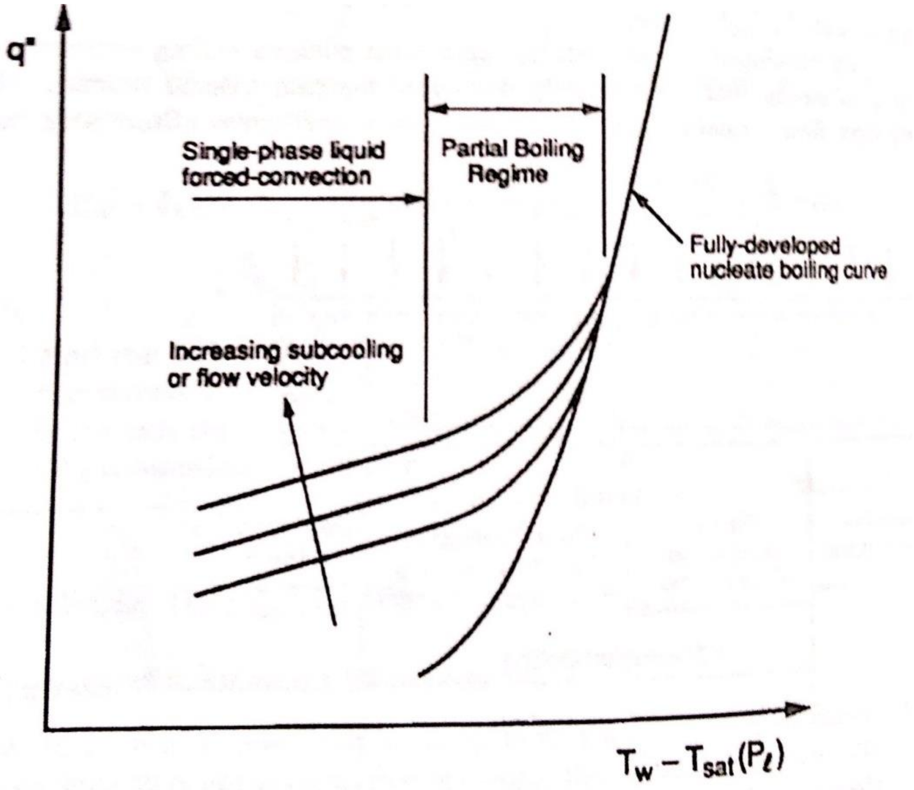

Figure 27: Effect of subcooling and flow rate on flow boiling curves [72]

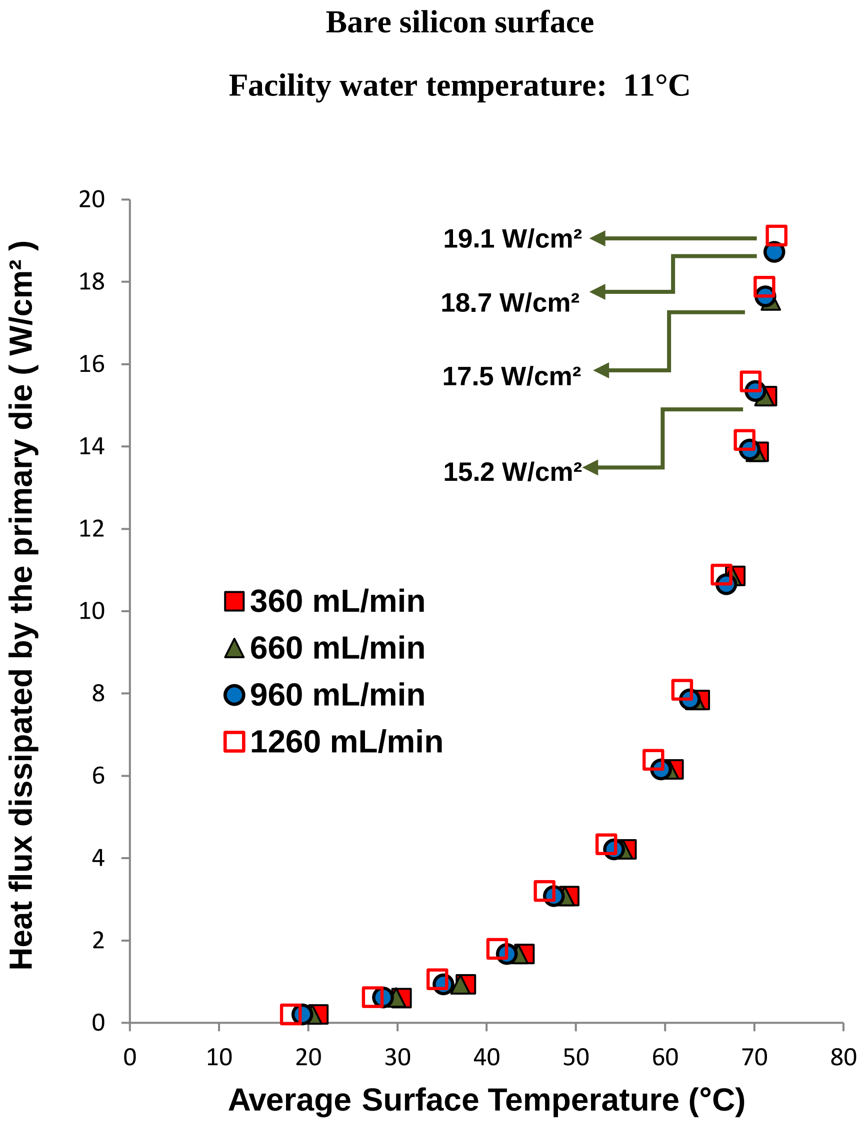

Figure 28: Effect of increasing flow rates on thermal performance of bare silicon surface with parallel flow distributor

vigorous, featuring large vapor masses forming all over the surface, indicating an impending CHF. Figure 30 presents the effect of decreasing the facility water temperature for the system with bare silicon surfaces at a flow rate of 660 mL/min. In addition to the increase in heat dissipation, the flow boiling curves show surface show reduced surface temperatures in the forced convection regime, and this trend continues into partial boiling regime but the temperature differences decrease along the way. The fully developed boiling regime is less sensitive to the change in facility water temperature. Similar trends were observed at other flow rate values tested in this study. In addition to the boiling literature, the study by Rainey et al. [56] for electronics cooling applications has also shown similar flow boiling trends with changes in flow rate and subcooling. This study used a flat copper test surface with dimensions comparable to the current study, and used FC-72 dielectric fluid which has comparable properties to Novec 649 used in current study.

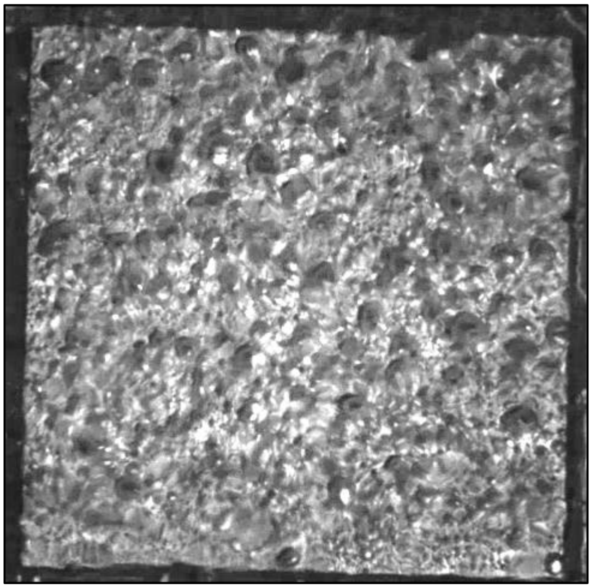

Figure 29: Boiling activity at heat-addition termination point for the bare silicon surface

Table 4 shows the summary of thermal performance of the bare silicon surface under different values of facility water temperature and flow rate used in this study. From Table 4, it can be seen that the increase in flow rate by 900 mL/min and decrease in facility water temperature by 8°C achieves up to 50% increase in heat dissipation. Achieving these operational parameters does not need additional equipment, as the facility water temperature of 7°C is within the typical range of chiller operation temperature for liquid cooling applications [73], and the

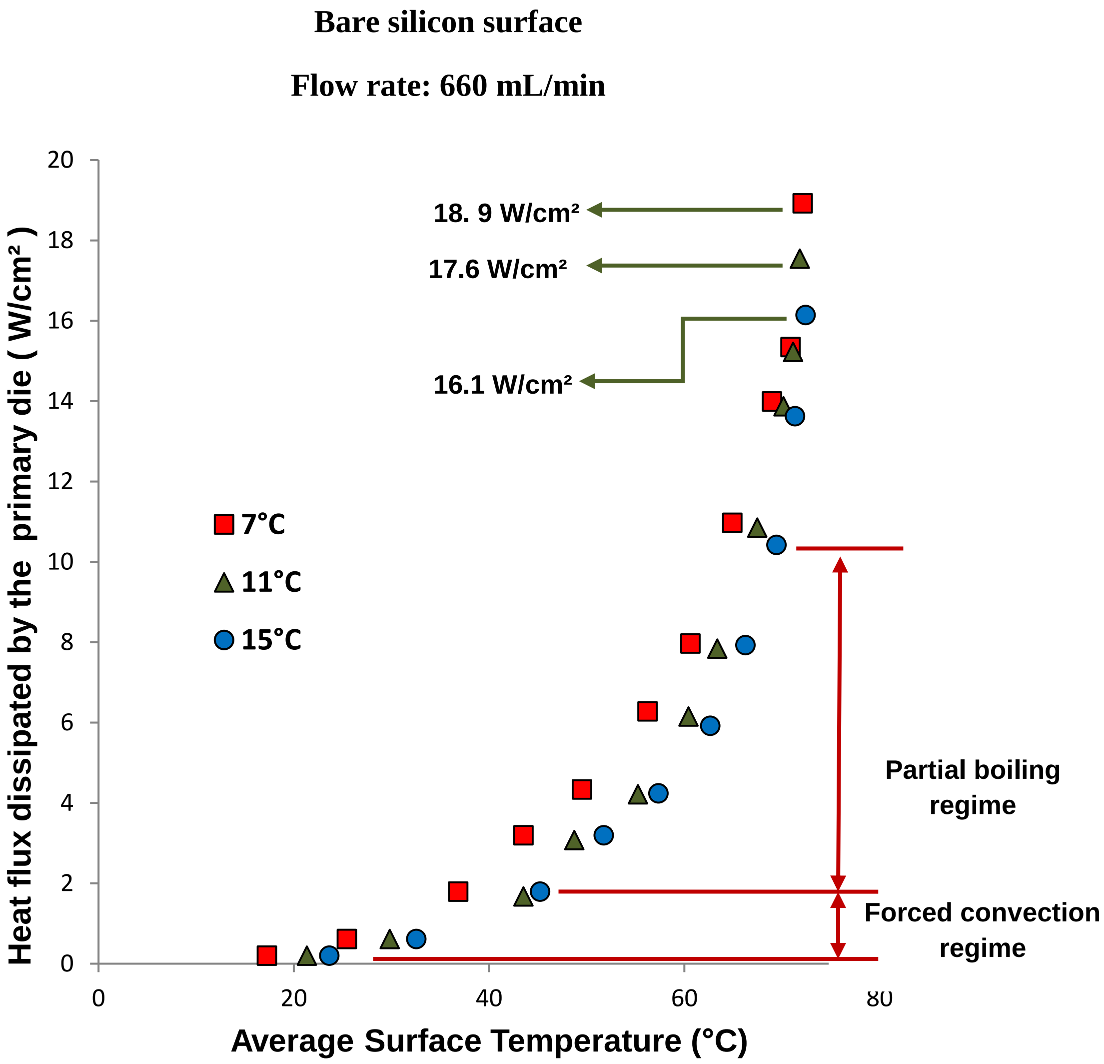

Figure 30: Effect of decreasing facility water temperatures on the boiling curves of bare silicon surface with parallel flow distributor

pumping power is not high due to the combination of gentle flow rates and low pressure drop across the system. The Rohsenow correlation shown in Equation 3 provides the relationship

$$\frac{q"}{\mu_l * h_{lv}}\left[\frac{\sigma}{g(\rho_l-\rho_v)}\right]^{\frac{1}{2}} = \left(\frac{1}{C_{sf}}\right)^{\frac{1}{r}} * {Pr_l}^{-\left(\frac{s}{r}\right)} * \left[\frac{C_{pl}[T_w-T_{sat}(P_l)]}{h_{lv}}\right]^{\frac{1}{r}} \tag{3}$$

between the wall heat flux and the surface temperature for the fully developed nucleate boiling heat transfer. Where the values for r and s in the equation are 0.33 and 1.7 respectively for a fluid like the dielectric fluid used in this study are. The other fluid properties are taken from Table 2 which are the saturated properties of the fluid. The value of C_{sf} is determined by the type of the fluid and the surface, and determination of this value could aid in prediction of nucleate boiling heat transfer to an accuracy of ±40%. With the values of heat flux, q" and average surface temperature, T_w determined from the experiments, other relevant properties of the fluid can be plugged into Equation 3 to determine the C_{sf} value. The C_{sf} values are listed in Table 4 for the bare silicon surface. This value is calculated by using the highest heat flux dissipated for a given facility water temperature and flow rate, along with the corresponding average surface temperature.

The combined effect of flow rate and facility water temperature on the nucleation characteristics of the bare silicon surface is shown in Figure 31. It can be seen that the single-phase heat transfer dominates the system with highest subcooling and flow rate. The nucleation density is higher for the system with lowest subcooling and flow rate, and this high nucleation density leads to vigorous boiling at a relatively lower heat flux than the system with high flow rate and subcooling.

Table 4: Thermal performance summary of bare silicon surfaces with parallel flow distributor

Facility Water Temperature (°C)	Flow Rate (mL/min)	Heat Flux (W/cm²)	Average Surface Temperature (°C)	C_{sf}
7	360	17.5	72.6	0.0046
	660	18.9	73.6	0.0047
	960	19.8	74.2	0.0047
	1260	20.5	74.1	0.0047
11	360	15.2	72.3	0.0048
	660	17.6	72.1	0.0045
	960	18.7	73.6	0.0047
	1260	19.1	73.9	0.0047
15	360	13.6	71.9	0.0049
	660	16.1	72.7	0.0048
	960	17.3	73.6	0.0048
	1260	17.7	74.2	0.0049

Figure 32 shows the effect of increasing flow rate for the system with microporous surfaces at 15°C facility water temperature. The trends are similar to that of the bare silicon surface, with increase in heat dissipation and no significant changes in the surface temperatures all throughout the flow boiling curve. Figure 33 shows the effect of decreasing the facility water temperature for the system at flow rate of 360 mL/min. These results are also comparable to that of the bare silicon surface, with reduced temperatures in the convection regime continually reducing up to the partial regime. Similar trends have been observed on microporous surfaces by Rainey et al. [56] in their flow boiling experiments.

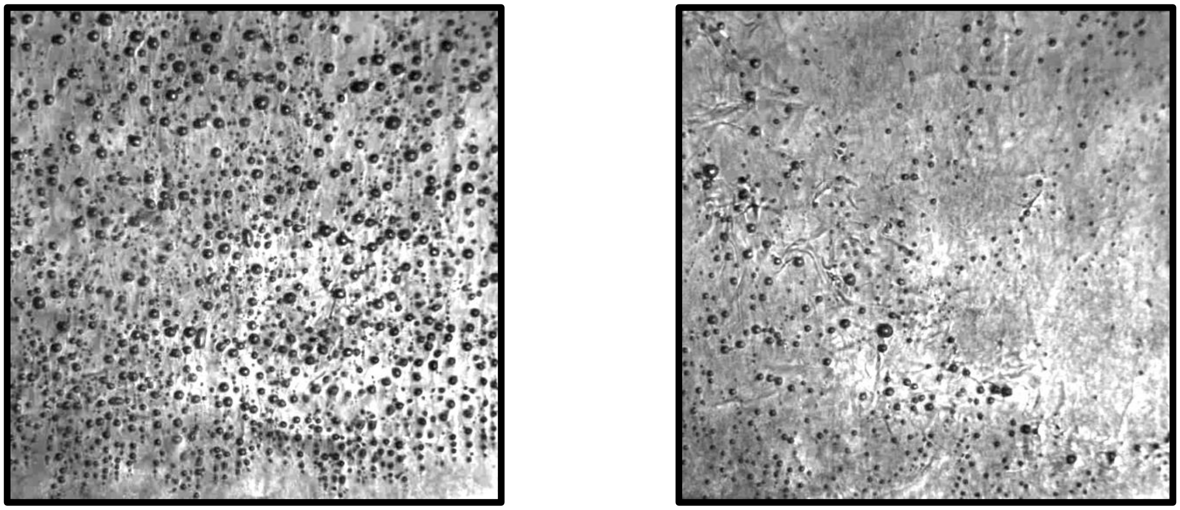

(a) 360 mL/min & 15°C **(b) 1260 mL/min & 7°C**

Figure 31: Nucleation characteristics of bare silicon surfaces at the lowest flow rate and highest facility water temperature (a) and vice-versa (b)

Table 5 shows the summary of thermal performance of the system with microporous surfaces at different flow rates and facility water temperatures. Experimental constraints due to performance issues in test surfaces limited the range of parameters tested. But the data from Table 5 alone is sufficient to show the significant impact of subcooling and flow rate on heat dissipated by the system. Figure 34 shows a screen-captured high-speed image of the vigorous boiling activity at which heat addition was stopped. The large vapor agglomeration on the surface is clearly discernible in this image

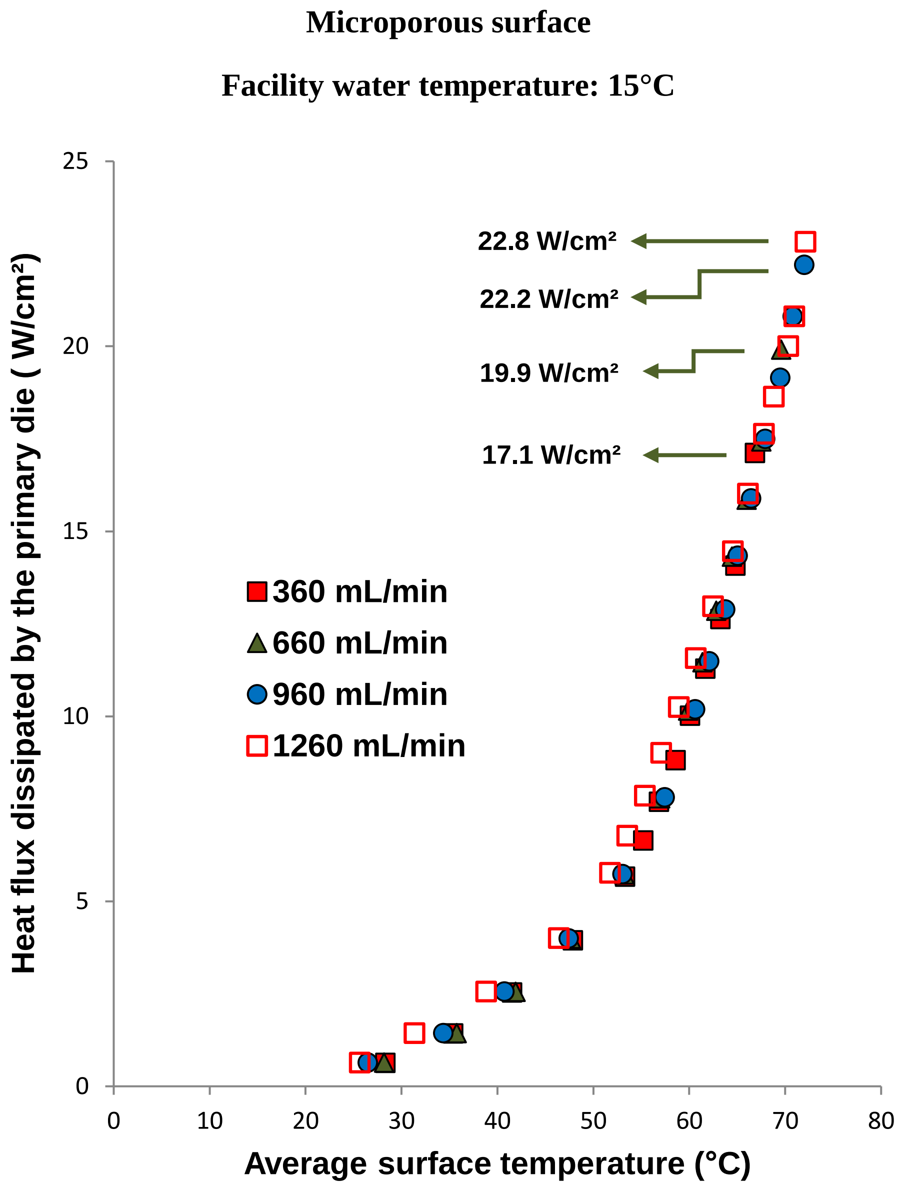

Figure 32: Effect of increasing flow rate on flow boiling curves of the microporous surface with parallel flow distributor

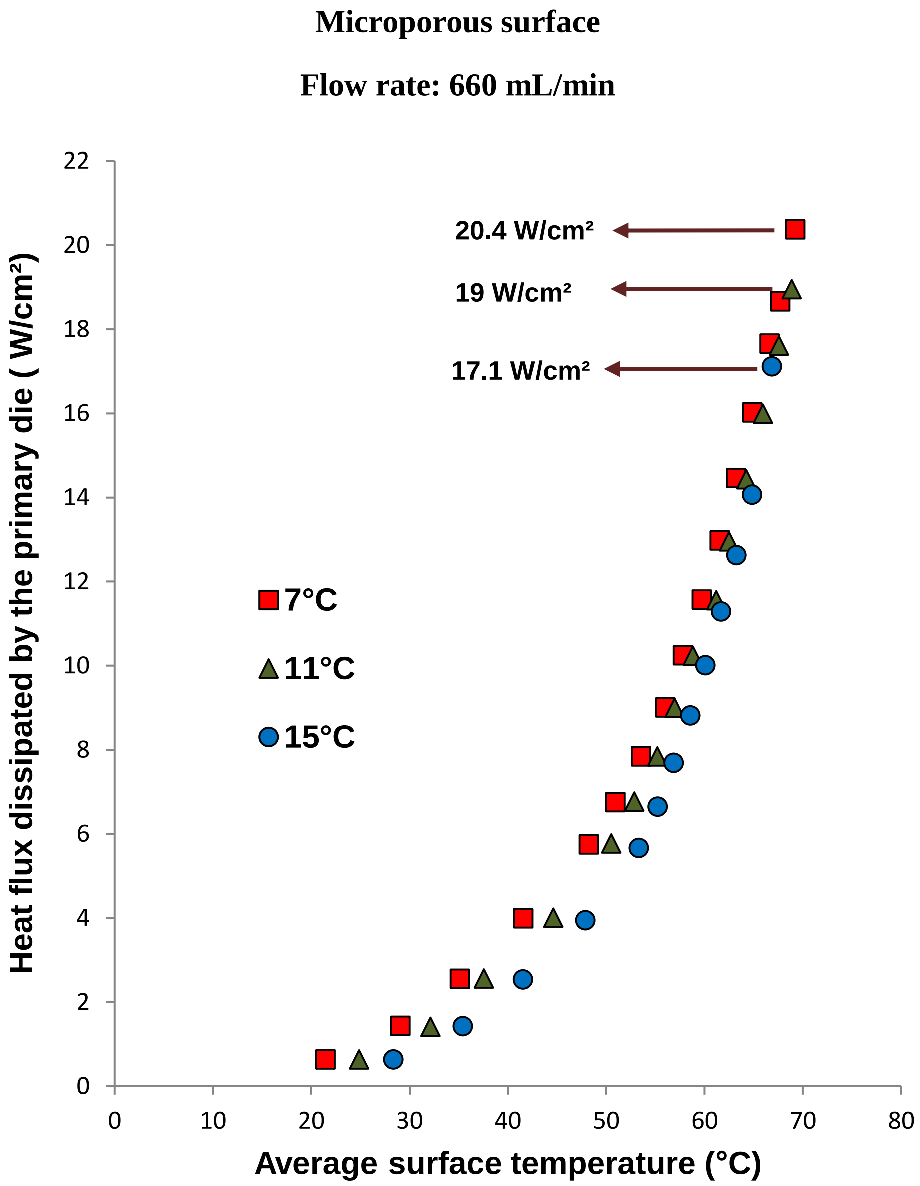

Figure 33: Effect of decreasing facility water temperature on the flow boiling performance of microporous surfaces with parallel flow distributor

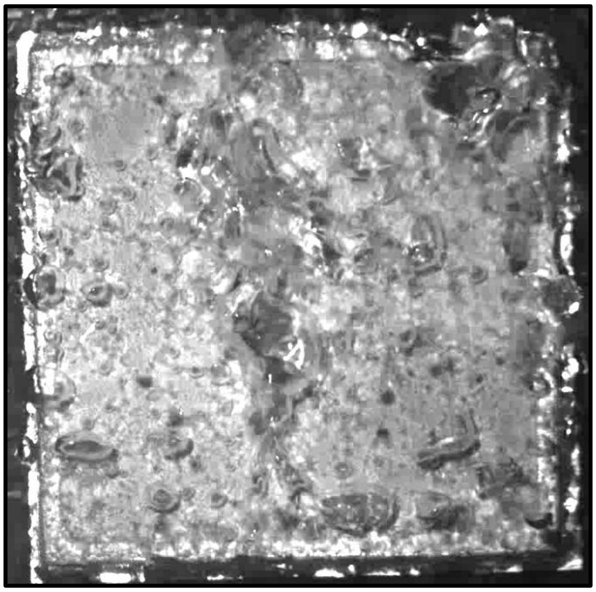

Figure 34: Screen-captured high-speed image shows the vigorous boiling activity at the heat-addition termination point for the microporous surface

Table 5: Thermal performance summary of microporous surface with parallel flow distribution system

Facility Water Temperature (°C)	Flow Rate (mL/min)	Heat Flux (W/cm^2)	Average Surface Temperature (°C)	C_{sf}
7	360	20.4	69.2	0.0038
11	360	19	68.9	0.0038
15	360	17.1	66.9	0.0035
	660	19.9	69.6	0.0039
	960	22.2	72	0.0041
	1260	22.8	72.1	0.0041

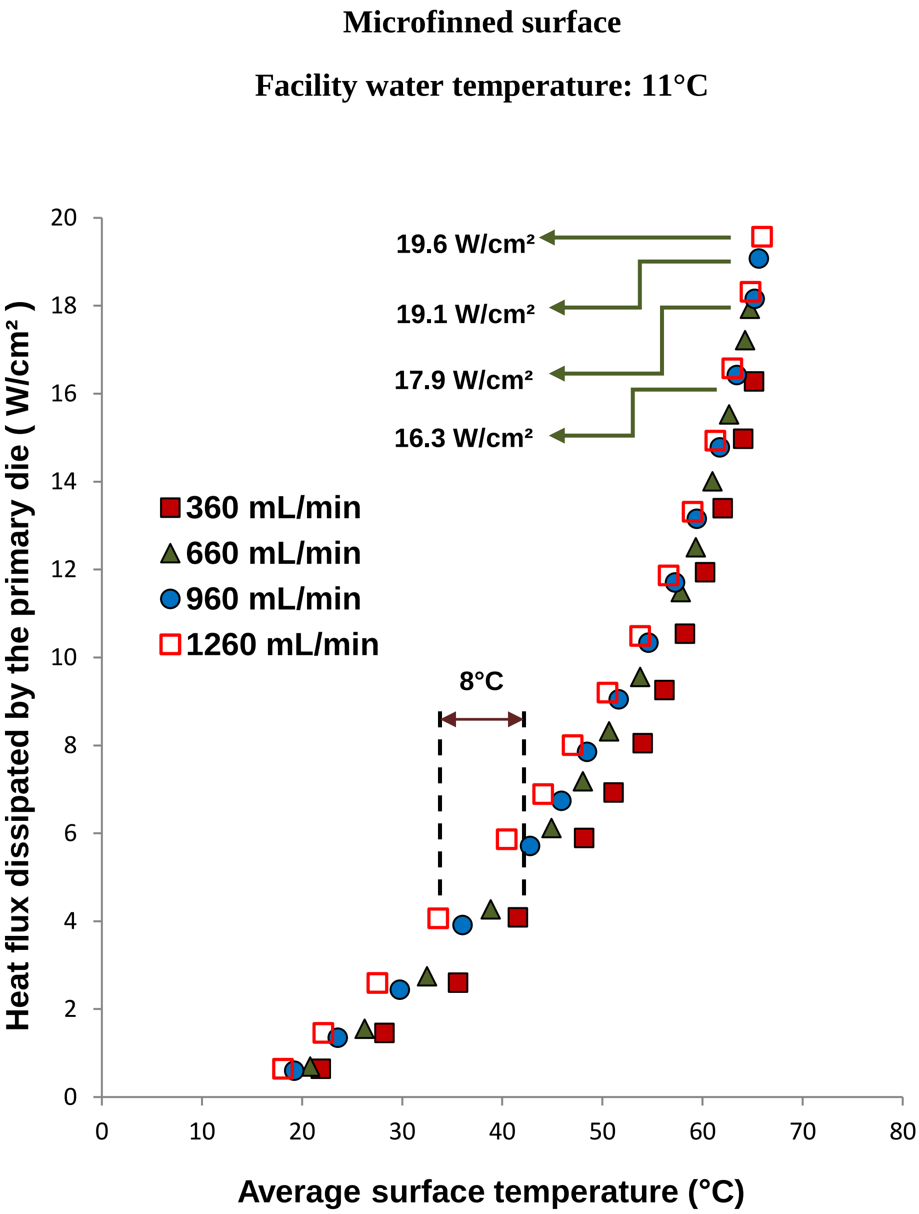

Figure 35: Effect of increasing flow rate on thermal performance of the microfinned surface with parallel flow distribution system

Figure 35 shows the effect of increasing flow rates for the system with microfinned surfaces at 11°C facility water temperature. Unlike the bare silicon and microporous surfaces, the boiling curves for microfinned surface show a different response to change in flow rate. In addition to increase in heat dissipation, the increasing flow rates also reduce the surface temperatures in the forced convection and partial boiling regimes. The fully developed boiling regime, however, is less sensitive changes in flow rate. Similar trends are observed at the other two facility water temperature settings. This different response can be attributed to the increased heat transfer area with the extended fin surfaces, which provide higher single-phase heat transfer in the forced convection regime with increase in flow rate. This enhanced single-phase contribution continues into the partial boiling regime, and becomes progressively less dominant as the contribution from boiling heat transfer increases. Figure 36 shows the effect of decreasing the facility water temperature for the system at 660 mL/min flow rate. The trends here are comparable to bare silicon and microporous surfaces, with increase in heat transfer and reduction of surface temperatures in the convection and partial boiling regimes. In flow boiling experiments for silicon surfaces with micro pin-fin using FC-72 as working fluid, Yuan et al. [45] found similar trends in heat dissipation and surface temperatures for the parameter ranges of 15-35 K level of subcooling and 0.5-2 m/s flow velocity.

Table 6 shows the thermal performance of the microfinned surface for different values of flow rate and facility water temperatures. The change in parameters provides up to 40% improvement in heat dissipated by the system. For the microfinned surface, all the heat flux values discussed in this study are calculated based on the base area, not the total surface area.

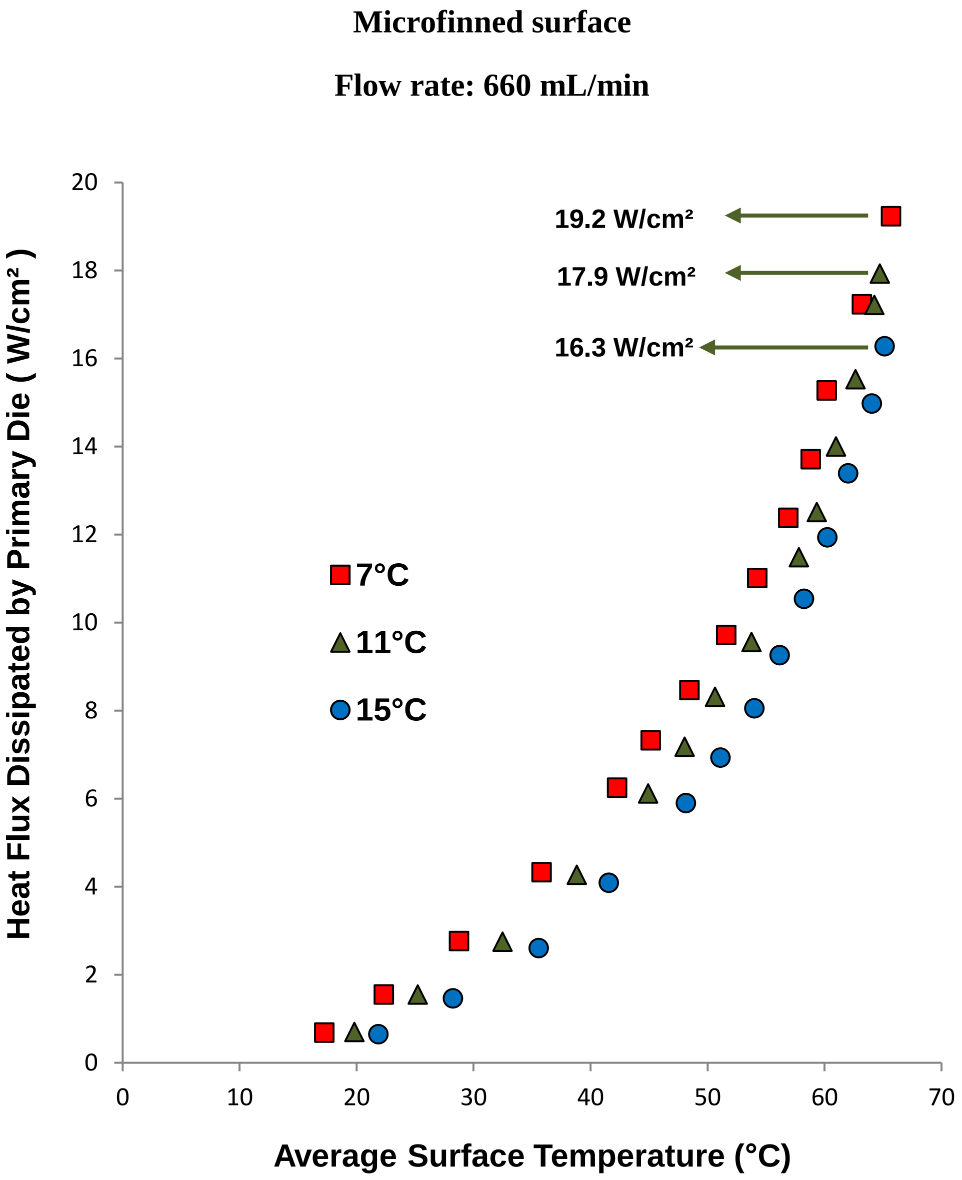

Figure 36: Effect of decrease in facility water temperature on the thermal performance of the microfinned surface with parallel flow distributor

4.1.2 Surface Enhancement Effects

This section compares the effect of surface characteristics on the thermal performance of the cooling model. Table 7 provides the highest heat dissipation values recorded in this study for the bare silicon, microporous and microfinned surfaces. As the problems with the microporous surface did not allow for the measurement at highest flow rate and subcooling, the highest value recorded among the values tested is provided. From Table 7, it can be observed that while the microfinned surface provides heat flux enhancement over the bare silicon surface for some

Table 6: Thermal performance summary for the microfinned surface with parallel flow distribution system

Facility Water Temperature (°C)	Flow Rate (mL/min)	Heat Flux (W/cm²)	Average Surface Temperature (°C)	C_{sf}
7	360	17.8	65.3	0.0032
	660	19.2	65.7	0.0032
	960	20.1	66.2	0.0032
	1260	20.8	66.6	0.0032
11	360	16.1	65.1	0.0032
	660	17.9	64.7	0.0030
	960	19.1	65.6	0.0032
	1260	19.6	66.1	0.0032
15	360	14.9	65.1	0.0033
	660	16.3	65.3	0.0033
	960	17.4	66.2	0.0034
	1260	18.3	65.9	0.0033

combinations of flow rate and facility water temperature, the highest heat flux recorded in this study for the microfinned surface is not substantially more than the highest heat flux of the bare silicon surface. It must be noted that the thermal performance comparisons and resulting conclusions presented throughout study are based on the highest heat dissipation values obtained with the author's visual assessment of the boiling activity, and a comparison of actual CHF values might lead to different conclusions. At the highest flow rates, while the bare silicon surfaces had a fairly uniform boiling activity across the four surfaces, the microfinned surface had a relatively non-uniform boiling activity between the top and bottom row of heater surfaces. At the highest heat flux value reported, the top row of heaters in the microfinned surface had a relatively higher boiling activity compared to the bottom heaters. To maintain uniform heat dissipation across all four surfaces, the heat addition had to be stopped after the top surfaces experienced vigorous boiling activity. Therefore, the bottom surfaces could reach higher heat flux values than heat flux values reported in Table 7. In terms of heat dissipation, the microporous surface outperforms both bare silicon and microfinned surface with heat flux values of up to 22.8 W/cm², even with 15°C facility water temperature and a flow rate of 1260 mL/min. This heat flux value corresponds to a heat dissipation of 588 W, or 147 W per chip. At this level, the volumetric heat dissipation of this system is 0.344 W/cm³. This dissipation is about 6.7 times higher than the volumetric dissipation of the air-cooled HP Proliant Gen8 server model [74]. For similar heat dissipation requirements, replacing air cooling with the model from current study will achieve dramatic reduction in data center size.

Table 7: Highest heat flux recorded in this study for different surfaces with parallel flow distribution system

Surface Type	Facility Water Temperature (°C)	Flow Rate (mL/min)	Highest Heat Flux Dissipated (W/cm²)
Bare Silicon	7	1260	20.5
Microfinned	7	1260	20.8
Microporous	15	1260	22.8

In terms of surface temperature, both microporous and microfinned surfaces perform better than the bare silicon surface. The highest surface temperature reported in this section for bare silicon surface is around 74°C, which is still significantly lower than the allowable junction temperatures of 85°C to 105°C. Figure 37 compares all three surfaces at a fixed facility water temperature and dielectric flow rate. It can be observed from the figure that the microporous and microfinned surfaces operate at 6°C and 7°C temperatures lower than the bare silicon surface. This is a substantial decrease, when the available temperature budget of the electronic devices is considered. With the failure rate of the processor doubling for every 10°C increase in surface temperature [75], the use of surface enhancements in immersion cooling stands essential to the reliability of the electronic devices.

To understand the enhancements brought about by the microfinned surfaces, high-speed imaging at 2000 fps was performed at a higher magnification to capture the bubble characteristics and the bubble-fin interaction. Figure 38 (a) - (d) screen-captured high-speed images for the microfinned surface at a flow rate of 360 mL/min and facility water temperature of 15°C. It can be observed from the images that the bubble nucleation is not just limited to the spaces between the fins, but also the periphery of the fins and also the tip of the fins. The surface was characterized by a wide range of bubble sizes, even at low heat fluxes. As a vapor slug generated from the lower surface enters the gap between the fins, it is squeezed and distorted by the fins. This squeezing action results in the vapor slug sweeping the small bubbles that are formed on the fin surfaces. The detachment of vapor bubbles from the surface causes the liquid to flow and replace the vapor, which again initiates the nucleation activity. Therefore, the sweeping action provides a bubble detachment mechanism to improve heat transfer. It must be noted that this entire process happens only when the characteristic size of the vapor slug is larger than inter-fin spacing. Along the depth of the fins, this squeezing activity happens at multiple planes. Further exploration of the fin spacing and geometry that optimizes this effect could be used to improve the heat transfer of surfaces that are located upstream to the other heated surfaces.

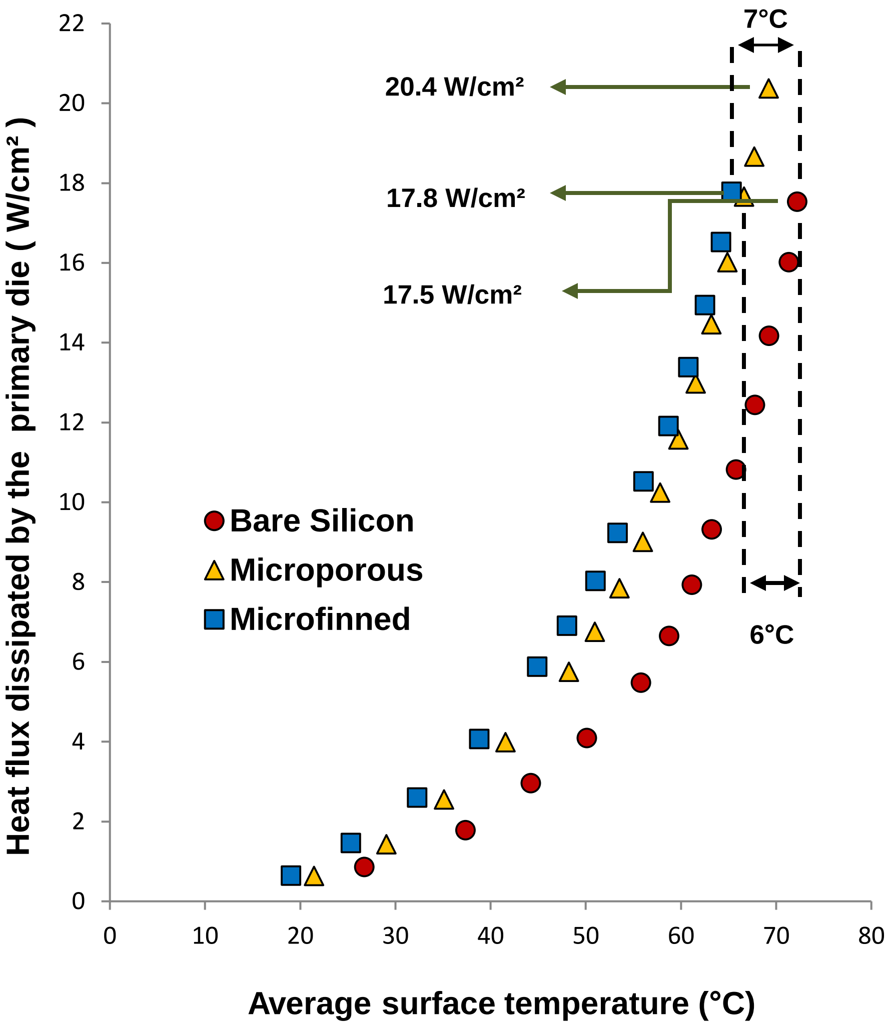

Flow rate: 360 mL/min

Facility water temperature: 7°C

Figure 37: Comparison of thermal performance of three surfaces at a fixed facility water temperature and flow rate

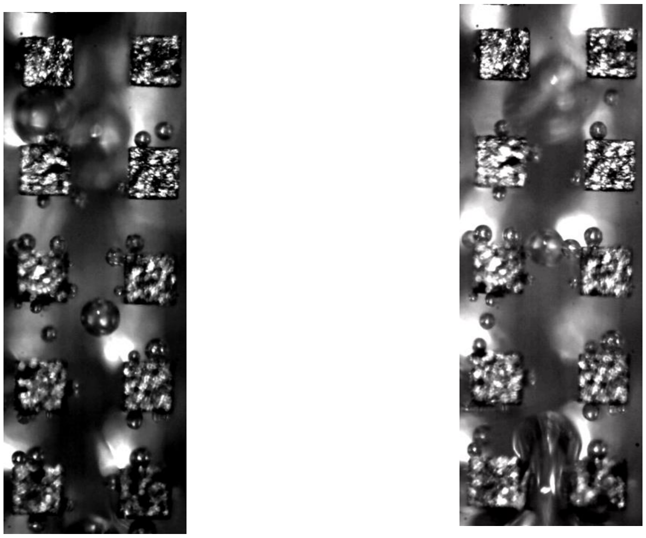

(a) Capture time: t + 0 ms **(b) Capture time: t + 8 ms**

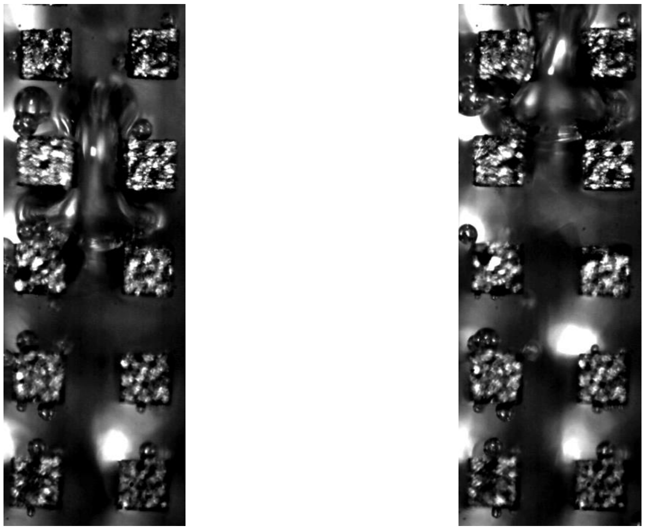

(c) Capture time: t + 34 ms **(d) Capture time: t + 43 ms**

Figure 38: Screen-captured high-speed images of microfinned surface showing the movement of vapor slug through the inter-fin spacing

4.2 Impinging Flow Distribution System Results

The results presented in this section are for the system implemented with impinging flow distribution system. Table 8 provides the parameters used in these studies.

Table 8: Parameters used in impinging flow distribution system studies

Parameter	Value/ description
Facility Water Temperature (°C)	7 and 15
Novec 649 Flow Rate (mL/min)	360, 1260 and 1650
Surface Characteristics	Bare silicon and Microfinned

4.2.1 Dielectric Flow Rate and Facility Water Temperature Effects

For the system with bare silicon surface at a facility water temperature of 7°C, the effect of increasing the flow rate from 360 mL/min to 1260 mL/min is presented in Figure 39. In the forced convection regime, the surface temperatures of the system with 1260 mL/min flow rate are lower than the system with 360 mL/min flow rate. This can be attributed to the effectiveness of the impinging flow distributor in disrupting the boundary layer, which impacts the bottom row of heaters, and increased mixing of the fluid in the pool that impacts the top row of heaters. However, for some of the heat flux values in the partial boiling regime, the two curves start merging into a single curve. This is due to the reason that the surfaces at 360 mL/min flow rate start nucleating at lower heat fluxes than the surfaces at 1260 mL/min, and since nucleate boiling has higher heat transfer rates than forced convection, the surfaces have relatively smaller increase in surface temperatures. As the boiling contribution in the system with 1260 mL/min flow rate increases, the surface temperature again becomes lower than the low flow rate system. Finally, the fully developed boiling curves for both flow rates approach into a single curve,

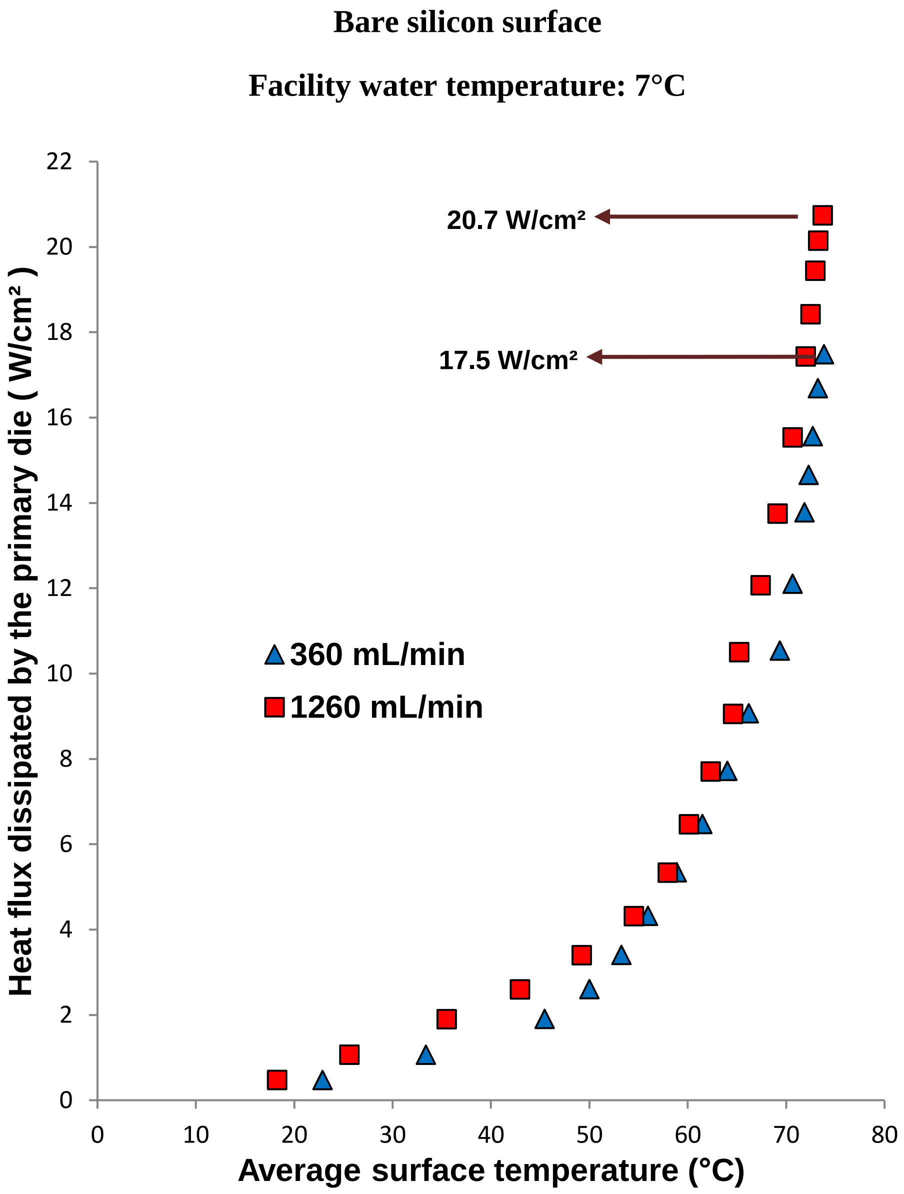

Figure 39: Effect of increasing the flow rate on thermal performance of bare silicon surfaces with impinging flow distributor

showing that this regime is less sensitive to changes in flow rate. Figure 40 shows the effect of decreasing the facility water temperature of the system from 15°C to 7°C for the system with

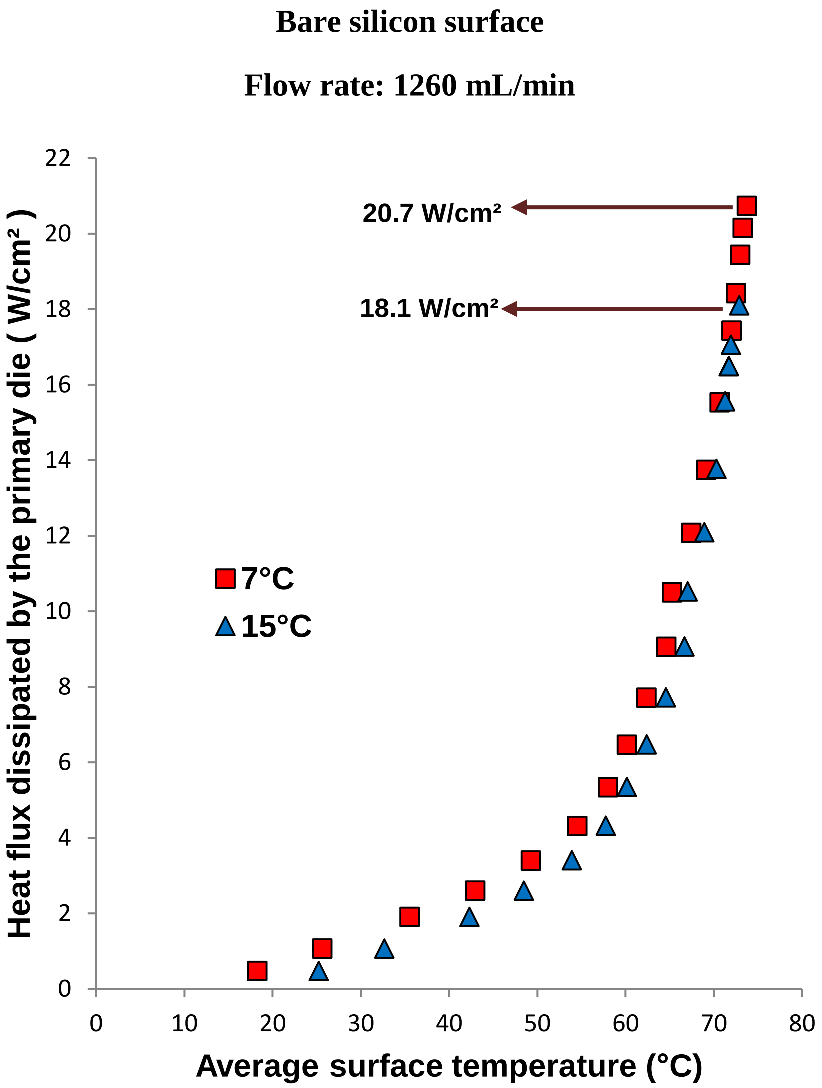

Figure 40: Effect of decreasing the facility water temperature on the thermal performance of bare silicon surface with impinging flow distributor

bare silicon surfaces at a flow rate of 1260 mL/min. The surface temperatures in the convection regime are lower for the 7°C system, and this difference reduces through the partial boiling regime and the curves collapse into a single curve in the fully developed boiling regime. The system at 360 mL/min shows a similar trend. Table 9 shows the summary of thermal performance for the bare silicon surfaces with the impinging flow distributor. The improvement in heat dissipation with changes in flow rate and facility water temperature is approximately 47%.

Table 9: Thermal performance summary of the bare silicon surface with impinging flow distribution system

Facility water temperature (°C)	Flow rate (mL/min)	Highest heat flux (W/cm^2)	Average surface temperature (°C)	C_{sf}
7	360	17.5	73.9	0.0049
	1260	20.7	73.7	0.0046
15	360	13.9	72.2	0.0049
	1260	18.1	72.8	0.0046

Figure 41 shows the effect of flow rate on the flow boiling curves of the system with microfinned surfaces at a facility water temperature of 7°C. The change in flow rate from 360 mL/min to 1260 mL/min has a substantial impact of the surface temperatures in the forced convection and partial boiling regimes, with up to a 10.5°C reduction. The increased heat transfer area of the microfinned surface, along with the high convective transport of the impinging flow distributors can be attributed to this enhanced response. The fully developed boiling curves, however, approach into a single curve. The system at the facility water temperature of 15°C also has a similar behavior. While the impinging flow distributor creates a temperature reduction for all four surfaces, the benefits at higher flow rates, however, are heavily toward the bottom row of heaters. This is because of the fact that the impingement effects are only experienced by the heaters proximal to the flow inlet. The top rows of heaters receive

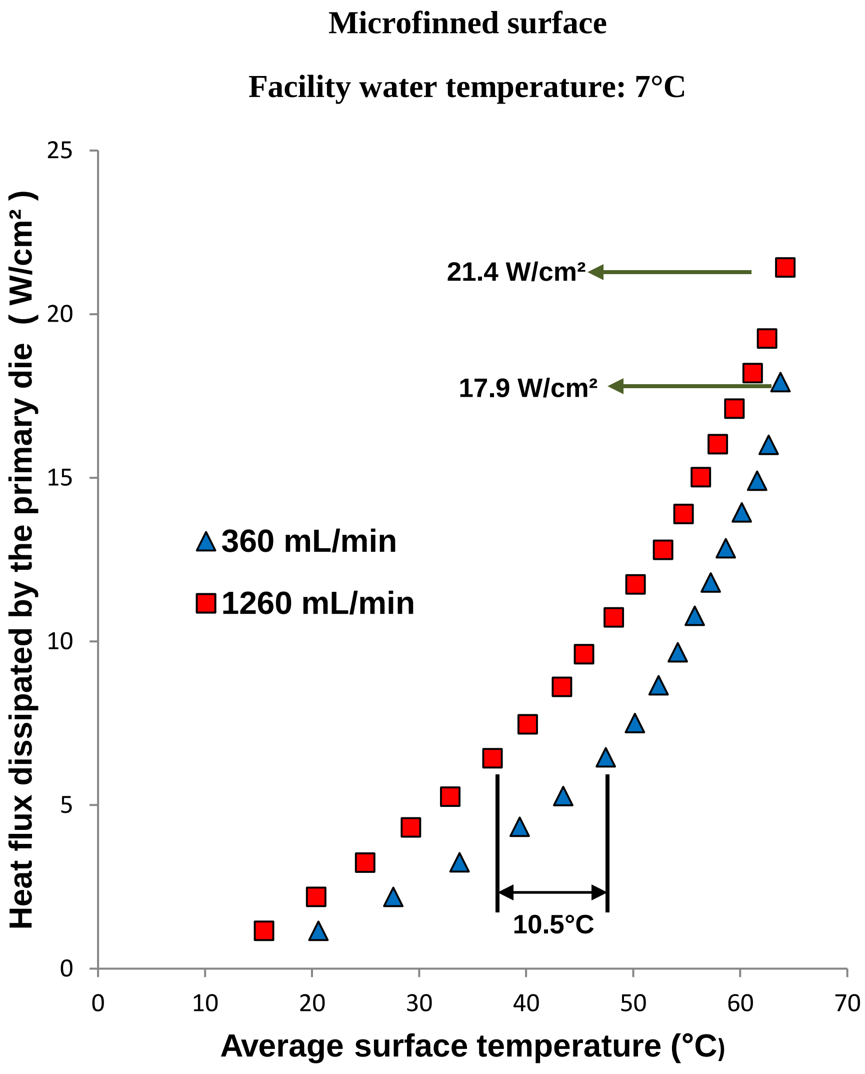

Figure 41: Effect of flow rate on thermal performance of microfinned surface with impinging flow distributor

roughly a parallel flow over the surfaces. If the system considered in current study is used in applications where there are high-power and low-power dies, the high-power elements with microfinned enhancements will be benefitted when placed proximal to impingement system. Figure 42 shows the effect of decreasing the facility water temperature in a system with 1260 mL/min flow rate. Temperature differences of up to 6.5°C between the 15°C and 7°C curves can be observed from the figure. The differences continue to reduce in the partial boiling regime and diminish in the fully developed regime. Table 10 shows the thermal performance of the system under different values of facility water temperature and flow rate. Up to 34% improvement in heat dissipation has been obtained by increasing subcooling and flow rate.

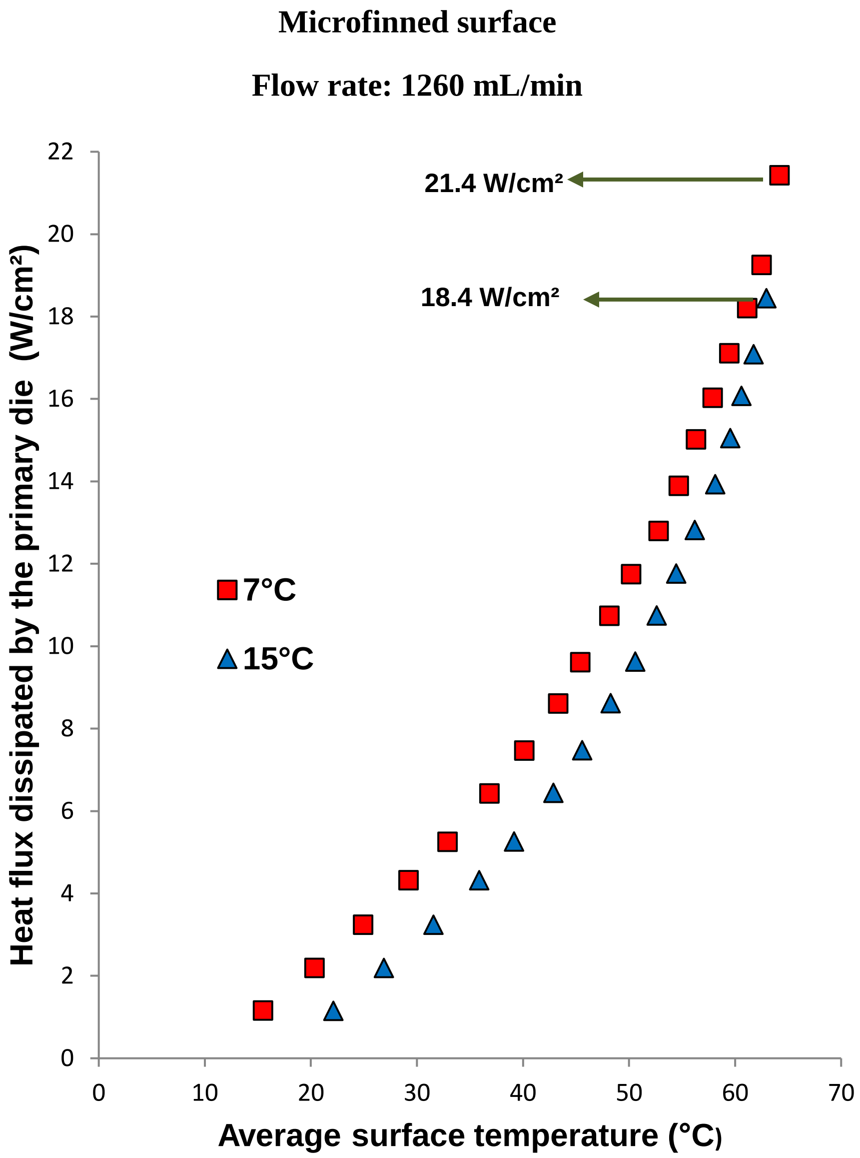

Figure 42: Effect of decrease in facility water temperature on thermal performance of microfinned surface with impinging flow distributor

Table 10: Thermal performance summary of the microfinned surface with impingement flow distribution system

Facility water temperature (°C)	Flow rate (mL/min)	Highest heat flux (W/cm²)	Average surface temperature (°C)	C_{sf}
7	360	17.9	63.8	0.0029
	1260	21.4	64.2	0.0028
15	360	15.5	62.2	0.0027
	1260	18.4	63	0.0027

4.2.2 Impact of Surface Enhancement

Table 11 provides the highest heat dissipation recorded in this study for the system for the bare silicon and microfinned surfaces with the impinging flow distributor implemented. As with the case of parallel flow distributor, while the microfinned surfaces showed heat dissipation improvement over the bare silicon surface at some flow rate and facility water temperature combinations, the highest recorded heat flux in this study for microfinned surface is not significantly more than the highest heat flux for the bare silicon surface. For high flow rates, the

Table 11: Highest recorded heat flux for bare silicon and microfinned surfaces with impinging flow distributor at 1260 mL/min flow rate and 7°C facility water temperature

Surface type	Heat flux (W/cm²)
Bare silicon	20.7
Microfinned	21.4

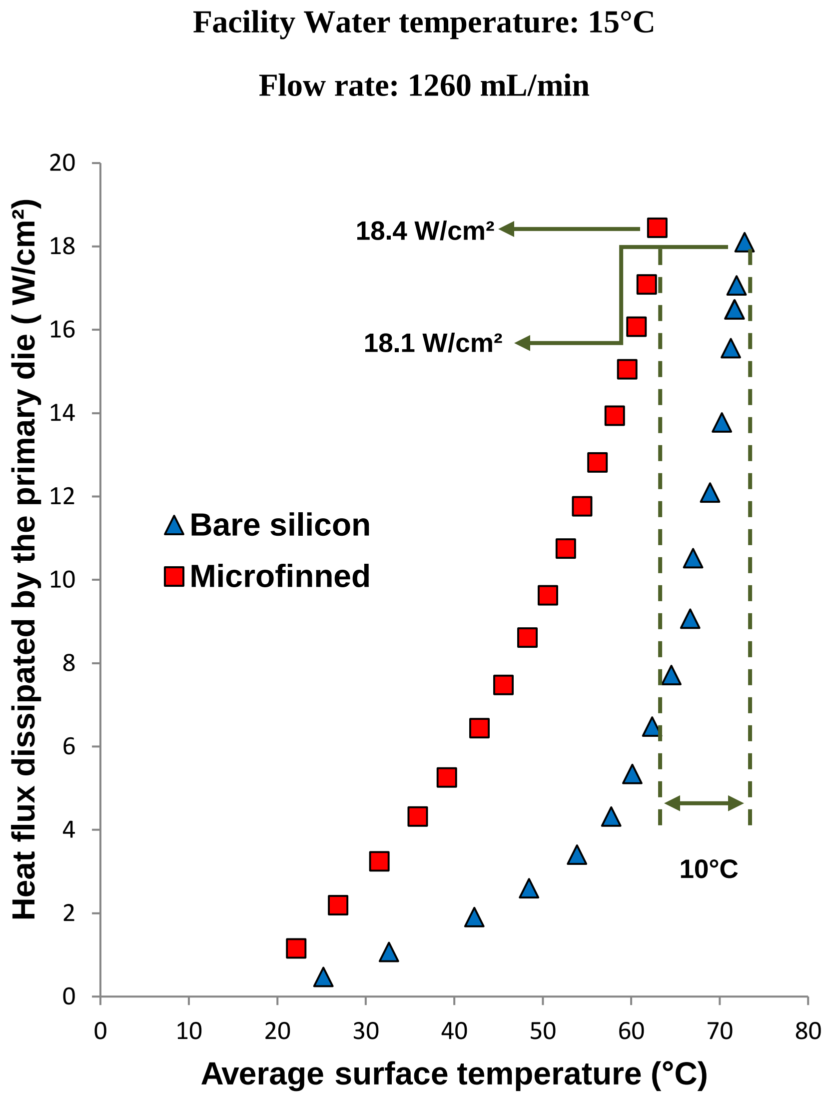

Figure 43: Thermal performance comparison for bare silicon and microfinned surfaces for impingement flow distribution system

stark difference in the boiling activity between the top row and bottom row of heaters meant that the system was constrained by the top heater surfaces receiving roughly a parallel flow, which was the reason for the lack of performance improvement. Figure 43 shows the thermal performance of the system with bare silicon and microfinned surfaces at a fixed facility water temperature and flow rate. It can be observed that for similar heat flux values, the microfinned surface operates at substantially lower temperatures than the bare silicon surface. These results once again underscore the impact of surface enhancements on improving the reliability of the electronic systems used in immersion cooling applications.

To quantify the highest performance of the impinging system, the system was set to the highest flow rate that could be consistently provided by the pump – 1650 mL/min, and the facility water temperature was set at 7°C. Only the lower pair of heaters was powered in these experiments. Both bare silicon and microfinned surfaces were tested in this study and the thermal performance of these surfaces are provided in Table 12. The highest heat flux recorded in these experiments is 28.6 W/cm², for the microfinned surfaces. This heat flux value represents a total heat dissipation of approximately 370 W or 185 W per die. This value is well above most of the high power chips in the market today. The surface temperature at this point is only around 62°C, which is well below even the 85°C operating temperature for electronics. Even at this limit, the system did not have vapor agglomeration all over the surface, but vigorous boiling at the top right section of the die as shown in Figure 44. This local effect is due to the reason that the current system employs only one slot that directs the fluid toward center of the die, and the boundary layer thickness is higher towards the top of the die. Designs that incorporate more fluid impingement points on the die may solve this problem, and further increase the heat flux limit of the microfinned surfaces. While the microfinned surfaces have the best performance, the bare silicon surfaces also show a substantial increase in heat dissipation value with around 320 W, or 160 W per chip. The higher performance of the microfinned surface in impingement systems compared to bare surface has also been recorded by Rau and Garimella [63], in a study that used HFE-7100 as working fluid.

Table 12: Highest thermal performance recorded for the bare silicon and microfinned surfaces with impinging flow distributor with power only to bottom heated surfaces

Surface characteristics	Highest heat flux dissipated (W/cm^2)	Average surface temperature (°C)
Bare silicon	24.8	73
Microfinned	28.6	61.9

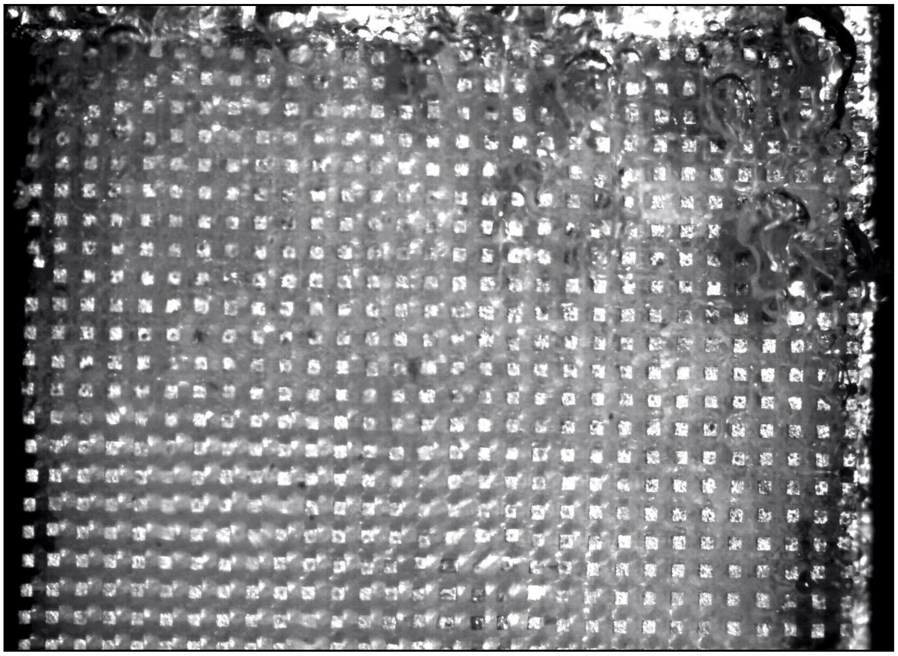

Figure 44: Screen-captured high-speed image showing vigorous boiling activity only at the right corner of the microfinned surface

4.3 Flow Distributor Effects

This section compares the impact of flow distribution system on the thermal performance of the cooling system. Table 13 provides the heat dissipation recorded for the bare silicon and microfinned surfaces under parallel and impingement flow distribution systems along with the corresponding average surface temperatures. It can be observed from Table 13 that for both surface characteristics, replacing the parallel flow distribution system with impinging system does not offer any improvement in thermal performance. As discussed in a preceding section, the reason for this lack of performance improvement can be attributed to the fact that the impingement effects are highly local to the bottom surfaces, and the top surfaces still receive roughly a parallel flow. To maintain uniform heat dissipation in the experiments with four dies powered, heat addition had to be stopped once the top dies achieved vigorous boiling. The mixing of the fluid in the pool due to the introduction of the impinging flow distribution does not seem to significantly affect the flow field of the top heater surfaces. As it was demonstrated

Table 13: Highest heat flux comparison of parallel and impinging flow distributors

Surface type	Flow distributor	Heat flux (W/cm²)	Average surface temperature (°C)
Bare silicon	Parallel	20.4	73.7
	Impinging	20.7	73.8
Microfinned	Parallel	20.8	64.3
	Impinging	21.4	64.2

Bare silicon surface

Facility water temperature: 7°C

Flow rate: 360 mL/min

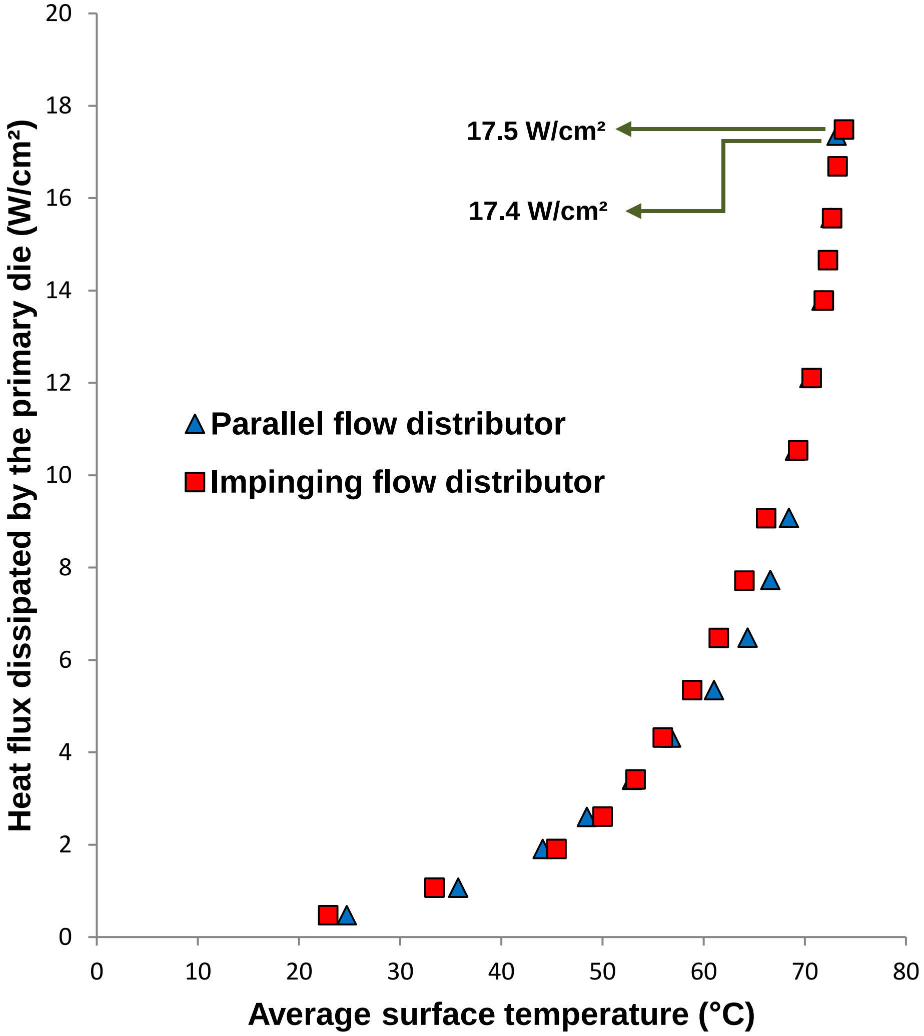

Figure 45: Comparison of thermal performance of parallel and impinging flow distributors for the bare silicon surface for 360 mL/min flow rate

toward the end of the previous section, the impingement system can offer high heat dissipation capability for the surfaces in this system. Implementation of flow distributors that provide impingement on multiple points on the surface, for all four surfaces will ultimately increase the heat dissipation capability of the system.

Figure 45 and Figure 46 show the flow boiling curves with the parallel and impinging flow distributors, for the bare silicon surface at a fixed facility water temperature and flow rate. It can be observed from the figures that at 360mL/min flow rate, the curves are almost on top of each other, showing similar thermal performance. At 1260 mL/min, the implementation of the impinging flow distribution system results in lower surface temperatures in the forced convection and this difference continued to decrease though the partial boiling regime. Similar trends are observed for the system at the facility water temperature of 15°C. The microfinned surface also shows a similar trend, as shown for the 1260 mL/min flow rate in Figure 47. To understand the effect of flow distributors on the boiling curves for only the bottom heater surfaces, the data from only the bottom two heater surfaces is plotted in Figure 48. While the surface temperatures in the boiling curves essentially follow the same trend as the boiling curve for the entire system as shown in Figure 47, the temperature difference between the parallel and impinging flow distributors is higher for the bottom two surfaces. Also, for the highest flow rate value, forced convection dominates the heat transfer in microfinned surfaces with impingement flow, even a high heat flux values. This strong contribution from forced convection has also been visually confirmed through high-speed imaging, with the observed lack of nucleation activity even at

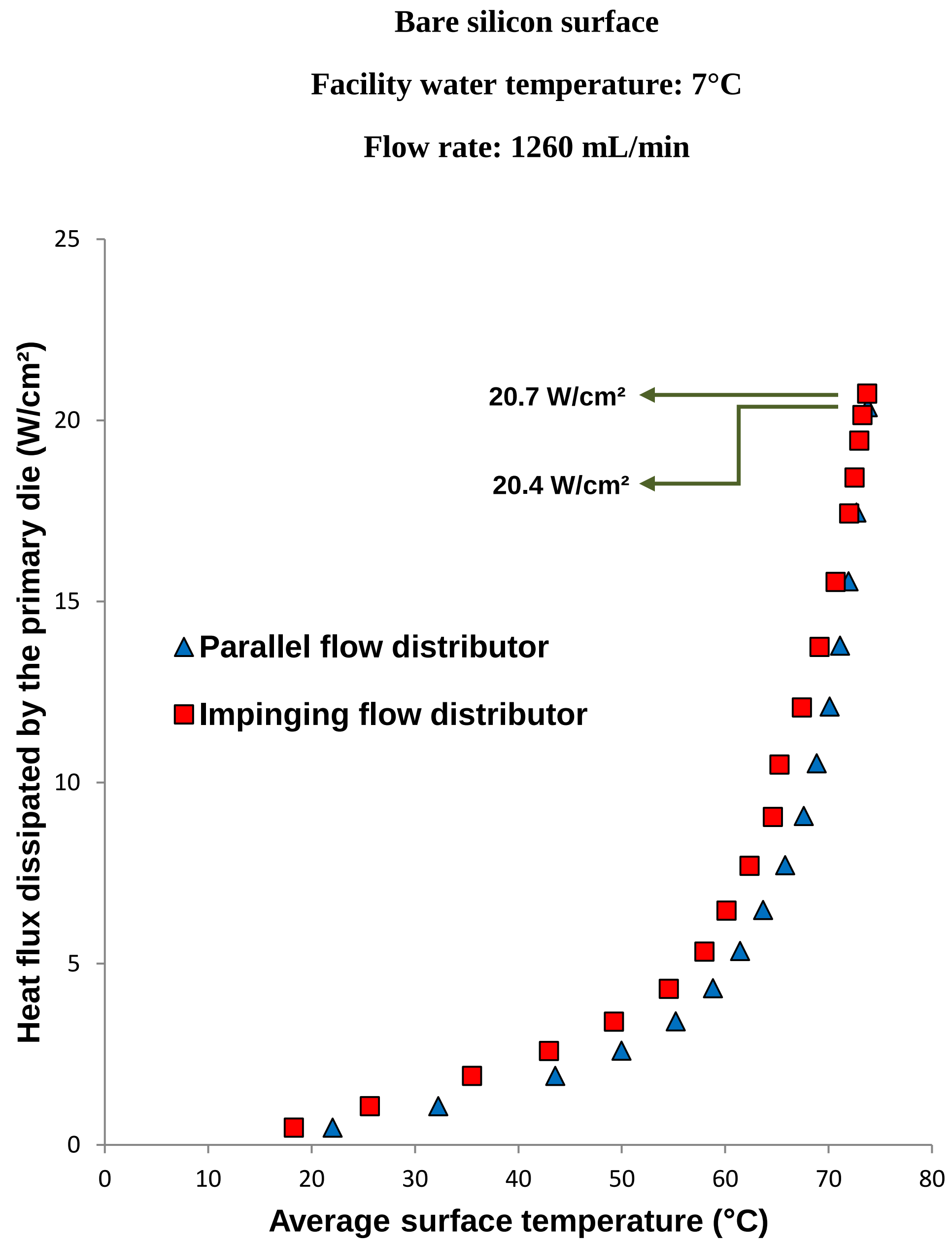

Figure 46: Comparison of thermal performance of parallel and impinging flow distributors for the bare silicon surface for 1260 mL/min flow rate

high heat fluxes. In contrast, the parallel flow distributor has more nucleation sites at heat fluxes of about 8 W/cm² for the parameters shown in Figure 48. This aforementioned difference can also been observed from Figure 48, in which the parallel flow distributor has a forced convection regime marked by a relatively constant slope, after which the increasing contribution from

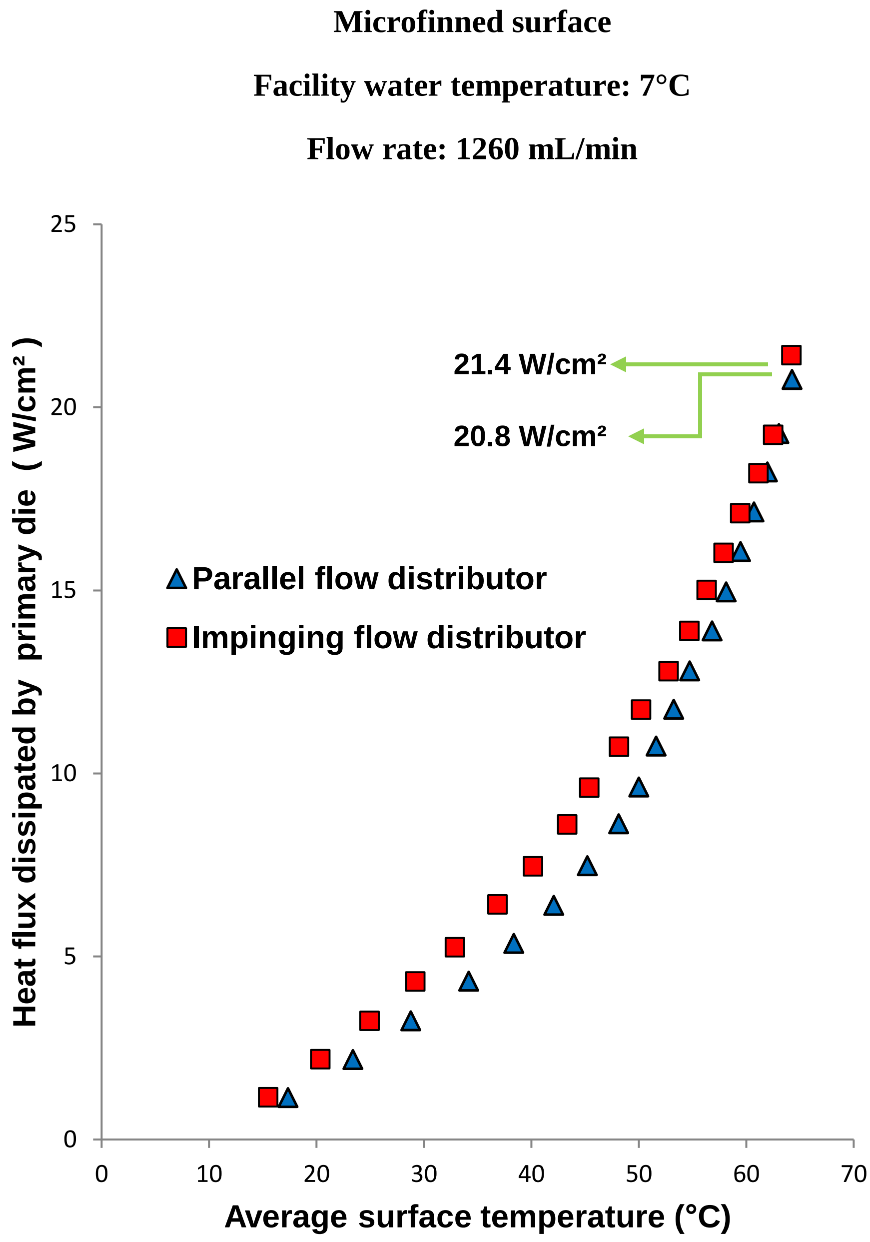

Figure 47: Comparison of thermal performance of parallel and impinging flow distributors for the microfinned surface for 1260 mL/min flow rate

nucleate heat transfer above a heat flux of about 5 W/cm² continually steepens the slope of the boiling curve. In contrast, the impinging flow distributor has a curve with relatively constant slope up to heat flux values in the neighborhood of 14 W/cm². Another notable aspect is that the impingement flow distribution offers forced convection dominated heat transfer coefficients, which are high enough to keep up with the nucleate boiling dominated heat transfer coefficients in the parallel flow distributor.

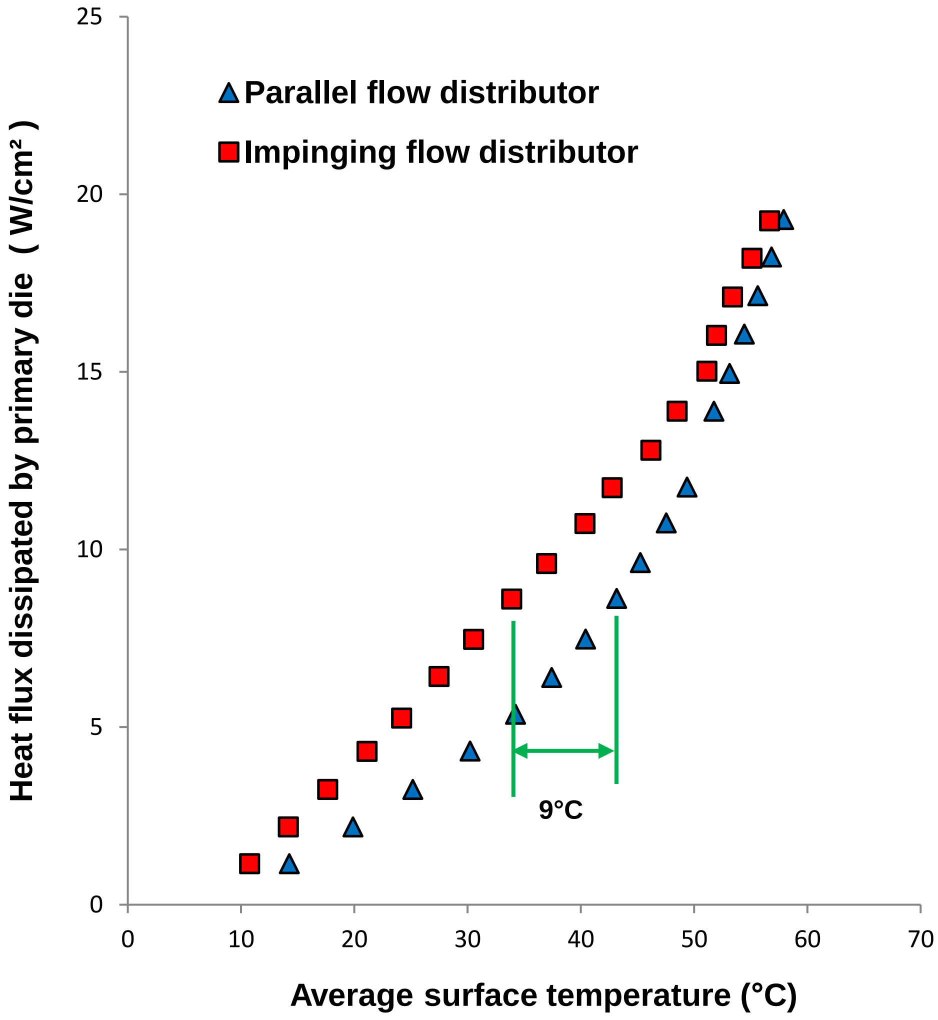

Microfinned surface

Facility water temperature: 7°C

Flow rate: 1260 mL/min

Figure 48: Comparison of thermal performance of parallel and impinging flow distributors only for the bottom microfinned surfaces at 1260 mL/min flow rate

4.4 Nucleation Suppression

This section provides the results and observations from the investigations on the nucleation suppression phenomenon in this server module. The objective of the experiments in this study is to find the highest heat flux that can be dissipated by the system without any nucleation activity, for a fixed facility water temperature and for a flow rate of 1650 mL/min, which is highest flow rate used in this study. The study was carried out in two different ways. In one set of experiments, the facility water temperature of the system was set, followed by introducing a high flow rate of 1650 mL/min into the system, and finally adding a known heat flux to the surfaces. These sets will be refered to as flow-first runs from now on. In second set of experiments, the surfaces were first powered with a known heat flux, and then a flow rate of 1650 mL/min was introduced. These experiments will be referred to as heat-first runs. In both these experiments, the presence of nucleation activity was determined visually with the use of the Phantom® v310 high-speed camera. The system was determined to be in steady state when the surface, inlet dielectric fluid, and exit dielectric fluid temperatures stabilized. The highest heat flux achieved without nucleation was determined by starting with a low heat flux, and repeating the experiment each time with a 0.5 W/cm² heat flux increment. The experiments were performed till nucleation activity was observed, and the value one increment lower than the nucleation heat flux is reported as the highest heat flux value.

Figures 49 (a) – (d) show the change in nucleation activity for the bottom heated surfaces with the change in flow rate for the flow-first runs with parallel flow distributor. Equation 4 presents a relation from Hsu model [76], which provides the criterion for nucleation incipience on a surface. Depending on the fluid properties, subcooling and the thermal boundary layer thickness, there exists a range of cavity sizes that will support nucleation activity. Equation 4 provides the minimum and maximum values of this range. The embryonic bubbles in cavity sizes below this range are too small to receive wall super heat and activate. For the cavity sizes above this range, the embryonic bubble is large enough to protrude above the superheated boundary layer and expose itself to the relative cooler fluid. This results in condensation of these bubbles, resulting in inhibition of bubble growth and its detachment from the surface. Therefore the cavities or sites with these bubbles remain inactive. The boundary layer thickness for the no flow

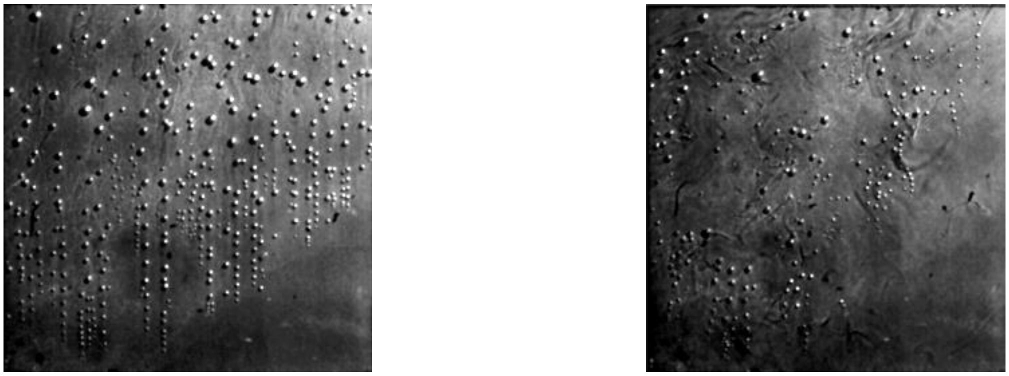

(a) No flow **(b)** 500 mL/min

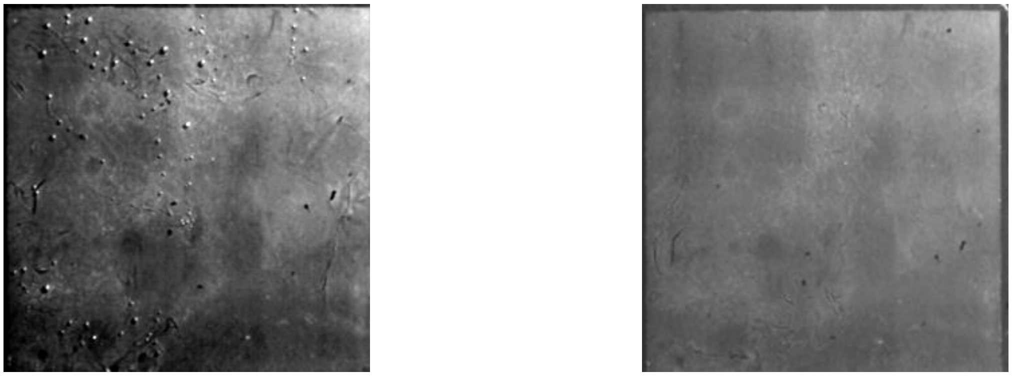

(c) 1000 mL/min **(d)** 1650 mL/min

Figure 49: Nucleation suppression in bare silicon surfaces

condition is a natural convection boundary, which is always thicker than the combined natural and forced convection boundary layers or forced convection dominated boundary layers. This results in the values from Equation 4 being higher, which means a wide range of cavities sizes can be active. This higher range increase the probability of nucleation in natural convection. In forced convection, the thermal boundary layer thickness is related to the momentum boundary layer thickness and the Prandtl number. The thickness of the momentum boundary layer is inversely proportional to the Reynolds number (Re) as shown by the Equations 5 and 6 for laminar and turbulent flow over a flat plate, respectively. For the fluid system in this study, these equations are applicable to the bare silicon surface with parallel flow distributor, especially for the bottom heated surfaces, since the three dimensional effects are less than that of the top surfaces due to the proximity to the flow distributor. The increasing flow rates increase the Re, and therefore decrease the thickness of the momentum and thermal boundary layers. This results in a lower range of nucleation cavity sizes according to Equation 4, leading to fewer nucleation sites. From Figures 49 (a) – (d), it can be observed that for a given heat flux, increasing the flow rate reduces the number of nucleation sites for the bare silicon surface.

$$\begin{Bmatrix} r_{c,min} \\ r_{c,max} \end{Bmatrix} = \frac{\delta_t}{4}\left[1 - \frac{\Theta_{sat}}{\Theta_w}\begin{Bmatrix} + \\ - \end{Bmatrix}\sqrt{\left(1 - \frac{\Theta_{sat}}{\Theta_w}\right)^2 - \frac{12.8\,\sigma\, T_{sat}(P_l)}{\rho_v\ h_{lv}\,\delta_t\,\Theta_w}}\right] \tag{4}$$

$$\Theta_{sat} = T_{sat}(p_l) - T_\infty \qquad\qquad \Theta_w = T_w - T_\infty$$

$$\delta = 5 * x * Re_x^{-1/2} \tag{5}$$

$$\delta = 0.37 * x * Re_x^{-1/5} \tag{6}$$

In a pool boiling system, the temperature change from wall temperature to saturation temperature occurs across a larger distance than that in flow boiling. This is shown in Figure 50. This means that in pool boiling, embryonic vapor bubble formed on the surface is surrounded by a fluid that has a relatively higher superheat than the flow boiling system. As the degree of superheat is not constant across the boundary layer in both pool as well as flow boiling systems, a mean or effective superheat ΔT_e is used for comparison. In pool boiling system, the mean superheat value is close to the wall superheat value ΔT , due to the relatively gentle slope of the temperature profile. In flow boiling system, the temperature profile is steeper, and the mean superheat is significantly lower than the wall superheat. This low mean superheat value implies that nucleation activity decreases along the flow direction for the flow boiling surface, up to the point where the local superheat around the bubble periphery is low enough that it cannot support nucleation. Heat transfer from this point is through the evaporation of the thin film above the surface.

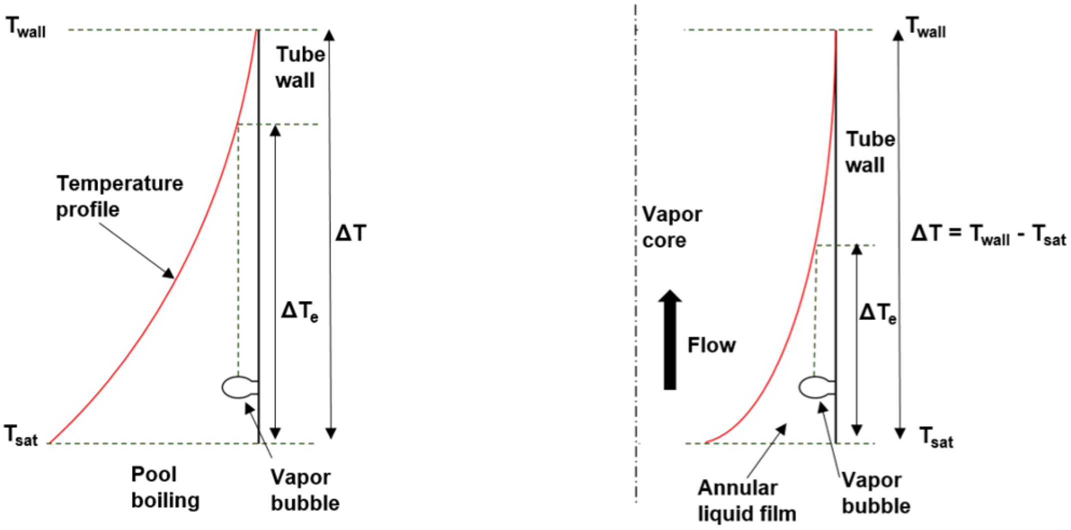

Figure 50: Temperature profiles for pool boiling system (left) and flow boiling system (right)

Table 14 provides the nucleation suppression data for the bare silicon surface. The highest heat flux values that cause suppression on all four surfaces, and also only the bottom two surfaces located close to the flow distribution inlet are presented. It can be seen from Table 14 that for a given facility water temperature, the value of heat flux that can be suppressed is generally higher for the flow-first runs compared to the heat-first runs. This apparent hysteresis in the suppression heat flux can be attributed to the difference in flow field between flow-first and heat-first runs, the latter being different due to the introduction of flow into a system with already active nucleation sites. Also, it can be seen that the increase in subcooling slightly increases the value of heat flux that can be suppressed. This is in accordance with Equation 4, in which decreasing T_∞ reduces the range of the nucleation cavity sizes. Comparing parallel and

Table 14: Summary of heat flux values with nucleation suppression for bare silicon surface

Highest heat flux with no nucleation activity (W/cm^2)		
Parallel flow distribution system		
Facility water temperature : 7°C		
Heated surface	Flow-first runs	Heat-first runs
All four surfaces	3	2.5
Bottom two surfaces	3.5	2.5
Facility water temperature : 15°C		
Heated surface	Flow-first runs	Heat-first runs
All four surfaces	2	2
Bottom two surfaces	3	2
Impinging flow distribution system		
Facility water temperature : 7°C		
Heated surface	Flow-first runs	Heat-first runs
All four surfaces	3	2
Bottom two surfaces	5	3
Facility water temperature : 15°C		
Heated surface	Flow-first runs	Heat-first runs
All four surfaces	2.5	2
Bottom two surfaces	4	2.5

impinging systems, it can be observed that for the bottom heated surfaces in flow-first runs, the impinging system has relatively higher heat flux values than the parallel system. This is due to the more efficient boundary layer disruption mechanism of the impinging flow, compared to the parallel flow path.

The nucleation suppression phenomenon for the microfinned surface is shown in Figures 51 (a) – (d). These figures represent the high-speed images for the bottom heated surfaces for flow-first runs with the impingement flow distribution system. Figures 51 (c) and (d) show the surfaces at a higher magnification, from which the nucleating bubbles can be clearly discerned from other surface features.

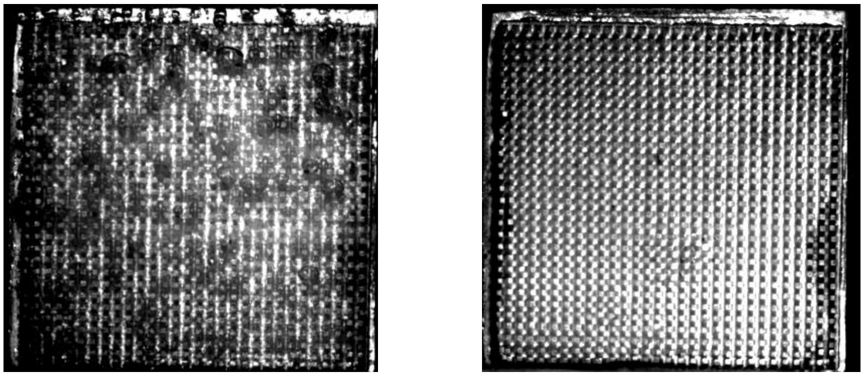

(a) No flow **(b)** 1650 mL/min

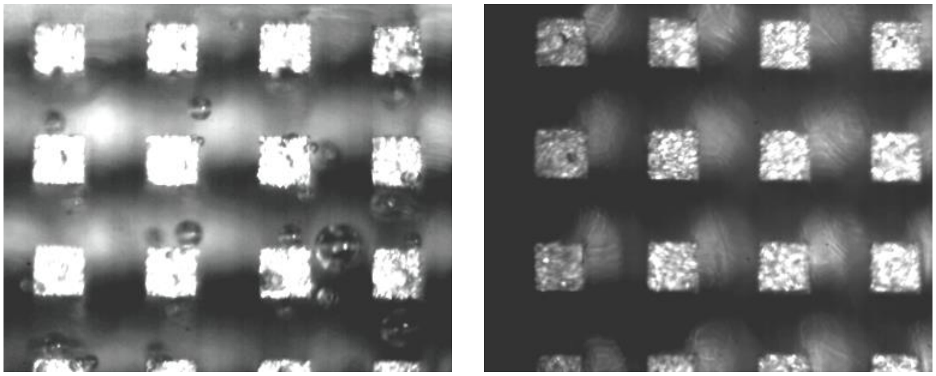

(c) No flow – higher magnification **(d)** 1650 mL/min – higher magnification

Figure 51: Nucleation suppression in microfinned surfaces

The heat flux values supported without nucleation activity, for the microfinned surface, are listed for different parameters in Table 15. The parallel flow distribution system for the microfinned shows some increase in heat flux values compared to the same flow distributor for the bare silicon surface. This is due to the increase in single-phase heat transfer coefficient due to the higher heat transfer area of the microfinned surfaces. For the same heat flux value higher heat transfer coefficient results in lower wall temperature, which decreases the Θ_w values. Lower Θ_w increases the second term of Equation 4 inside the square bracket, and in effect reduces the range of cavity sizes. For the microfinned surfaces, the impingment flow distribution system for the microfinned surface shows a more interesting trend. The bottom two surfaces under this flow distributor support very high heat flux values without nucleation activity, with 15 W/cm² for 15°C facility water temperature, and as high as 18 W/cm² for 7°C facility water temperature. For the heat-first runs, as the system starts with no flow addition, therefore the highest heat flux that can be added to the system for a given facility temperature is the highest heat flux supported by pool boiling. Nucleation activity at this heat flux value was suppressed by the addition of flow during the heat-first runs, and as is it not known if the flow can suppress any more than this heat flux value, it is labeled as the "pool boiling limit" in Table 15. These high values of nucleation suppression heat flux can be attributed to the combination of two effects – high heat transfer area due to the extended surface of the microfinned surface and effective disruption of the boundary layer with the impinging flow. This combination also offers high heat-transfer coefficients, which results in multiple parameters in Equation 4 that favor nucleation suppression.

Table 15: Summary of heat flux values with nucleation suppression for microfinned surface

Highest heat flux with no nucleation activity (W/cm^2)		
Parallel flow distribution system		
Facility water temperature : 7°C		
Heated surface	Flow-first runs	Heat-first runs
All four surfaces	4	3
Bottom two surfaces	5	3
Facility water temperature : 15°C		
Heated surface	Flow-first runs	Heat-first runs
All four surfaces	3.5	2.5
Bottom two surfaces	4.5	2.5
Impinging flow distribution system		
Facility water temperature : 7°C		
Heated surface	Flow-first runs	Heat-first runs
All four surfaces	5.5	5
Bottom two surfaces	18	Pool boiling limit
Facility water temperature : 15°C		
Heated surface	Flow-first runs	Heat-first runs
All four surfaces	5	4.5
Bottom two surfaces	15	Pool boiling limit

Chapter 5: Conclusions

Experimental investigations were conducted to quantify the effect of facility water temperature, flow rate, surface characteristics and flow distribution system on the flow boiling performance of a small form factor server cooling model. The results indicate that the decrease in facility water temperature by 8°C and increase in flow rate by 900 mL/min results in a heat dissipation improvement of up to 50% for the bare silicon surface and up to 40% for the microfinned surface. The values of facility water temperature used in this study are typically used in data center facilities that have a chiller for heat rejection. The flow rate values used in this experiment are gentle, with the highest value approximately close to 1.25 L/min. While some flow boiling curves show changes in surface temperatures in the forced convection and partial boiling regimes, the surface temperatures in the fully developed boiling regime for all the flow boiling curves in this study are less sensitive to the changes in flow rate and facility water temperature.

The use of surface enhancements offers improved reliability of the electronic packages the server cooling module, as both microporous and microfinned surfaces operate at significantly lower temperatures than the bare silicon surface for similar heat flux values. In terms of heat dissipation, the microporous surface outperforms both bare silicon and microfinned surfaces with heat flux values of up to 22.8 W/cm^2, even at the highest facility water temperature tested in this study. For the highest subcooling and flow rate tested in this study, the microfinned surface did not offer significant improvement in heat dissipation over the bare silicon surface.

The thermal performance of the impinging flow distribution system is similar to that of the parallel flow distribution system, since the impingement effects are local to the bottom row of heaters. Studies performed by only powering the bottom row of heaters showed up to 28.6 W/cm² heat flux for the microfinned surface, indicating the potential of the impingement system in improving heat dissipation.

The nucleation suppression phenomenon in flow boiling was investigated for this cooling module. It was observed that the microfinned surface with impinging flow distributor could support heat flux values of up to 18 W/cm² without any nucleation activity for the highest flow rate tested in this study.

5.1 Suggestions for future studies

From the literature review, for similar subcooling and flow rate, it was observed that the microfinned surface generally offers higher heat dissipation over the plain surface. This was not the case in the current study. As it was discussed in the results section, at higher flow rates, there is a significant difference in boiling activity between the top and bottom microfinned surfaces. Modifications in the flow distribution system to improve the uniformity of boiling activity may result in higher heat dissipation for the microfinned surface.

The impingement flow distribution system used in the current study provided impingement only to the bottom surfaces, and also only to the center plane of the bottom heated surfaces. A flow distribution system that delivers impinging flow at multiple points across all four surfaces would result in better convective transport and disruption of boundary layer in each surface, and ultimately increase the heat dissipation capability of the system.

References

[1] A. Shehabi, et al. “United States Data Center Energy Usage Report” (June 2016).

[2] Uptime Institute, “2014 Data Center Industry Survey”, 2014, Available: https://journal.uptimeinstitute.com/2014-data-center-industry-survey/.

[3] S.V. Garimella, T. Persoons, J. Weibel and L.T. Yeh, “Technological Drivers in Data Centers and Telecom Systems: Multiscale Thermal, Electrical, and Energy Management”, *Applied Energy,* 2013, Vol. 107, pp. 66-80.

[4] R. Schmidt, A. Vallury, M. Iyengar, “Energy Savings Through Hot and Cold Aisle Containment Configurations for Air Cooled Servers in Data Centers”, *Proceedings of the ASME 2011 Pacific Rim Technical Conference and Exposition on Packaging and Integration of Electronic and Photonic Systems (InterPACK 2011).*

[5] Google, “Efficiency: How We Do It”, 2017, Available: https://www.google.com/about/datacenters/efficiency/internal/.

[6] Facebook, “Prineville, OR DataCenter”, 2017, Available: https://www.facebook.com/PrinevilleDataCenter/app/399244020173259/.

[7] 3M, “Immersion Cooling with 3M™ Novec™ Engineered Fluids”, Available: http://multimedia.3m.com/mws/media/949741O/immersion-cooling-3mtm-novectm-engineered-fluid-infographic.pdf.

[8] Allied Control (2014), DataTank™ Product Information [PDF]. Available:http://www.allied-control.com/publications/DataTank_Product_Info.pdf.

[9] Green Revolution Cooling (2012), Intel Publicizes Results from CarnotJet™ System Testing (Sep, 2012) [PDF]. Available:http://www.grcooling.com/wp-content/uploads/2015/03/2012-09-10-Intel-Publicizes-Results-from-CarnotJet-System-Testing.pdf.

[10] Thomasnet, “As Data Centers Grow, Innovators Search for Green Cooling Methods”, (2012) Available” http://news.thomasnet.com/imt/2012/09/11/as-data-centers-grow-innovators-search-for-green-cooling-methods.

[11] Iceotope, “University of Leeds Project”, 2013, Available: https://static1.squarespace.com/static/58bd659e17bffc359072bbfd/t/592ef391b8a79ba0444c33aa/1496249234288/Leeds-Case-Study.pdf.

[12] Iceotope, “The Iceotope Liquid Cooling System in Action”, 2013, Available: http://iceotope-news.blogspot.com/2013/03/the-iceotope-liquid-cooling-system-in.html.

[13] G.E. Moore, "Cramming more components onto integrated circuits," 1965, Electronics, Vol. 38, No. 8.

[14] A. Huang, "The death of Moore's Law will spur innovation," Mar 2015, IEEE Spectrum, Available: http://spectrum.ieee.org/semiconductors/design/the-death-of-moores-law-will-spur-innovation.

[15] J. Hruska, "Intel at ISSCC: 14nm in the bag, full steam ahead on 10nm," Feb 2015, ExtremeTech, Available: http://www.extremetech.com/extreme/199636-intel-at-isscc-14nm-in-the-bag-full-steam-ahead-on-10nm.

[16] “Qualcomm and Samsung Colloborate on 10 nm Process Technology For the Latest Snapdragon 835 Mobile Processor”, 2016, Available: https://www.qualcomm.com /news/releases/2016/11/17/qualcomm-and-samsung-collaborate-10nm-process-technology-latest-snapdragon.

[17] J. Gu, "Health Assessment and Prognostics of Electronic Products: An Alternative to Traditional Reliability Prediction Methods," Electronics Cooling, May 2009, Available:http://www.electronics-cooling.com/2009/05/health-assessment-and-prognostics-of-elec, tronic-products-an-alternative-to-traditional-reliability-prediction-methods/.

[18] ITRS 2011, “Assembly and Packaging”, Available: https://www.dropbox.com/sh/r51qrus06k6ehrc/AACQYSRnTdLGUCDZFhB6_iXua/2011Chapters?dl=0.

[19] Nakayama, W., “Heat in Computers: Applied Heat Transfer in Information Technology” *Journal of Heat Transfer* (2014), 136(1), 013001.

[20] R.E. Simons, "Direct Liquid Immersion Cooling for High Power Density Microelectronics," May 1996, Electronics Cooling, Available: http://www.electronics-cooling.com/1996/05/direct-liquid-immersion-cooling-for-high-power-density-microelectronics/.

[21] M.J. Ellsworth, Jr. et al., “The Evolution of Water Cooling for Large IBM Server Systems: Back to the Future”, *11th Intersociety Conference on Thermal and Thermomechanical Phenomena in Electronic Systems* (ITHERM), 2008.

[22] R.E. Simons, “The Evolution of IBM High Performance Cooling Technology”, *IEEE Transactions on Components, Packaging, and Manufacturing Technology: Part A*, 1995, Vol. 8, Issue: 4.

[23] R.C. Chu, “Review of Cooling Technologies for Computer Products: Past, Present and Future”, 2005, Available: http://cseweb.ucsd.edu/~kuan/talk/ChuRichardX05X1X.31.05X-Presentation.pdf

[24] "IBM 3081 Thermal Conduction Module", Electronic Material Handbook: Packaging (Vol. 1) Available: https://books.google.com/books?id=c2YxCCaM9RIC&pg=PA48&dq=ibm+tcm+3081&hl=en&sa=X&ved=0ahUKEwjV2Ze66frUAhUSfiYKHV6WATUQ6AEIJDAA#v=onepage&q=ibm%20tcm%203081&f=false

[25] G. Goth et al., "An Overview of the IBM zEnterprise EC 12 Processor Cooling System", 2014, *14th Intersociety Conference on Thermal and Thermomechanical Phenomena in Electronic Systems* (ITHERM).

[26] Coolcentric, "The Coolcentric Family of Rear Door Heat Exchangers", Available: http://www.coolcentric.com/Portals/0/pdf/Coolcentric-RDHx-4PageBrochure-082012.pdf

[27] A. Bar-Cohen et al., "Encyclopedia of Thermal Packaging", Available: https://books.google.com/books?id=0BLGCgAAQBAJ&pg=RA1-PA13&dq=cray+2+cooling&hl=en&sa=X&ved=0ahUKEwivvNz_7PrUAhXMJCYKHbwtDDgQ6AEIJDAA#v=onepage&q=cray%202%20cooling&f=false

[28] Motivair, "ChilledDoor Rack Cooling System by motivair", Available: http://www.chilleddoor.com/files/uploads/2014/10/MOT_chilledDoor_9-2016_FINAL.pdf

[29] S.R. Cray Jr., "Immersion Cooled High Density Electronic Assembly", 1986, US Patent 4,590,538.

[30] Cray Research Inc, “The Cray-2 Computer System”, 1985, Available: http://archive.computerhistory.org/resources/text/Cray/Cray.Cray2.1985.102646185.pdf

[31] S. Nukiyama, “The Maximum and Minimum Values of the Heat Q Transmitted from Metal to Boiling Water under Atmospheric Pressure”, 1934, *International Journal of Heat and Mass Transfer,* Vol.9, pp. 1419-1433.

[32] Chen et al., “Nanowires for Enhanced Boiling Heat Transfer”, 2009, *Nano letters,* Vol.9 No.2 pp. 548-553.

[33] P. J. Berenson, “Experiments on Pool Boiling Heat Transfer”, 1962, *International Journal of Heat and Mass Transfer,* Vol. 5, pp. 985-999.

[34] S. Oktay and A. F. Schmeckenbecher, “Preparation and Performance of Dendritic Heat Sinks”, 1974, *Journal of The Electrochemical Society,* Vol.121, Issue 7, pp. 912-918.

[35] L. -H. Chien and C. -C. Chang, “Experimental Study of Evaporation Resistance on Porous Surfaces in Flat Heat Pipes”, 2002, *8th Intersociety Conference on Thermal and Thermomechanical Phenomena in Electronic Systems* (ITHERM).

[36] L. Campbell and P. Tuma, “Numerical Prediction of the Junction-to-Fluid Thermal Resistance of a Two-Phase Immersion-Cooled IBM Dual Core POWER 6 Processor”, 2012, *28th* IEEE SEMI-THERM *Symposium.*

[37] G. Moreno, J.R. Jeffers and S. Narumanchi, “Effects of Pressure and a Microporous Coating on HFC-245fa Pool Boiling Heat Transfer”, 2014, *Journal of Heat Transfer,* Vol. 136 (10), 101502.

[38] S.M. You and J.P. O’Connor, “Boiling Enhancement Coating”, 1998, US Patent 5,814,312.

[39] J.P. O’Connor and S.M. You, “A Painting Technique to Enhance Pool Boling Heat Transfer in Saturated FC-72”, 1995, *Journal of Heat Transfer,* Vol. 117(2), pp. 387-393.

[40] J. Y. Chang, S.M. You, “Boiling Heat Transfer Phenomena from Microporous and Porous Surfaces in Saturated FC-72”, 1997, *International Journal of Heat and Mass Transfer*, Vol. 40, No. 18, pp. 4437-4447.

[41] K.N. Rainey and S.M. You, “Pool Boiling Heat Transfer from Plain and Microporous, Square Pin-Finned Surfaces in Saturated FC-72”, 2000, *Journal of Heat Transfer,* 122(3), pp. 509-516.

[42] M.Arik, A. Bar-Cohen and S.M. You, “Enhancement of Pool Boiling Critical Heat Flux in Dielectric Fluids by Microporous Coating”, 2007*, International Journal of Heat and Mass Transfer,* Vol. 50, Issues 5-6, pp. 997-1009.

[43] J.L. Parker and M.S. El-Genk, "Enhanced Saturation and Subcooled Boiling of FC-72 Dielectric Liquid", 2005, *International Journal of Heat and Mass Transfer,* Vol. 48, Issue 18, pp. 3736-3752.

[44] H. Honda, H. Takamastu and J.J. Wei, "Enhanced Boiling of FC-72 on Silicon Chips With Micro-Pin-Fins and Submicron-Scale Roughness", 2002, *Journal Heat Transfer,* Vol. 124(2), 383-390.

[45] M. Yuan, J. Wei, Y. Xue, J. Fang, "Subcooled Flow Boiling Heat Transfer of FC-72 from Silicon Chips Fabricated with Micro-pin-fins" *International Journal of Thermal Sciences* (2009) 48: 1416-1422.

[46] S. Ujereh, T. Fischer and I. Mudawar, "Effects of Carbon Nanotube Arrays on Nucleate Pool Boiling",2007, *International Journal of Heat and Mass Transfer,* Vol. 50, Issues 19-20, pp.4023-4038.

[47] J. Gess, "Experimental Investigation of a Liquid Immersion Cooled Electronics Module using Two-Phase Heat Transfer for Thermal Management" PhD dissertation, Mechanical Engineering, Auburn University, Auburn, AL, 2015.

[48] A. Sridhar, "Experimental Evaluation of Immersion-Cooled Strategies for High-Power Server Modules", MS thesis, Mechanical Engineering, Auburn University, Auburn, AL, 2012.

[49] B. Ramakrishnan, “Viability of Server Module Thermal Management Using Enhanced Heat Sinks and Low Global Warming Potential Dielectric Fluids”, MS thesis, Mechanical Engineering, Auburn University, Auburn, AL, 2014.

[50] A. Jaikumar, S.G. Kandlikar, “Enhanced Pool Boiling for Electronics Cooling Using Porous Fin Tops on Open Microchannels with FC-87”, *Applied Thermal Engineering* (2015) 91: 426-433.

[51] M.S. El-Genk, “Nucleate Boiling Enhancements on Porous Graphite and Microporous and Macro-finned Copper Surfaces”, *Heat Transfer Engineering* (2012), 33:3, 175-204.

[52] S.J. Thiagarajan, R.Yang, C. King, and S. Narumanchi, “Bubble Dynamics and Nucleate Pool Boiling Heat Transfer on Microporous Copper Surfaces”, *International Journal of Heat and Mass Transfer* (2015), 89: 1297-1315.

[53] I. Mudawar and D.E. Maddox, “Critical Heat Flux in Subcooled Flow Boiling of Fluorocarbon Liquid on a Simulated Electronic Chip in a Vertical Rectangular Channel”,1989, *International Journal of Heat and Mass Transfer*, Vol.32, No.2, pp.379-394.

[54] I. Mudawar and D.E. Maddox, “Enhancement of Critical Heat Flux from High Power Microelectronic Heat Sources in a Flow Channel”, 1990, *Journal of Electronics Packaging*, Vol.112 (3), pp.241-248.

[55] T.C. Willingham and I. Mudawar, “Forced-Convection Boiling and Critical Heat Flux from a Linear Array of Discrete Heat Sources”, 1992, *International Journal of Heat and Mass Transfer*, Vol. 35, No. 11, pp. 2879-2890.

[56] K.N. Rainey, G. Li and S.M. You, “Flow Boiling Heat Transfer From Plain and Microporous Coated Surfaces in Subcooled FC-72”, *Journal of Heat Transfer* (2001) 123: 918-925.

[57] R. Cardenas, “Submerged Jet Impingement Boiling Thermal Management”, PhD dissertation, Mechanical, Industrial and Manufacturing Engineering, Oregon State University, Corvallis, OR, 2011.

[58] C. –F. Ma and A.E. Bergles, “Jet Impingement Nucleate Boiling”, 1986, *International Journal of Heat and Mass Transfer*, Vol.29, No.8, pp. 1095-1101.

[59] G.M. Chrysler, R.C. Chu and R.E. Simons,”Jet Impingement Boiling of a Dielectric Coolant in Narrow Gaps”, 1995, *IEEE Transactions on Components, Packaging and Manufacturing Technology*, Part. A, Vol. 1, No.3 pp. 527-533.

[60] R. Cardenas, V. Narayanan, “Heat Transfer Characteristics of Submerged Jet Impingement Boiling of Saturated FC-72” *International Journal of Heat and Mass Transfer* (2012), 55: 4217 - 4231.

[61] D. Copeland, “Single-Phase and Boiling cooling of Small Pin Fin Arrays by Multiple Jet Nozzle Impingment”, 1996, *Journal of Electronics Packaging*, Vol. 118(1), pp.21-26.

[62] S. Ndao, Y. Peles and M.K. Jensen, “Experimental Investigation of Flow Boiling Heat Transfer of Jet Impingement on Smooth and Micro Structured Surfaces”, 2012, *International Journal of Heat and Mass Transfer*, Vol.55, Issues 19-20, pp. 5093-5101.

[63] M.J. Rau, S.V. Garimella, “Confined Jet Impingement With Boiling on a Variety of Enhanced Surfaces”, *Journal of Heat Transfer* (2014), 136(10), 101503.

[64] I. Mudawar, D.C. Wadsworth, “Critical Heat Flux from a Simulated Chip to a Confined Rectangular Impinging Jet of Dielectric Liquid”, 1991, *International Journal of Heat and Mass Transfer*, Vol. 34, No.6, pp. 1465-1479.

[65] D.C. Wadsworth, I. Mudawar, “Cooling of a Multichip Electronic Module by Means of Confined Two-dimensional Jets of Dielectric Liquid”, 1990, *Journal of Heat Transfer*, Vol. 112(4), pp.891-898.

[66] G.E. Thorncroft, J.F. Klausner, R. Mei, “Suppression of Flow Boiling Nucleation”, *Journal of Heat Transfer* (1997), 119(3): 517-524.

[67] V.P. Carey, ”Saturated Flow Boiling”, Liquid-Vapor Phase-Change Phenomena, p.609 2008, Second Edition, Taylor and Francis, New York, NY.

[68] R. Meynart, ”Flow Velocity Measurements by Speckle Method”, 1979, SPIE Vol. 210 *2nd European Congress on Optics Applied to Metrology*, pp.25-28.

[69] V.K. Arghode, P. Kumar, Y. Joshi, T. Weiss, and G. Meyer, "Rack level modeling of air flow through perforated tile in a data center," 2013, Journal of Electronic Packaging, Vol. 135, No. 3, p. 030902-1.

[70] A. Pavlova and M. Amitay, ”Electronic Cooling Using Synthetic Jet Impingement”, 2006, *Journal of Heat Transfer*, 128(9), pp.897-907.

[71] L.J. Gong, K. Kota, W. Tao and Y. Joshi, “Thermal Performance of Microchannels With Wavy Walls for Electronics Cooling”, 2011, IEEE *Transactions on Components, Packaging and Manufacturing Technology*, Vol. 1, Issue 7, pp. 1029-1035.

[72] V.P. Carey, ”Subcooled Flow Boiling”, Liquid-Vapor Phase-Change Phenomena, p.600 2008, Second Edition, Taylor and Francis, New York, NY.

[73] “ASHRAE Thermal Guidelines”, Available: https://datacenters.lbl.gov/sites/all/files/ASHRAE%20Thermal%20Guidelines_%20SVLG%202015.pdf

[74] HP, “HP Proliant DL 380p Gen8 Server – Specifications,” 2015, Available: https://www.hpe.com/h20195/v2/getpdf.aspx/c04128241.pdf?ver=72.

[75] Extron Electronics, “Thermal Management Part 1: How Hot is Too Hot?”, Available: http://www.extron.com/company/article.aspx?id=thermalmgt1_ts.

[76] V.P. Carey, ”Criteria for the Onset of Nucleate Boiling”, Liquid-Vapor Phase-Change Phenomena, p.600 2008, Second Edition, Taylor and Francis, New York, NY.

Appendix A

Flow Distributor Component Drawings

This section provides the component drawings for the parallel and impingement flow distribution systems. The drawing for the parallel flow distribution has been reproduced from the study by Gess [47]. The study [47] also provides detailed engineering drawings for design and assembly of the enclosure system.

NOTES:

1. MATERIAL: ALUMINUM SHEET PER ASTM B221, 1/8" THICK.

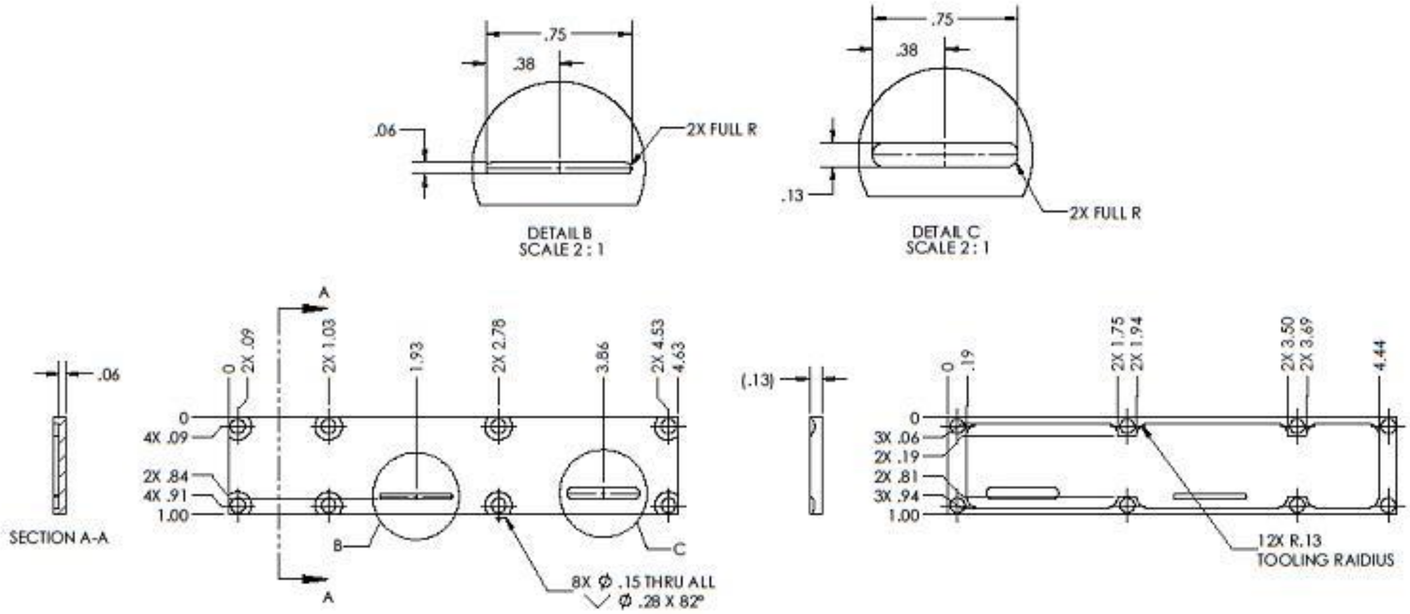

NEXT ASSY
USED ON
APPLICATION

UNLESS OTHERWISE SPECIFIED:
DIMENSIONS ARE IN INCHES
TOLERANCES:
FRACTIONAL ±
ANGULAR: MACH ± BEND ±
TWO PLACE DECIMAL ±
THREE PLACE DECIMAL ±
INTERPRET GEOMETRIC TOLERANCING PER:
MATERIAL
FINISH
DO NOT SCALE DRAWING

	NAME	DATE
DRAWN		
CHECKED		
ENG APPR.		
MFG APPR.		
Q.A.		
COMMENTS:		

TITLE:

SIZE B
DWG. NO. AUB-100039
REV
SCALE: 1:1
WEIGHT:
SHEET 1 OF 1

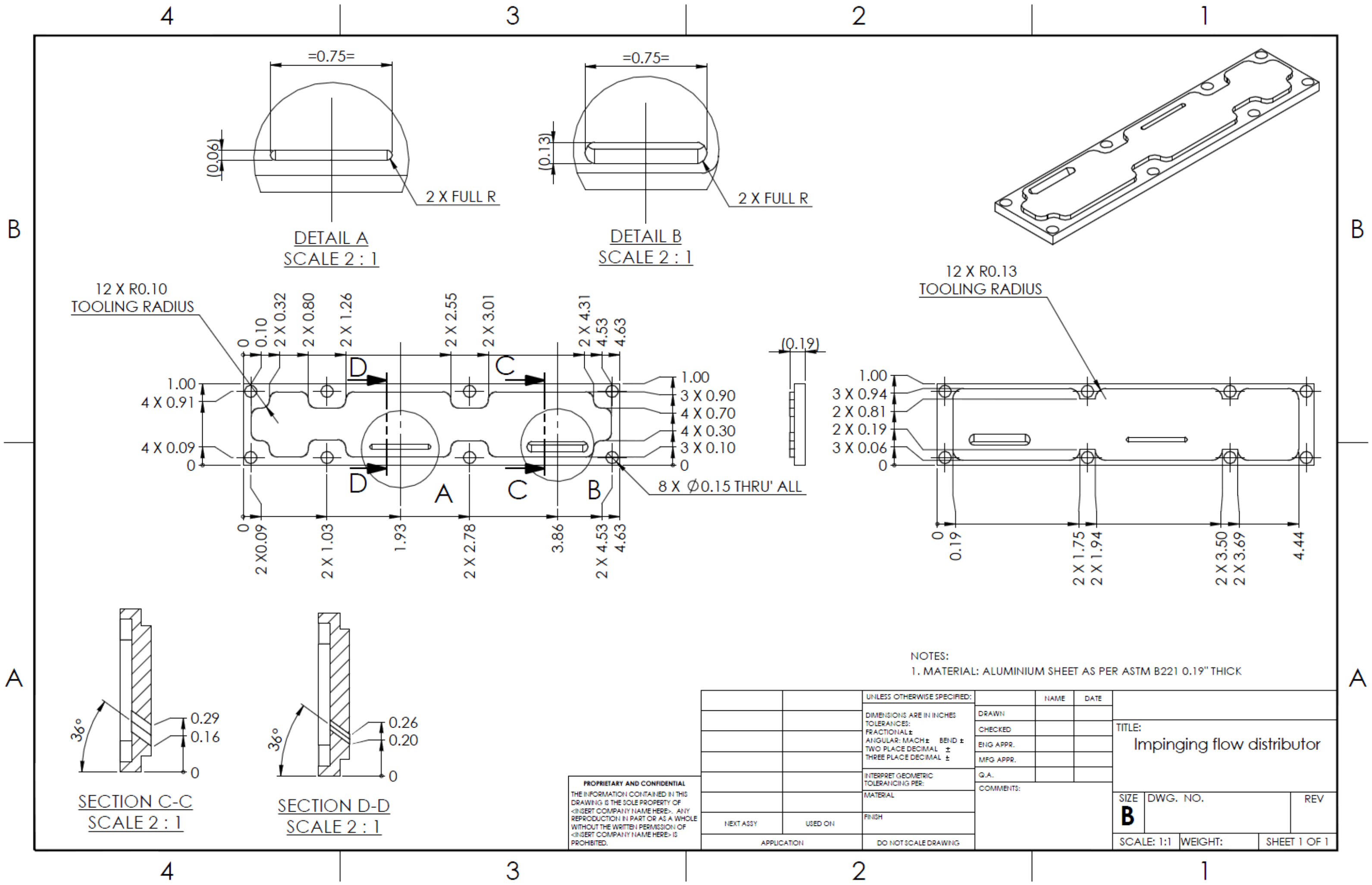

NOTES:

1. MATERIAL: ALUMINIUM SHEET AS PER ASTM B221 0.19" THICK

Appendix B

Data Acquisition System

The data acquisition system in this study employs multiple different data acquisition cards from National Instruments (NI) to measure voltage, current, temperature and to provide digital output signal for supplying excitation current to different temperature measurement diodes. The LabView software from NI was used for collecting and processing the data from the various sensors in the experimental setup. The details of data collection can be found in Chapter 3 of this study. A snapshot of front panel in the LabView virtual instrument (VI) is shown in Figure B.1. The wiring schematic for the power supply and temperature measurement connections to thermal test cells is shown in Figure B.2, and the schematic for other sensors such as thermocouples and flow meters is shown in Figure B.3.

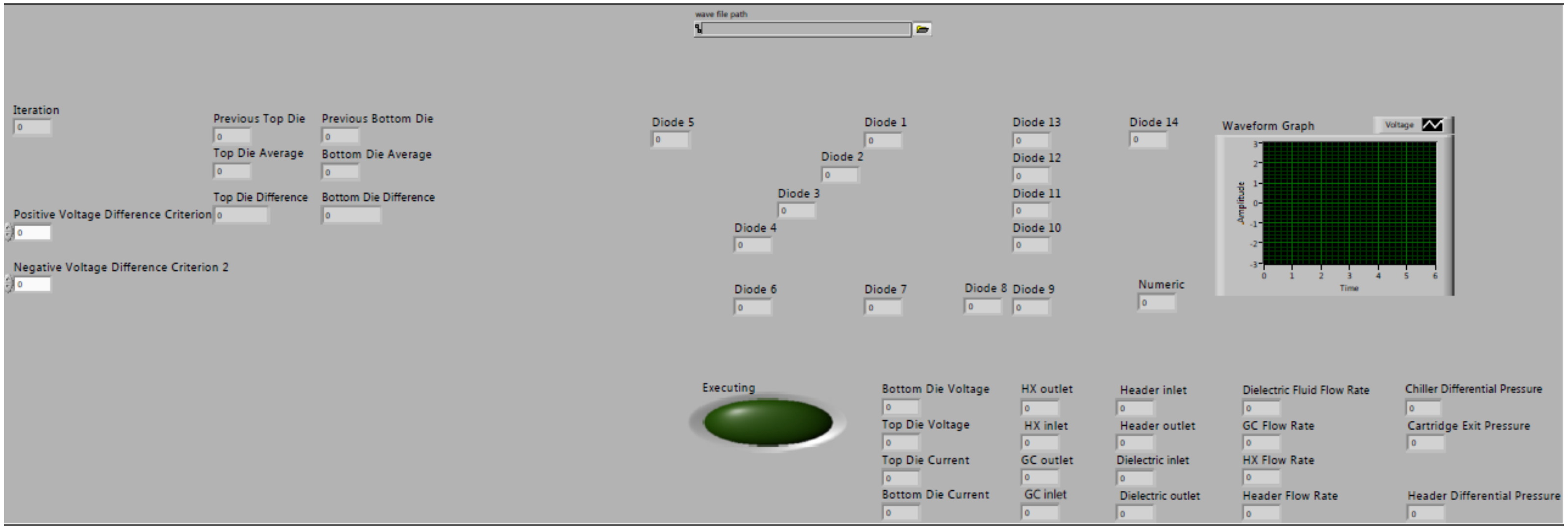

Figure B.1: Front panel of the LabView VI

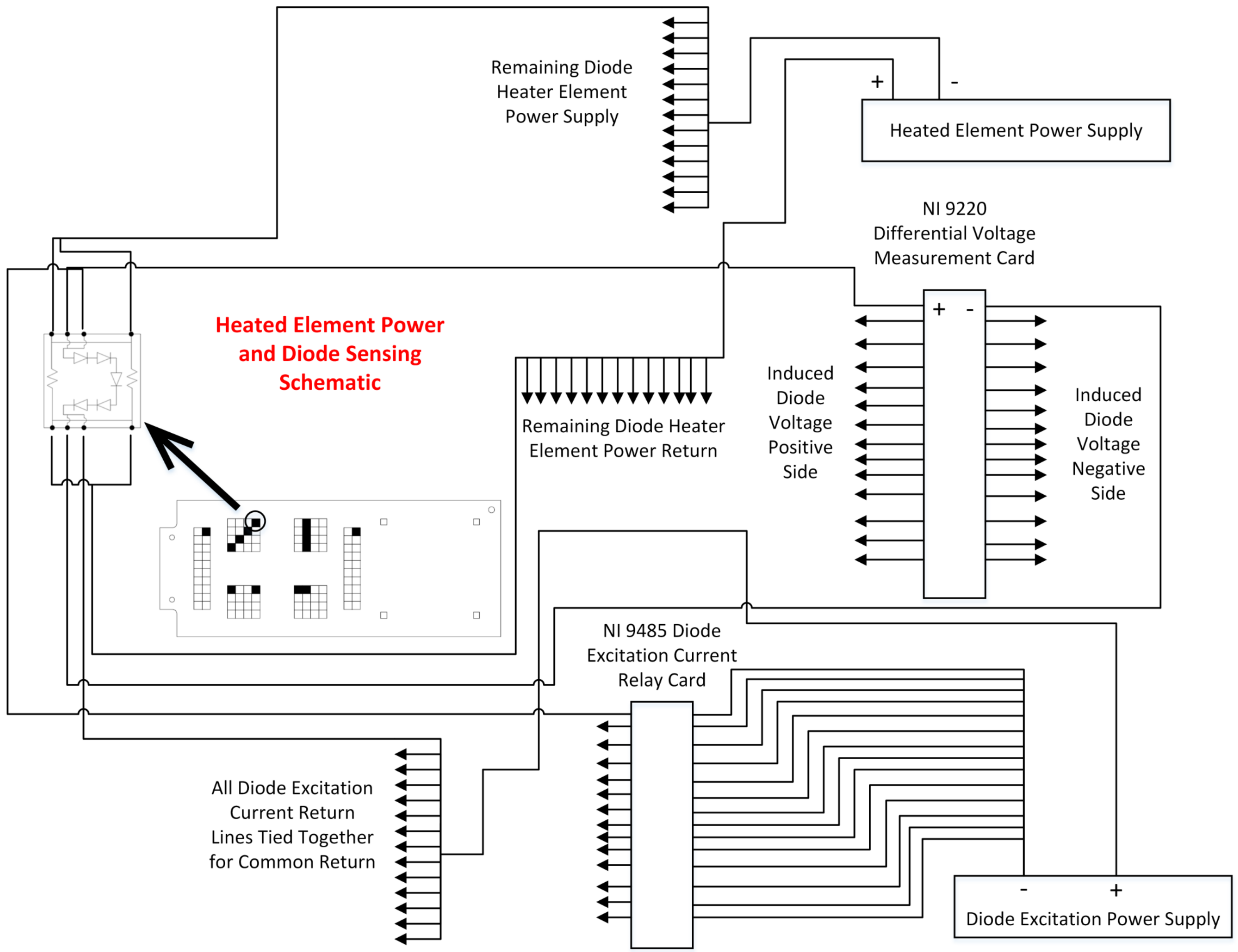

Figure B.2: Wiring schematic for the thermal test cell system

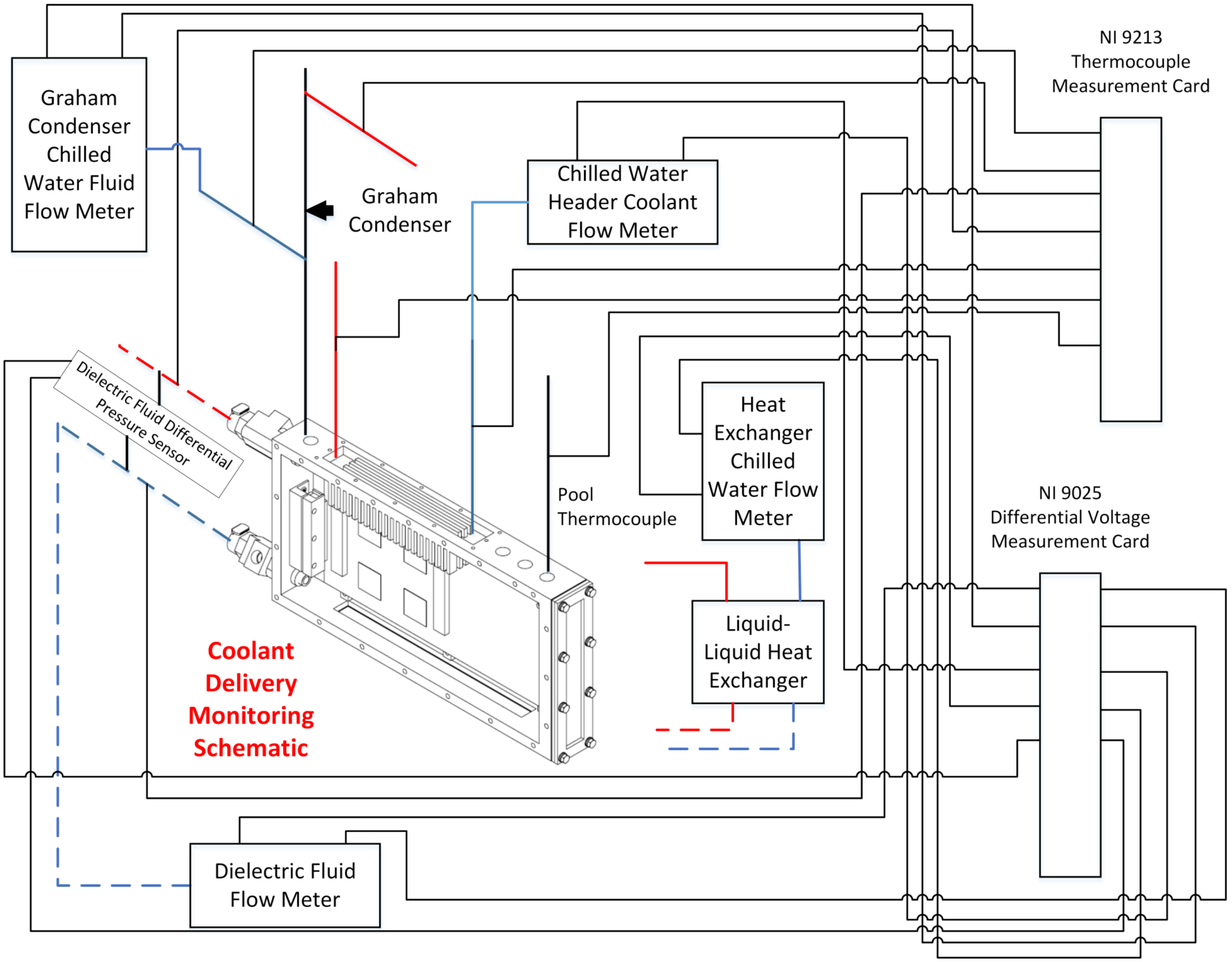

Figure B.3: Wiring schematic for different sensors in the system

Appendix C

Sample Calculations

C_{sf} Calculation

Manipulate the Rohsenow Correlation, Equation 3, to solve for C_{sf}:

$$C_{sf} = \frac{1}{\left\{\frac{q''}{\mu_l h_{lv}} * \left[\frac{\sigma}{g*(\rho_l - \rho_v)}\right]^{\frac{1}{2}} * Pr^{\frac{s}{r}} * \left[\frac{c_{pl}*[T_w - T_{sat}]}{h_{lv}}\right]^{-1/r}\right\}^{r}}$$

As an example, the C_{sf} value for the microporous surface was calculated using the base dimensions, or that interfacing with the 1” x 1” thermal test cell. The heat flux was calculated with the measured voltage and measured current, divided by this base area as shown below:

$$q'' = \frac{(42.44\ Volts * 5.24\ Amps) + (42.12\ Volts * 5.23\ Amps)}{4 * 6.45\ x\ 10^{-4}\ m^2}$$

$$q'' = 17.15\ x\ 10^4\ \frac{W}{m^2}\ or\ 17.15\ \frac{W}{cm^2}$$

The wall temperature is calculated by averaging the diode temperatures across the four dies

$$T_w = \frac{59.45\ °C + 57.53°C + 74.59\ °C + 65.81\ °C + 69.19\ °C + 74.51\ °C + 70.04\ °C + 66.17°C + 65.21\ °C}{9}$$

$$T_w = 66.9\ °C$$

Using Novec as the working fluid, its associated saturated properties from Table 2, along with the measured average surface temperature, the C_{sf} value is calculated below.

$$Pr = \frac{\frac{\mu_l}{\rho_l}}{\frac{k_l}{\rho_l * c_p}}$$

$$Pr = \frac{\frac{4.4\ x\ 10^{-4}\ (Pa*\mathrm{sec})}{1517\ \frac{kg}{m^3}}}{\frac{0.054\ \frac{W}{m*K}}{1517\ \frac{kg}{m^3}*1118\ \frac{J}{kg*K}}}$$

$$Pr = 9.11$$

$$C_{sf} = \frac{1}{\left\{\frac{17.15x\ 10^4 \frac{W}{m^2}}{4.4\ x\ 10^{-4}\ (Pa*sec)*88\ x\ 10^3 \frac{J}{kg}} * \left[\frac{9.24\ x\ 10^{-3} \frac{N}{m}}{9.81\ \frac{m}{sec^2}*\left(1517\ \frac{kg}{m^3} - 12.6\ \frac{kg}{m^3}\right)}\right]^{\frac{1}{2}} * 9.11^{\frac{1.7}{0.33}} * \left[\frac{1118\ \frac{J}{kg*K}*[66.9\ °C - 49°\ C]}{88\ x\ 10^3\ \frac{J}{kg}}\right]^{-1/0.33}\right\}^{0.33}}$$

$$C_{sf} = 0.0035$$

This is the final C_{sf} value shown on the left plot for Table 5 associated with the 360 mL/min dielectric fluid flow rate and 7°C facility water temperature data.

Appendix D

Microporous Surface Enhancement Fabrication Procedure

The following is information received from the manufacturer documenting the manufacture of the microporous surface used in the current study.

Introduction

The patented 3M™ Microporous Metallic Boiling Enhancement Coating (MMBEC) was developed to provide optimal boiling heat transfer coefficients with 3M™ Novec™ Engineered Fluids. 3M MMBEC is made with 3M™ developmental material L-20227. This powder is composed of sub-20µm copper particles coated with 0.5 wt% silver. L-20227 particles are applied to a copper substrate in a layer about 150µm thick and then fused at elevated temperature, typically 850ºC in the absence of oxygen. The silver diffuses into the copper, temporarily forming a eutectic that melts and re-solidifies, before cooling, as diffusion progresses. This method provides:

- High thermal conductivity ligament between particles
- Ligaments present at all particle contact points
- Pores size provides optimal nucleation sites for Novec™ fluids
- Coating properties relatively insensitive to processing conditions

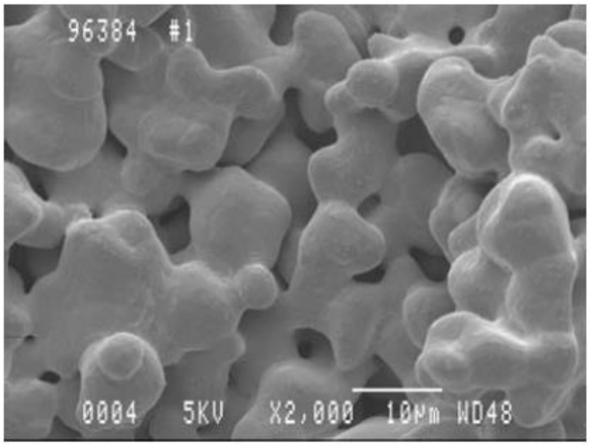

Figure D.1: Scanning Electron Micrograph of 3M MMBCE

Below are directions for the standard 3M technique for applying and fusing L-20227 powder. Other techniques are allowed and may be preferred depending on the equipment available.

Application

L-20227 particles are mixed with Dow 704 silicone diffusion pump oil to achieve a mixture that is 13% oil by weight. This mixture is applied to a flat copper substrate using standard screen printing techniques and a Sefar 45 180 mesh polyester screen (45-180 W IM E11F 0.5 30d STD) with the desired pattern. The resultant coating contains 0.052g/cm2 L20227 particles.

Notes: Particles may be applied dry (for example by knife coating) or using any volatile binder that will be removed in and compatible with the fusing process.

Fusing

Fusing is done at 0.01 milliTorr in a vacuum furnace. Temperature is raised to 300ºC and paused for 20 minutes to remove the oil. Temperature is then raised to 850ºC and held for 1 hour.

Notes: Inert atmospheres may be used in place of or in addition to vacuum to control oxygen levels. Ramp rates and equilibrium times were dictated by oven capabilities and temperature uniformity. Higher ramp rates and shorter equilibrium times may be possible if equipment allows.

Notes

Resultant coating thickness should be approximately 150µm. A minimum thickness of 100µm is required to achieve optimal performance. Heat transfer coefficients will drop precipitously as the thickness is reduced below this level. Thicknesses up to 300µm will perform well.

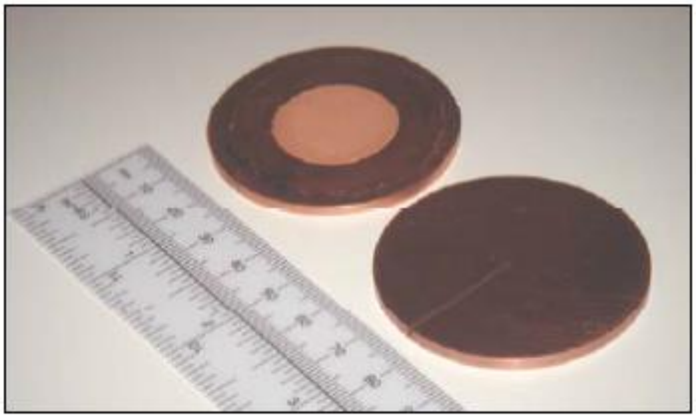

Figure D.2 : Photo of 3M MMBCE fused to a copper test disk